Probing Coprecipitation Processes Towards Synthesis of Lithium-Ion Battery Active Materials of Controllable Morphology and Composition

A Dissertation

Presented to

The Faculty of the School of Engineering and Applied Science

University of Virginia

In partial fulfilment

Of the requirements of the degree

Doctor of Philosophy in Chemical Engineering

By

Hongxu Dong

April 2018

Executive Summary

The fast increasing requirement of portable electronics, as well of the demanding of electric vehicles as a substitute for the robust engines that burn fossil fuels and cause warning impacts on the environment and of stable large scale energy storage systems for grid, all put a great pressure on the development and commercialization of high performing batteries with high energy capacity, high power density, and long cycle life. Besides the exploration of new chemistries and materials, modifications of current known battery materials is also an important and reliable direction of extracting higher and more stable energy. And lithium-ion batteries have been and will be considered as the most promising chemistry of batteries for further study.

Composition deviation of multicomponent transition metal (TM) oxides active materials have been found to result in decrease of structural stability and energy capacity, and particle morphologies are reported to determine the electrode packing density and thus the energy density. The synthesis process of the active materials has a profound but also complicated influence on the materials structure and electrochemical performances, which requires fundamental knowledge about the synthesis process itself. As a widely used synthesis method in both lab and industrial environment, coprecipitation reaction is well-known for its advantages of homogenous mixing of different ions and particle morphology tunability; the obtained precursor particles from coprecipitation reaction are directly fired with lithium salt to produce final TM oxide as cathode active materials, which means the properties of the precursors are determinant for the performance of the final active materials. While many different particle morphologies have been gained from coprecipitation synthesis to leverage the electrochemical performances of the cell, the knowledge of relationship between solution conditions and particle composition and morphologies is still lacking for a precise design and control of the precursors and final active materials properties, majorly because that

coprecipitation is a complex process where many different factors including temperature, reaction initiation method, solution mixing method and status, will influence the reaction. In addition, most synthesis processes for producing battery cathode materials requires multicomponent coprecipitation where more than one TM are involved and co-existing in the solution, which makes the process more complicated with potential interactions between different ions precipitations. More advanced tools are in need to enable the study of the multicomponent coprecipitation reaction, towards a more precise control of the synthesis procedure.

This dissertation addresses this knowledge gap in the literature by studying about the coprecipitation reaction mechanism via *in-situ* tracking the ion concentration and particle size distribution along the reactions, and also via conducting apparent reaction activation energy among the whole multicomponent composition rang. It also confirms the advantage of local mixing of different TM ions in the precipitates on the final materials phase purity and other properties. Attempt also has been made to design and tune the particle morphology of the precipitate by adding chemical inhibitors, and to align the particles with special shapes in the electrode with an external magnetic field. In these studies, we aimed to synthesize lithium-ion cathode active materials with controllable composition and particle morphology via coprecipitation reaction by using the knowledge gained through the solution chemistry study of coprecipitation reaction. The tools we developed along the process are expected to be useful techniques for studying nucleation and particle growth processes in general and can be applied to other single or multicomponent coprecipitation reactions for applications which requires accurate composition and particle morphology control.

Bibliography

The publications that resulted/will result from this dissertation are stated in each perspective chapter. A summary of all the publications is listed below:

Chapter 1: **Dong, H.,** G., Koenig, Jr., G. M. Coprecipitation as a Robust and Versatile Method to Synthesize Precursors for Good-Performing Lithium-ion Battery Cathode Active Materials: A Review. In Preparation.

Chapter 2: **Dong, H.**, & Koenig Jr, G. M. (2017). Compositional control of precipitate precursors for lithium-ion battery active materials: role of solution equilibrium and precipitation rate. Journal of Materials Chemistry A, 5(26), 13785-13798.

Chapter 3: **Dong, H.**, Wang, A., & Koenig, G. M. (2018). Role of coprecipitation and calcination of precursors on phase homogeneity and electrochemical properties of battery active materials. Powder technology, 335, 137-146.

Chapter 4: **Dong, H.**, Wang, A., Smart, G., Johnson, D., & Koenig Jr, G. M. (2018). In-situ analysis of nucleation and growth of transition metal oxalate battery precursor particles via time evolution of solution composition and particle size distribution. Colloids and Surfaces A: Physicochemical and Engineering Aspects, 558, 8-15.

Chapter 5: **Dong, H.**, Gardner, E., Barron, A., Koenig, Jr., G. M. Apparent Activation Energy of Multicomponent Transition Metal Oxalates Towards Tunable Synthesis of Battery Precursor Materials, Submitted.

Chapter 6: **Dong, H.**, Cai, C., Denecke, M. E., Remaly, G., Koenig, Jr., G. M. Low-tortuosity LiMn1.5Ni0.5O4 electrode by particle alignment under low magnetic field. In Preparation.

Table of Contents

1. Research Background: coprecipitation route for synthesizing battery active materials

1.1. Overview

This chapter provides the background and scientific basis for the work in this dissertation. An outline of coprecipitation reaction used as a synthesis method of transition metal (TM) battery material precursors is reviewed. This is the first review on this topic in the literature, even though this method has been widely used for both lab scale and manufacturing scale synthesis of battery materials for over two decades. Technical challenges for precisely designing and controlling the coprecipitation reactions, for the purpose of optimizing the particle properties and final electrochemical performances, are discussed in detail. The scope of the dissertation is then defined after reviewing the technical background. This chapter also provides the foundation for the arguments presented in subsequent chapters which provide more focused and detailed discussion on the research progress and achievements.

Elements of this chapter will be submitted soon:

- **Dong, H., G.,** Koenig, Jr., G. M. Coprecipitation as a Robust and Versatile Method to Synthesize Precursors for Good-Performing Lithium-ion Battery Cathode Active Materials: A Review. In Preparation.

1.2. Introduction

Interest in developing high energy, high power, and safe electrochemical energy storage has motivated research in battery technologies for many decades [1–5]. Lithium-ion (Li-ion) rechargeable batteries, since their commercialization by Sony in the early 1990s, has received much attention over the last three decades due to the intrinsically high volumetric and gravimetric energy density and also excellent charge/discharge efficiency and cycle life [6]. While in most cases commercial cells use similar active material cell chemistry of a graphite anode and layered transition metal oxide cathode [7–10], many methods have been developed to synthesize these electroactive materials with the goal of controlling over the particle composition, morphology, and surface functionality [11–19]. The motivation to have exquisite control over active material composition and morphology are that the performance of the final assembled battery cell is highly sensitive to these parameters – both due to the properties of the individual particles themselves and due to the sensitivity to their organization within the electrode [17,20–24].

One of the methods very popular to produce Li-ion battery active materials is coprecipitation. Coprecipitation is very popular due to its simplicity, scalability, homogeneous mixing in atomic scale, and particle morphology control [25–27]. The process of using coprecipitation to synthesize battery active materials usually contains two steps: first the formation of particles from a coprecipitation reaction which are normally referred to as precursors; then the blending of the precursor with a lithium source and calcination into final active materials which can be conducted at a wide range temperatures and atmospheres depending on specific final material desired [28–32]. Due to homogeneous mixing at the atomic scale provided by the coprecipitation reaction, relatively mild calcination temperatures and holding times are needed to form the final product with its target phase and crystallinity

[28]. The relatively mild calcination conditions are also beneficial for retaining the secondary morphology of the original precursor particles, although the surface roughness and/or primary particles that make up the secondary particles are often modified due to decomposition of some of the precursor particle constituents [33]. The precursor decomposition can also result in internal porosity, the structure and degree of which is highly sensitive to the precursor material chemistry and the calcination conditions [17,34,35]. Coprecipitation for production of battery materials is often conducted in batch processes in the literature, but the process has also been reported using continuous reactor systems which are highly scalable for mass production of battery active material powders [28,36]. There are many controllable parameters for coprecipitation synthesis that can significantly impact the composition and morphology of the particles, including temperature, pH, concentration of both species that participate in the precipitation and their counter ions in solution, stirring rate and mixing within the reactor, mixing method, rate of reactant feed, and the use of additives that modify the particle morphology such as chelating agents [37–40]. The variety of coprecipitation chemistry and reaction conditions have resulted in many different particle morphologies including spheres, cubes, rods, plates, hollow spheres, dumbbells, rhomboids, and others [41–51]. Some of these particle morphologies are shown in Figure 1. Thus far, detailed knowledge of the fundamental processes that would enable rational and predictive control of final particle composition and morphology that includes solution chemistry, process variables, and particle nucleation and growth has been lacking, but some efforts have been made to tackle some aspects towards achieve this outcome such as probing the impact of solution chemistry equilibrium on particle morphology or detailed process optimization reports [37–40,52,53].

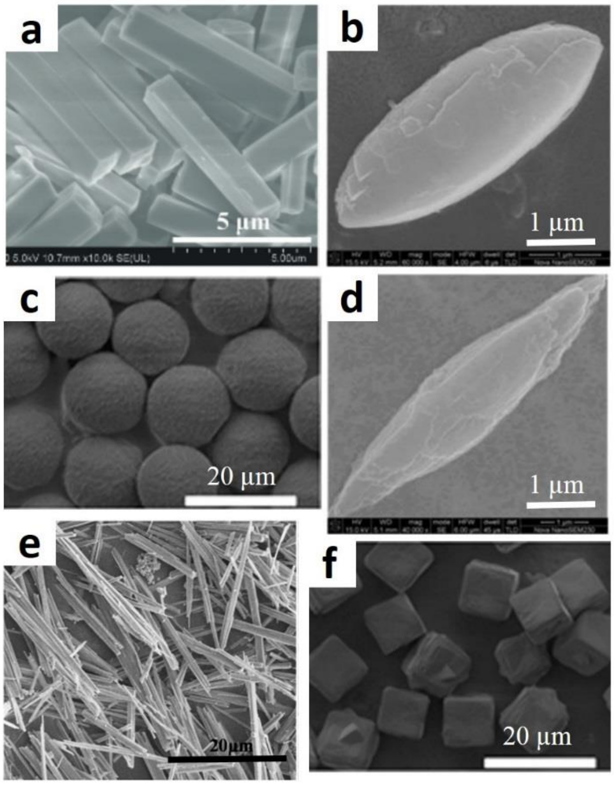

Figure 1. Different particle morphologies obtained from coprecipitation reactions under different solution conditions for the use of battery active materials synthesis. a) [48], b,d) [44], c,f) [51], e) [54].

The study of coprecipitation broadly is very old and has been well used in metal mining, water treatment, catalyst, pharmacy, et al. [55–58]. However, the use of coprecipitation as a popular method for the synthesis of Li-ion battery materials has been more recent and largely followed after the commercialization of the first Li-ion battery. While solid-state and sol-gel synthesis were among the most common for producing Li-ion materials in the early literature and are still common today, coprecipitation has grown in popularity in particular over the last 15-20 years. A Web of Science^{TM} topical search including “precipitation”, “lithium”, and “battery” in February 2019 found 921 publications, with 5 or less from 1995-2001 and rising to the highest value of 123 in the most recent year of 2018. This review will introduce a brief overview of some of the earliest coprecipitation papers in the Li-ion battery literature in the second section, which often promoted the advantages of coprecipitation compared to more common synthesis methods such as solid-state and spray pyrolysis. In the third section, the three most common types of coprecipitation will be discussed and compared: hydroxide, carbonate, and oxalate. The disadvantages and major concerns when using coprecipitation to synthesize materials will also be described, and the superiority of oxalate coprecipitation can be seen. Equilibrium and kinetic studies will be summarized in the fourth section, which also covered the known mechanisms of particle morphology control by using chelating agent. The challenge of particle morphology control in oxalate coprecipitation is also briefly discussed. In the final section, research overview and organization of this dissertation will be provided.

1.3. Coprecipitation of Transition Metals with Different Anions

Hydroxide coprecipitation is the earliest developed coprecipitation method used for TM oxide battery materials synthesis [59–62]. Chelating agents, such as ammonia and ammonium salts, were generally used to assist the production of dense spherical particles [63]. Hydroxide precipitates were reported with homogeneous cation mixing and monodispersity with regards to particle shape and particle size distribution [28,32,64]. Detailed discussion of particle morphology control through reaction conditions using coprecipitation will be covered in Section 4. Hydroxide coprecipitation does have some challenges: 1) Mn^{2+} will be oxidized to Mn^{3+} and Mn^{4+} in the presence of oxygen in air, forming MnOOH and MnO_2 impurities; 2) to prevent the formation of oxidized Mn impurity phases, the coprecipitation must be carried out in an inert atmosphere which adds complexity to the process; and 3) reproducibility of particle morphologies can be low due to the sensitivity of the particle nucleation and growth process to the solution conditions.

In 2002 Lee *et al*. published one of the earliest reports using carbonate coprecipitation to synthesize battery precursor particles [65]. The carbonate precursor was used to synthesize the high voltage spinel structure cathode material $LiMn_{1.5}Ni_{0.5}O_4$ (LMNO). In the synthesis, an ammonium carbonate solution and a TM solution containing appropriate stoichiometric feed amounts of Mn and Ni (3:1 Mn:Ni) dissolved from sulfate salts were poured into a reactor with heating at 80° C. The precipitates were then filtered, washed, and preheated at 600° C. Then a stoichiometric amount (1:2 Li:TM) of Li was mixed with the obtained powder and calcined at properly high temperature to form the final oxide materials. No impurity phase was detected in the materials synthesized from the carbonate precursors. This was attributed to the homogeneous mixing between the TM ions from the coprecipitation process, whereas in the sol-gel process isolated Ni failed to substitute into the Li Mn spinel phase. SEM images showed the particles from coprecipitation were irregular secondary particles (3-4 um) composed of nano-sized primary particles (50-100 nm). In a follow up report，carbonate coprecipitation was applied to synthesize precursors used to make multi-component layered materials [13]. In these initial reports utilizing carbonate coprecipitations, particle size and shape control was not well defined. Also, in some cases the secondary particle aggregates would undergo significant fracture and break up of primary particles after the carbonate decomposition and calcination processes initiated via exposure to elevated temperatures. In later works relatively uniform particle shape was obtained with narrower size distribution [33,66]; however process variables that resulted in the more monodisperse particle morphologies were still under exploration. These early reports showed the possibility of particle morphology tuning by controlling the solution conditions from carbonate coprecipitation. And even though many of the precipitate particles had a relatively wide size distribution with irregular shapes, the aggregates become more uniform in shape and more densely packed with the aid of chelating agents [67,68]. The micrometers-sized secondary particles comprised of hundreds of nanometers-sized primary particles as the final product exhibited structural stability and highly accessible surface area as cathode materials, resulting in encouraging electrochemical performance and rate capability [28,53,69,70].

Carbonate coprecipitation has the following advantages: 1) almost all the commonly used TM cations remain in the divalent oxidation state in carbonate coprecipitation solution within typical pH operating ranges; thus inert gas is not needed to assure phase purity of the product [33]; 2) the solution conditions of carbonate coprecipitation are relatively neutral with regards to pH. Later studies of carbonate coprecipitation have also mentioned some drawbacks of carbonate coprecipitation: 1) continuous growth of secondary particle sizes [71] in a continuous stirred tank reactor (CSTR) makes control of particle size monodispersity challenging; 2) the large particle size and large surface area makes the precursor samples vulnerable to moisture [72]; 3) composition deviation from the feed or designed ratio due to the different solubilities of the precipitates [22]. For example, the relatively stronger coordination of ammonia with nickel ions cause Ni-deficit in the coprecipitate sample when using ammonia as chelating agent [73]. 4) At high Ni compositions Ni impurity phases form [74]; 5) The larger carbonate constituent compared to hydroxide results in increased porosity on calcination to final active material. While this improves electrolyte accessibility to the particle interior which has advantages with regards to rate capability, the particle porosity makes them more susceptible to fracture during calendaring which is an important step in commercial electrode processing [71,75].

Oxalate has also been investigated as a coprecipitation agent with TM cations to produce battery precursors. In 2010 Park et al used oxalate coprecipitation to synthesize precursors for making multi-component olivine materials [31]. In this work the effect of the pH, atmosphere, temperature, and aging time was investigated with respect to the impacts on the atomic ratio of transition metals, phase purity, and morphology of the mixed TM oxalate. Significant Mn-deficiency was observed in this work due to the relative higher solubility of Mn oxalate, when oxalic acid and TM sulfate salts were used to produce the precursors; improvement in obtaining the target stoichiometry was achieved by using ammonium oxalate as the oxalate source, which increased the solution pH. For Co and Fe, the β-phase oxalate formation was found to be preferred during room temperature coprecipitation and α-phase oxalate formation was observed during high temperature coprecipitation (90°C); in contrast Mn only exhibited α-phase oxalate for all conditions. In order to produce a phase pure precursor with homogeneous mixing of multiple TM cations, temperature was maintained at 90°C in the binary system to avoid formation of Mn-rich α-oxalate and Mn-lean β-oxalate. Optimized samples from oxalate coprecipitation exhibited significant improvements in rate capability, which confirmed the importance of phase and compositional homogeneity for extracting the best electrochemical performance from the multi-component cathode materials. SEM images of final olivine samples from ammonium oxalate system showed nano-size crystals aggregated into irregular secondary structures. Mn-deficiency of the precipitate samples, especially in low pH conditions, was also studied by Wang et al. in 2013 [76]. They also reported that by using ammonium hydroxide as a pH adjuster and shifting the pH to near 7 the Mn to Ni ratio in the particles was much closer to the feed ratio in the synthesis of Li-rich Mn-rich layered cathode precursors. The final oxide particles were hierarchical structures with pores of regular patterns forming from aligned rod-like primary particles; the rod-cluster structure showed superiority over individual nano-sized primary particles produced after ball milling treatment with regards to both cycle life and rate capability.

In 2010 Wu *et al.* published on the use of oxalate coprecipitation to synthesize precursors for $xLi[Li_{1/3}Mn_{2/3}]O_2.(1 - x)LiNi_{1/2}Mn_{1/2}O_2$ [77]. The obtained particles showed irregular shapes, similar to sol-gel materials. In 2013 Zhu et al. developed a novel oxalate-carbonate composite coprecipitation to synthesize precursors for the production of LMNO [73]. The stronger coordination of ammonia with Ni ions was known to result in Ni-deficit in the carbonate precipitate materials. Since both Ni and Mn oxalates have very little solubility in aqueous solution, ammonia had no obvious effect in bonding with either TM cations, and experimental results showed that with ammonium oxalate as the precipitation reagent the obtained coprecipitate samples had stoichiometry almost the same as the feed. However, without the chelating effect of dissolving and modifying the particles from ammonia, the obtained particles from pure oxalate precipitation were non-spherical; spherical and stoichiometric particles were obtained by adding small amount of ammonium carbonate to oxalate coprecipitation.

Oxalate coprecipitation has a few advantages over hydroxide and carbonate coprecipitation: 1) oxalate ions in the solution play a dual role as both a precipitation agent and a complexing agent-- the formation of metal complexes slows down the precipitation rate and makes the nucleation and growth of the particles more controllable [73]; 2) most TMs used in cathode materials, including Ni, Co, Mn, and their blends, form stable oxalate dihydrates across the entire range of mixing ratios [76,78], which results in high purity precursors with homogeneous mixing across a wide range of compositional space. It is important though to be aware that although the TMs all form oxalate dehydrates, different crystallographic structures may form under different temperatures and pressures [79–81]. Proper solution conditions must be chosen to prevent phase separation [18,76]. Oxalate precipitation also has some challenges. 1) Compositional deviations can occur between the precursor and the initial solution feed composition. The issue of composition deviation from the feed also occurs for hydroxide and carbonate coprecipitation [28]; however, hydroxide and carbonate typically operate at higher total concentrations and higher precipitate yields, which mitigates the compositional deviation to the extent that it is often ignored in those systems. Compositional deviation from the feed can be significant when the reaction is conducted in low concentration regimes where slow precipitation rate is desired to control and tune precipitate growth and morphology [22,51]. Tuning the solution feeding ratio to target on the final desired composition in the precursor has been used to improve material purity and electrochemical performance [22]. 2) Oxalate salts have relatively low solubility in aqueous solution, which limits the utility of chelation agents as particle morphology modifier to make spherical particles [73]. Other chelating agents other than ammonia may be found which improve the particle morphology [82]; 3) oxalate salts and oxalic acid have relatively lower solubilities than hydroxide and carbonate species, which may limit the precipitate yield and production rates. 4) While many TMs are stable for oxalate coprecipitation in air, others require an inert atmosphere – in particular Fe^{2+} ions were reported to readily be oxidize to Fe^{3+} and result in iron deficiency for oxalate coprecipitation with this TM in air [31].

Oxalate coprecipitation has been considered as the next generation coprecipitation method for synthesis of battery active materials with its obvious advantages over hydroxide and carbonate coprecipitations especially in structural stability, and particle morphology tunability. The focus of this dissertation is to systematically probe into the solution chemistry of multicomponent oxalate coprecipitation reaction with the purpose of solving the problem of composition deviation and inhomogeneity while exploring its morphology tuning possibility.

1.4. Fundamental solution chemistry and nucleation and growth studies

Fundamental study of the coprecipitation reaction solution chemistry and complexes and nucleation and particle growth processes are important to understand and eventually control the resulting precipitate composition and morphology. Often the target is dense spherical particles to obtain high tap density and electrode loading, but many other morphologies have been reported to have desirable electrochemical performance [24,51,83,84]. In addition, explicit compositional control is needed both to achieve target compositions with high accuracy and reproducibility and to obtain more complex particles that have variation in composition within the particles.

1.4.1. Solution equilibrium study

Van Bomme *et al.* previously reported the use of equilibrium calculations to study the effect of pH on particle morphologies in a mixed TM hydroxide reaction system with ammonia as the chelating agent [52]. By using the system of equations that included equilibrium constants and mole balance equations, they predicted the concentration of metal-ammonia complexes for both pure and mixed transition metal systems. The experimentally obtained tap densities from particles synthesized at different pH were then compared in the context of the regimes where the pH resulted in different extents of TM complexation. Spherical dense hydroxide is produced in the pH range where ammonia complexation was calculated to be significant – while at pH values where little complexation was calculated the resulting particles were very small and irregular and had low tap density. This study was one of the first few that integrated solution chemistry calculations with predictions on the final physical properties or morphologies of the resulting precipitate particles. In 2011, Wang et al. used equilibrium calculations on a carbonate coprecipitation process in a blend solution of Mn and Ni to guide the selection of solution conditions [71]. The residual TM concentration in the solution was calculated as a function of pH and it was determined that the pH range of 7.5 to 8.5 would minimize the residual TM concentration that did not precipitate to the solid phase. Lower pH was predicted to inhibit complete carbonate precipitation reaction while higher pH would increase the residual transition metal due to the formation of ammonia complexes, and even higher pH would result in hydroxide coprecipitation. These two studies are examples of some of the few cases where solution equilibrium calculations were explicitly used to guide the optimization of coprecipitation reaction conditions.

In 2015, Robinson *et al.* published a work on the tunability of particle morphology in manganese carbonate coprecipitation [51], in which equilibrium calculations were used to determine the amount of ammonia complex formation in the solution at different NH_4HCO_3 to Mn^{2+} ratios. It should be noted that NH_4HCO_3 could function both as the coprecipitation agent and as the chelating agent – with NH_4^+ providing the complexing NH_3 and CO_3^{2-} serving as the coprecipitation anion. Equilibrium calculations determined that less than 0.1% of the feed Mn kept in the solution as a soluble complex at equilibrium across a wide range of solution conditions, and that the residual manganese concentration decreased as the relative or absolute NH_4HCO_3 amount increased. This outcome was largely due to the relatively neutral pH of the solution, which resulted in NH_4^+ being the dominant species in the ammonia/ammonium equilibrium and thus relatively small amounts of NH_3 were available to form $Mn(NH_3)_n^{2+}$ complexes. Although the NH_3 complexation was low as determined by equilibrium calculations, substitution of NH_4HCO_3 with $NaHCO_3$ as the coprecipitation agent changed the particle morphology changed from cubic to spherical suggesting that even small amounts of complexation of TM may have significant impacts on the initial particle nucleation stage.

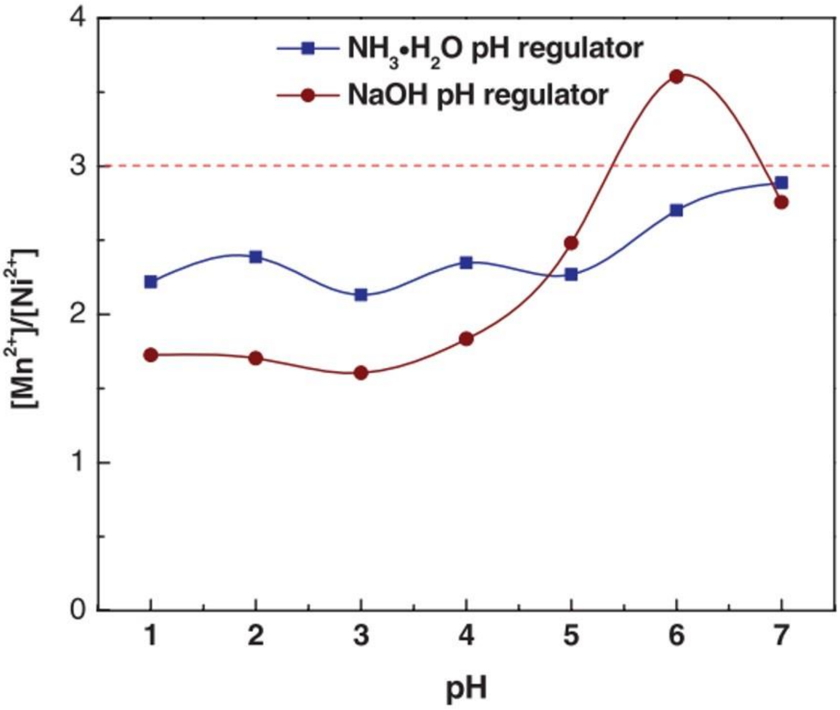

Figure 2. ICP-MS measured Mn/Ni atomic ratio in the precipitated particles from 3:1 feed solution as a function of reaction pH. [76]

Wang *et al.* applied equilibrium calculations to oxalate coprecipitation in a solution containing both Mn and Ni [76]. Oxalic acid was used as the coprecipitation reagent and either ammonia or hydroxide was used to control the solution pH. Both equilibrium calculations and experiments revealed that there was an optimal pH range to maximize the conversion of the TM cations to the solid phase precipitates. Calculation results indicated that the residual Mn in the solution phase was four times that of the residual Ni at all pH values due to differences in solubility, which resulted in the Mn:Ni ratio in the obtained precipitates lower than the feed ratio (as shown in Figure 2, the higher than feed Mn:Ni ratio at pH of 6 with NiOH as pH controller was due to the formation of hydroxide precipitates). These composition deviations were not well compensated by the addition of ammonia even though ammonia coordinates more Ni than Mn, keeping more Ni residual in the solution as soluble species.

1.4.2. Kinetic study of coprecipitation

Understanding the kinetics of the nucleation and particle growth for both single and multicomponent TM solutions are also critical for rational and explicit control of particle composition and morphology. Some reports have developed models to describe the reaction, nucleation, and particle growth process of the coprecipitation system [85,86]; however coprecipitation is a complex process where conditions such as pH, concentration, temperature, complexing agents, morphology-directing agents, and stirring rate can all significantly impact final particle yield, composition, and morphology. Changes to the reagent feeding rates and mixing methods, the composition of the reactants and product particles, smoothness of the reactor surface and the abovementioned factors may direct the nucleation towards a different path (homogeneous nucleation or heterogeneous nucleation) or the particle growth towards different driving forces (diffusion controlled or surface controlled). This complexity likely underlies why there have been very few studies which develop a model in the coprecipitation synthesis for battery materials, because developing a broadly applicable model to many experimental conditions would be challenging [71]. Even experimental studies aimed at gaining kinetic information are generally qualitative or semi-quantitative. In part this is due to the disparate length (from nanometers initial or pre-nuclei to submicron primary particles to tens of micrometers secondary particles) and time (from the rare event and fractions of a second initial nucleation to the many hours precipitation process; or possibly longer for continuous reactor operations) scales.

Van Bomme *et al.* tracked the tap density and particle morphology of $Ni(OH)_2$ particles as a function of time in a CSTR coprecipitation reactor [52]. It was found that the tap density of the particles gradually increased and then plateaued after ~10 hours at ~2 g cm^{-3}. The gradual formation of spherical particles which became larger and smoother over the first 10 hours of the process, as revealed with SEM, was given as the explanation for the tap density observations. Wang et al. also used SEMs from particles at different reaction times in a carbonate coprecipitation study [71], and similarly it was found that the formation of dense, smooth, spherical particles took ~8 hours. Particles collected <1 hour after initiation of the reaction were particularly irregular with wide size distributions of the secondary particles from 1 to 80 μm. Within the limits of the reaction time in this study in a CSTR, it was also found that the secondary particles continued to increase in diameter for the entirety of the process. These studies provided valuable insights into the coprecipitation timescale to achieve dense and spherical particles with both hydroxide and carbonate processes, although the systems were limited to a specific subset of experimental conditions. Note that in both of these studies the CSTR starts with a TM concentration (of both feed or soluble species and precipitates) of zero and thus part of the increase in particle size and tap density is the reactor reaching steady state with regards to concentration of total TM and coprecipitation anion.

1.4.3. Particle Morphology Control

Samsung SDI Co. published one of the earlier studies of the impact of ammonia as a chelating agent in hydroxide coprecipitation [34]. The report took advantage of ammonia to control the precipitate particle growth, and a patent was also filed on this process [63,87]. The function of ammonia was explained using the following reaction sequence (rearranged to a general form, M represents all possible transition metal ions):

$$M^{2+} + xNH_4OH(aq) \rightarrow M(NH_3)_n^{2+}(aq) + xH_2O \qquad [1]$$

$$M(NH_3)_n^{2+}(aq) + yOH^- = M(OH)_2(s) + nNH_3 \qquad [2]$$

In the proposed mechanism, ammonia forms complexes with TM ions in the solution, which then gradually react with hydroxide ions to form precipitates.

In the report, the pH was controlled and maintained by adding NaOH throughout the process. The obtained particles were sphere-like secondary particles composed of primary particles of sub-micron size, and the particle size of the secondary particles ranged from 5- 30 in a typical population. The next year Ying et al. published a work on ‘Controlled crystallization’ also using ammonia as the chelating agent in hydroxide coprecipitation to synthesize Co and Ni hydroxide particles [88]. The paper reported that with the aid of ammonia it was possible to increase the tap density of cathode materials without sacrificing the specific capacity by controlling particle morphology and size distribution. The obtained regular spherical hydroxide particles and final oxide particles were synthesized by using the chelating agent and the effect of ammonia concentration on particle morphologies was investigated. It was found that the particles became more spherical and had a narrower size distribution, which gave higher tap density, when higher concentrations of ammonia were used. The optimized particles (pH 11.5 C_{NH3} 0.6 M, having particle size 5-15 um), after conversion to layered oxide active material, surpassed the tap density and specific capacity of commercial reference materials when compared in battery cells. A later work published by Lee et al. in 2004 also reported the most regular spherical particles with the narrowest size distribution resulted in their study when the highest amount of ammonia, the lowest pH, and the highest stirring speed was used within their investigation ranges (with the ranges being 0.12-0.36 M ammonia, pH 11-12, and stir rate of 400-1000 rpm) [89].

Chelating agents were also applied in synthesis of battery precursors using the carbonate coprecipitation system. In 2005 in a paper from Park et al., carbonate coprecipitation was modified by the addition of $NH_3.H_2O$ as the chelating agent, and regular spherical-shaped coprecipitate particles with relatively monodisperse size of around 10 um were obtained. The particles well-retained the secondary morphology of the precursor after high temperature calcination and annealing processes [90]. The improved uniformity of the obtained particles was explained as resulting from the use of the chelating agent according to similar mechanism as stated in Samsung's work [63], functioning to prevent phase separation and to facilitate the formation of homogeneous and uniform particles.

While many of the previous reports focused on the hypothesis that the slow growth and dense hydroxide particles resulted from the ammonia complexing TM and slowly releasing the complex to the hydroxide solid phase (see Equations 1 and 2), Bommel et al. published a study that highlighted a different process [64]. In this report, the slow growth and high tap density precipitate particles were attributed to the equilibrium between TM hydroxide particles and aqueous ammonia TM complexes in solution as shown below:

$$M(OH)_2 + nNH_3 \leftrightarrow [M(NH_3)_n]^{2+} + 2OH^- \quad [3]$$

It was found that dense spherical particles only grew in the pH range where metal ions coordinated with ammonia, and the chelation effect was speculated to result in a dynamic dissolution-recrystallization of the hydroxide that resulted in lower particle internal porosity and higher tap density. The authors suggested that both the release of the complexed ammonia to the hydroxide and the dissolution-recrystallization was occurring during the coprecipitation reaction [51] . And the depending on the bounding strength between the complexes and the precipitate particles, a certain chelating agent has different effect in tuning the particle morphologies.

It is noted briefly that while ammonia is the most common chelation agent used in coprecipitation synthesis of battery precursor particles, others have also been explored. For example, Zhang et al. used poly(ethylene glycol) (PEG) to facilitate oxalate coprecipitation [82]. Oxalate itself forms complexes with TMs commonly used in battery precursor coprecipitation and thus can serve a similar function to a chelation agent at relatively low TM concentrations [73]. It should be noted though that ammonia cannot function as an effective agent for synthesizing spherical precipitate particles in oxalate coprecipitation due to the low solubilities of most TM oxalate salts which results in minimum ammonium complexes formation and negligible dissovation and dissolution-recrystallization process. Therefore, other chemical inhibitors will be needed for particle morphology tuning or modification in TM oxalate coprecipitation.

1.5. Scope of Dissertation

The goal of this work is to gain deep insights into the solution chemistry that control the composition and particle morphology of the particles in multicomponent coprecipitations. Such knowledge would make it possible to design and predictively control the composition and morphology of the precipitates particles in order to get optimal performances of final active materials in energy storage application. Even though there have been a lot of reports about the characterization of TM oxide active materials, limited research has been published about the study of either the crystallization and particle growth process of coprecipitation reaction or the properties of the precursor particles. This dissertation focuses on both solution and particle evolution as a function of reaction time, and also discovers well applicable tools to study coprecipitation reactions for wide variety of applications. Emphasis is also given to the optimization of electrochemical performance of battery active materials synthesized from coprecipitation.

Each of the following chapter is comprised of one of our published work, except for the last chapter which only contains some preliminary results. Chapter 2 is about *in-situ* tracking the solution concentrations as a way to track the reaction extent of each TM ion in the blend coprecipitation solution. The problem revealed in Chapter 2 about composition deviation is further characterized in Chapter 3, and put into context of the homogeneous mixing from coprecipitation reaction compared to solid-state reaction. Chapter 4 is about *in-situ* measuring the particle size distribution along the coprecipitation reaction, which, combined with the results from Chapter 2, gives insights into the mechanisms of particle nucleation and growth for different TM ion coprecipitation and their interactions in the blend solution. In chapter 5, a more quantitative descriptor of the coprecipitation reaction, apparent activation energy, is measured along the whole composition range of the binary reaction system, and found to be a promising tool to detect new phase formation in the precipitated particles. Chapter 6 discusses the possibility of electrode tortuosity control by particle alignment during the process of electrode assembly, using the special shaped particles synthesized from coprecipitation solution. Future works that need to be done to achieve the overall goal of predictive control the composition, morphology, and phase purity of the particles are also talked about in the last chapter.

1.6. Reference

[1] J.B. Goodenough, Y. Kim, Challenges for rechargeable Li batteries, Chem. Mater. 22 (2010) 587–603. doi:10.1021/cm901452z.

[2] Y.K. Sun, S.T. Myung, B.C. Park, J. Prakash, I. Belharouak, K. Amine, High-energy cathode material for long-life and safe lithium batteries, Nat. Mater. 8 (2009) 320–324. doi:10.1038/nmat2418.

[3] M. Hu, X. Pang, Z. Zhou, Recent progress in high-voltage lithium ion batteries, J. Power Sources. 237 (2013) 229–242. doi:10.1016/j.jpowsour.2013.03.024.

[4] E. Vinodkumar, R. Marom, R. Elazari, G. Salitra, D. Aurbach, Challenges in the development of advanced Li-ion batteries: a review, Energy Environ. Sci. 4 (2011) 3243–3262. doi:10.1039/c1ee01598b.

[5] R. Marom, S.F. Amalraj, N. Leifer, D. Jacob, D. Aurbach, A review of advanced and practical lithium battery materials, J. Mater. Chem. 21 (2011) 9938–9954. doi:10.1039/C0JM04225K.

[6] R. Van Noorden, The rechargeable revolution: A better battery, Nature. 507 (2014) 26–28. doi:10.1038/507026a.

[7] T. Ohzuku, A. Ueda, M. Nagayama, Y. Iwakoshi, H. Komori, Comparative study of LiCoO2, LiNi12Co12O2 and LiNiO2 for 4 volt secondary lithium cells, Electrochim. Acta. 38 (1993) 1159–1167. doi:10.1016/0013-4686(93)80046-3.

[8] J.M. Tarascon, The Spinel Phase of LiMn[sub 2]O[sub 4] as a Cathode in Secondary Lithium Cells, J. Electrochem. Soc. 138 (1991) 2859. doi:10.1149/1.2085330.

[9] R.J. Gummow, M.M. Thackeray, Lithium-cobalt-nickel-oxide cathode materials prepared at 400°C for rechargeable lithium batteries, Solid State Ionics. 53–56 (1992) 681–687. doi:10.1016/0167-2738(92)90447-W.

[10] Q. Zhong, A. Bonakclarpour, M. Zhang, Y. Gao, J.R. Dahn, Synthesis and Electrochemistry of LiNixMn2-xO4, J Electrochem Soc. 144 (1997) 205–213. doi:10.1149/1.1837386.

[11] D. Guan, C. Cai, Y. Wang, Enhanced cycleability of LiMn2O4 cathodes by atomic layer deposition of Al2O3 coatings, 2011 IEEE Green Technol. Conf. Green 2011. (2011) 1465–1469. doi:10.1109/GREEN.2011.5754875.

[12] F. Wu, Z. Wang, Y. Su, Y. Guan, Y. Jin, N. Yan, J. Tian, L. Bao, S. Chen, Synthesis and characterization of hollow spherical cathode Li1.2Mn0.54Ni0.13Co0.13O2 assembled

with nanostructured particles via homogeneous precipitation-hydrothermal synthesis, J. Power Sources. 267 (2014) 337–346. doi:10.1016/j.jpowsour.2014.05.097.

[13] S.-M. Park, T.-H. Cho, M. Yoshio, Novel Synthesis Method for Preparing Layered Li[Mn 1/2 Ni 1/2]O 2 as a Cathode Material for Lithium Ion Secondary Battery, Chem. Lett. 33 (2004) 748–749. doi:10.1246/cl.2004.748.

[14] L. Li, S. Song, X. Zhang, R. Chen, J. Lu, F. Wu, K. Amine, Ultrasonic-assisted co-precipitation to synthesize lithium-rich cathode Li1.3Ni0.21Mn0.64O2+d materials for lithium-ion batteries, J. Power Sources. 272 (2014) 922–928. doi:10.1016/j.jpowsour.2014.08.063.

[15] G.M. Koenig, I. Belharouak, H.M. Wu, K. Amine, Hollow lithiated metal oxide particles as lithium-ion battery cathode materials, Electrochim. Acta. 56 (2011) 1426–1431. doi:10.1016/j.electacta.2010.10.066.

[16] I. Belharouak, G.M. Koenig, K. Amine, Electrochemistry and safety of Li4Ti5O12 and graphite anodes paired with LiMn2O4 for hybrid electric vehicle Li-ion battery applications, J. Power Sources. 196 (2011) 10344–10350. doi:10.1016/j.jpowsour.2011.08.079.

[17] C.J. Bae, C.K. Erdonmez, J.W. Halloran, Y.M. Chiang, Design of battery electrodes with dual-scale porosity to minimize tortuosity and maximize performance, Adv. Mater. 25 (2013) 1254–1258. doi:10.1002/adma.201204055.

[18] H. Dong, G.M. Koenig, Compositional control of precipitate precursors for lithium-ion battery active materials: Role of solution equilibrium and precipitation rate, J. Mater. Chem. A. 5 (2017). doi:10.1039/c7ta03653a.

[19] C. Tan, H. Luo, K. Du, D. Huang, K. Hu, Core-shell structured Li[(Ni0.9Co0.05Al0.05)0.6(Ni0.4Co0.2Mn0.4)0.4]O2 cathode material for high-energy lithium ion batteries, 6 (2018) 1293–1304.

[20] M. Ebner, D.W. Chung, R.E. García, V. Wood, Tortuosity anisotropy in lithium-ion battery electrodes, Adv. Energy Mater. 4 (2014) 1–6. doi:10.1002/aenm.201301278.

[21] J. Billaud, F. Bouville, T. Magrini, C. Villevieille, A.R. Studart, Magnetically aligned graphite electrodes for high-rate performance Li-ion batteries, Nat. Energy. 1 (2016) 1–13. doi:10.1038/nenergy.2016.97.

[22] H. Dong, G.M. Koenig Jr, Compositional control of precipitate precursors for lithium-ion battery active materials: role of solution equilibrium and precipitation rate, J. Mater. Chem. A. 5 (2017) 13785–13798. doi:10.1039/C7TA03653A.

[23] R. Thirunakaran, G.H. Lew, W.S. Yoon, Cerotic acid assisted sol-gel synthesis and electrochemical performance of double doped spinels (LiCrxMgyMn2-x-yO4) as cathode materials for lithium rechargeable batteries, Powder Technol. 301 (2016) 197–210. doi:10.1016/j.powtec.2016.05.064.

[24] L. Zhang, W. Borong, L. Ning, W. Feng, Hierarchically porous micro-rod lithium-rich cathode material Li1.2Ni0.13Mn0.54Co0.13O2 for high performance lithium-ion batteries, Electrochim. Acta. 118 (2014) 67–74. doi:10.1016/j.electacta.2013.11.186.

[25] H. Li, Q. Xu, X.-X. Shi, D.-W. Song, L.-Q. Zhang, Electrochemical performance of LiNi0.5Mn0.5O2 with different synthesis methods, Rare Met. 34 (2015) 580–585. doi:10.1007/s12598-013-0088-z.

[26] H. Dong, A. Wang, G.M. Koenig, Role of coprecipitation and calcination of precursors on phase homogeneity and electrochemical properties of battery active materials, Powder Technol. 335 (2018). doi:10.1016/j.powtec.2018.05.020.

[27] M. a. Valenzuela, P. Bosch, G. Aguilar-Rios, a. Montoya, I. Schifter, Comparison between sol-gel, coprecipitation and wet mixing synthesis of ZnAl2O4, J. Sol-Gel Sci. Technol. 8 (1997) 107–110. doi:10.1007/BF02436826.

[28] D. Wang, I. Belharouak, G.M. Koenig, G. Zhou, K. Amine, Growth mechanism of Ni0.3Mn0.7CO3 precursor for high capacity Li-ion battery cathodes, J. Mater. Chem. 21 (2011) 9290. doi:10.1039/c1jm11077b.

[29] J.-H. Ju, K.-S. Ryu, Synthesis and electrochemical performance of Li(Ni0.8Co0.15Al0.05)0.8(Ni0.5Mn0.5)0.2O2 with core–shell structure as cathode material for Li-ion batteries, J. Alloys Compd. 509 (2011) 7985–7992. doi:10.1016/j.jallcom.2011.05.060.

[30] Y. Fan, J. Wang, X. Ye, J. Zhang, Physical properties and electrochemical performance of LiNi0.5Mn1.5O4 cathode material prepared by a coprecipitation method, Mater. Chem. Phys. 103 (2007) 19–23. doi:10.1016/j.matchemphys.2006.10.006.

[31] Y.U. Park, J. Kim, H. Gwon, D.H. Seo, S.W. Kim, K. Kang, Synthesis of multicomponent olivine by a novel mixed transition metal oxalate coprecipitation method and electrochemical characterization, Chem. Mater. 22 (2010) 2573–2581. doi:10.1021/cm903616d.

[32] Y. Kim, D. Kim, Synthesis of high-density nickel cobalt aluminum hydroxide by continuous coprecipitation method, ACS Appl. Mater. Interfaces. 4 (2012) 586–589. doi:10.1021/am201585z.

[33] T.H.H. Cho, S.M.M. Park, M. Yoshio, T. Hirai, Y. Hideshima, Effect of synthesis condition on the structural and electrochemical properties of Li[Ni1/3Mn1/3Co1/3]O2prepared by carbonate co-precipitation method, J. Power Sources. 142 (2005) 306–312. doi:10.1016/j.jpowsour.2004.10.016.

[34] Y.K. Sun, S.T. Myung, M.H. Kim, J. Prakash, K. Amine, Synthesis and characterization of Li[(Ni0.8Co 0.1Mn0.1)0.8(Ni0.5Mn 0.5)0.2]O2 with the microscale core-shell structure as

the positive electrode material for lithium batteries, J. Am. Chem. Soc. 127 (2005) 13411–13418. doi:10.1021/ja053675g.

[35] S.M. Oh, S.T. Myung, J.B. Park, B. Scrosati, K. Amine, Y.K. Sun, Double-structured LiMn 0.85Fe 0.15PO 4 coordinated with LiFePO 4 for rechargeable lithium batteries, Angew. Chemie - Int. Ed. 51 (2012) 1853–1856. doi:10.1002/anie.201107394.

[36] D. Wang, I. Belharouak, L.H. Ortega, X. Zhang, R. Xu, D. Zhou, G. Zhou, K. Amine, Synthesis of high capacity cathodes for lithium-ion batteries by morphology-tailored hydroxide co-precipitation, J. Power Sources. 274 (2015) 451–457. doi:10.1016/j.jpowsour.2014.10.016.

[37] M.H. Kim, H.S. Shin, D. Shin, Y.K. Sun, Synthesis and electrochemical properties of Li[Ni0.8Co0.1Mn0.1]O2and Li[Ni0.8Co0.2]O2via co-precipitation, J. Power Sources. 159 (2006) 1328–1333. doi:10.1016/j.jpowsour.2005.11.083.

[38] S.-M. Oh, S.-T. Myung, Y.S. Choi, K.H. Oh, Y.-K. Sun, Co-precipitation synthesis of micro-sized spherical LiMn0.5Fe0.5PO4 cathode material for lithium batteries, J. Mater. Chem. 21 (2011) 19368. doi:10.1039/c1jm13889h.

[39] D.-K. Lee, S.-H. Park, K. Amine, H.J. Bang, J. Parakash, Y.-K. Sun, High capacity Li[Li0.2Ni0.2Mn0.6]O2 cathode materials via a carbonate co-precipitation method, J. Power Sources. 162 (2006) 1346–1350. doi:10.1016/j.jpowsour.2006.07.064.

[40] J.-H. Lim, H. Bang, K.-S. Lee, K. Amine, Y.-K. Sun, Electrochemical characterization of Li2MnO3–Li[Ni1/3Co1/3Mn1/3]O2–LiNiO2 cathode synthesized via co-precipitation for lithium secondary batteries, J. Power Sources. 189 (2009) 571–575. doi:10.1016/j.jpowsour.2008.10.035.

[41] H.B. Lin, J.N. Hu, H.B. Rong, Y.M. Zhang, S.W. Mai, L.D. Xing, M.Q. Xu, X.P. Li, W.S. Li, Porous LiMn2O4 cubes architectured with single-crystalline nanoparticles and

exhibiting excellent cyclic stability and rate capability as the cathode of a lithium ion battery, J. Mater. Chem. A. 2 (2014) 9272–9279. doi:10.1039/c4ta01474j.

[42] N. Wu, H. Wu, W. Yuan, S. Liu, J. Liao, Y. Zhang, Facile synthesis of one-dimensional LiNi0.8Co0.15Al0.05O2 microrods as advanced cathode materials for lithium ion batteries, J. Mater. Chem. A. 3 (2015) 13648–13652. doi:10.1039/c5ta02767e.

[43] L. Yi, Y. Wang, B. Wu, R. Yu, Z. Liu, M. Liu, X. Wang, X. Yang, X. Zhang, G. Wang, X. Xiong, M. Liu, Li 1.2 Ni 0.13 Co 0.13 Mn 0.54 O 2 with Controllable Morphology and Size for High Performance Lithium-Ion Batteries, ACS Appl. Mater. Interfaces. 9 (2017) 25358–25368. doi:10.1021/acsami.7b07095.

[44] B.-J. Hwang, K.-F. Hsu, S.-K. Hu, M.-Y. Cheng, T.-C. Chou, S.-Y. Tsay, R. Santhanam, Template-free reverse micelle process for the synthesis of a rod-like LiFePO4/C composite cathode material for lithium batteries, J. Power Sources. 194 (2009) 515–519. doi:10.1016/J.JPOWSOUR.2009.05.006.

[45] S. Li, G. Ma, B. Guo, Z. Yang, X. Fan, Z. Chen, W. Zhang, Kinetically Controlled Synthesis of LiNi0.5Mn1.5O4 Micro- and Nanostructured Hollow Spheres as High-Rate Cathode Materials for Lithium Ion Batteries, Ind. Eng. Chem. Res. 55 (2016) 9352–9361. doi:10.1021/acs.iecr.6b02463.

[46] C.-L. Xu, W. Xiang, Z.-G. Wu, Y.-D. Xu, Y.-C. Li, H.-T. Li, Y. Xiao, B.-C. Tan, X.-D. Guo, B.-H. Zhong, Hierarchical hollow structured lithium nickel cobalt manganese oxide microsphere synthesized by template-sacrificial route as high performance cathode for lithium ion batteries, J. Alloys Compd. 777 (2019) 434–442. doi:10.1016/J.JALLCOM.2018.10.380.

[47] G. Ma, S. Li, W. Zhang, Z. Yang, S. Liu, X. Fan, F. Chen, Y. Tian, W. Zhang, S. Yang, M. Li, A General and Mild Approach to Controllable Preparation of Manganese-Based Micro-

and Nanostructured Bars for High Performance Lithium-Ion Batteries, Angew. Chemie - Int. Ed. (2016) 3667–3671. doi:10.1002/anie.201511196.

[48] S. Huang, H. Wu, P. Chen, Y. Guo, B. Nie, B. Chen, H. Liu, Y. Zhang, Facile pH-mediated synthesis of morphology-tunable MnCO 3 and their transformation to truncated octahedral spinel LiMn2O4 cathode materials for superior lithium storage, J. Mater. Chem. A. 3 (2015) 3633–3640. doi:10.1039/C4TA06522K.

[49] S. Zhang, C. Deng, B.L. Fu, S.Y. Yang, L. Ma, Synthetic optimization of spherical Li[Ni1/3Mn1/3Co1/3]O2 prepared by a carbonate co-precipitation method, Powder Technol. 198 (2010) 373–380. doi:10.1016/j.powtec.2009.12.002.

[50] J.P. Robinson, G.M. Koenig, Tuning solution chemistry for morphology control of lithium-ion battery precursor particles, Powder Technol. 284 (2015) 225–230. doi:10.1016/j.powtec.2015.06.070.

[51] C. Zhao, X. Wang, R. Liu, F. Xu, Q. Shen, β-MnO<inf>2</inf> sacrificial template synthesis of Li <inf>1.2</inf>Ni<inf>0.13</inf>Co<inf>0.13</inf>Mn<inf>0.54</inf>O<inf>2</inf> for lithium ion battery cathodes, RSC Adv. 4 (2014) 7154–7159. doi:10.1039/c3ra45428b.

[52] A. Van Bomme, J.R. Dahn, Analysis of the growth mechanism of coprecipitated spherical and dense nickel, manganese, and cobalt-containing hydroxides in the presence of aqueous ammonia, Chem. Mater. 21 (2009) 1500–1503. doi:10.1021/cm803144d.

[53] S. Jouanneau, K.W. Eberman, L.J. Krause, J.R. Dahn, Synthesis, Characterization, and Electrochemical Behavior of Improved Li[Ni[sub x]Co[sub 1−2x]Mn[sub x]]O[sub 2] (0.1≤x≤0.5), J. Electrochem. Soc. 150 (2003) A1637. doi:10.1149/1.1622956.

[54] W. Song, P. Shen, H. Ma, J. Chen, J. Zhao, F. Cheng, C. Li, Facile Controlled Synthesis of MnO 2 Nanostructures of Novel Shapes and Their Application in Batteries, Inorg. Chem. 45 (2006) 2038–2044. doi:10.1021/ic051715b.

[55] M.A. McCaffrey, B. Lazar, H.D. Holland, The evaporation path of seawater and the coprecipitation of Br- and K+ with halite, J. Sediment. Res. 57 (1987) 928–937. doi:10.1306/212F8CAB-2B24-11D7-8648000102C1865D.

[56] A.I. Petrov, D. V. Volodkin, G.B. Sukhorukov, Protein-calcium carbonate coprecipitation: A tool for protein encapsulation, Biotechnol. Prog. 21 (2005) 918–925. doi:10.1021/bp0495825.

[57] M. Haruta, N. Yamada, T. Kobayashi, S. Iijima, Gold catalysts prepared by coprecipitation for low-temperature oxidation of hydrogen and of carbon monoxide, J. Catal. 115 (1989) 301–309. doi:10.1016/0021-9517(89)90034-1.

[58] Q. Chen, A.J. Rondinone, B. C. Chakoumakos, Z. John Zhang, Synthesis of superparamagnetic MgFe2O4 nanoparticles by coprecipitation, J. Magn. Magn. Mater. 194 (1999) 1–7. doi:10.1016/S0304-8853(98)00585-X.

[59] D. Caurant, N. Baffier, B. Garcia, J.P. Pereira-Ramos, Synthesis by a soft chemistry route and characterization of LiNixCo1−xO2 (0 ≤ x ≤ 1) cathode materials, Solid State Ionics. 91 (1996) 45–54. doi:10.1016/S0167-2738(96)00418-3.

[60] J.M. Paulsen, D. Larcher, J.R. Dahn, O2-Type Li2/3 [Ni1/3 Mn2/3]O2: A New Layered Cathode Material for Rechargeable Lithium Batteries II. Structure, Composition, and Properties, J. Electrochem. Soc. 147 (2000) 2862–2867.

[61] Z. Lu, J.R. Dahn, The Effect of Co Substitution for Ni on the Structure and Electrochemical Behavior of T2 and O2 Structure Li2 / 3 [CoxNi1 / 3 − xMn2 / 3] O 2, J. Electrochem. Soc. 148 (2001) A237. doi:10.1149/1.1350016.

[62] Z. Lu, D.D. MacNeil, J.R. Dahn, Layered Li[Ni[sub x]Co[sub 1−2x]Mn[sub x]]O[sub 2] Cathode Materials for Lithium-Ion Batteries, Electrochem. Solid-State Lett. 4 (2001) A200. doi:10.1149/1.1413182.

[63] J. Cho, LiNi0.74Co(0.26-x)Mg(x)O2 cathode material for a Li-ion cell, Chem. Mater. 12 (2000) 3089–3094. doi:10.1021/cm000153l.

[64] A. Van Bommel, J.R. Dahn, Analysis of the Growth Mechanism of Coprecipitated Spherical and Dense Nickel , Manganese , and Cobalt -Containing Hydroxides in the Presence of Aqueous Ammonia, Chem. Mater. 21 (2009) 1500–1503. doi:10.1021/cm803144d.

[65] Y.S. Lee, Y.K. Sun, S. Ota, T. Miyashita, M. Yoshio, Preparation and characterization of nano-crystalline LiNi0.5Mn1.5O4 for 5 V cathode material by composite carbonate process, Electrochem. Commun. 4 (2002) 989–994. doi:10.1016/S1388-2481(02)00491-5.

[66] T. Cho, S. Park, M. Yoshio, Preparation of Layered Li[Ni1⁄3Mn1⁄3Co1⁄3]O2 as a Cathode for Lithium Secondary Battery by Carbonate Coprecipitation Method, Chem. Lett. 33 (2004) 704–705. doi:10.1246/cl.2004.704.

[67] H. Groult, T. Nakajima, N. Kumagai, Characterization and Electrochemical Properties of LiNi0.5Mn1.5O4 Prepared by a Carbonate Co-Precipitation Method, Int. J. Electrochem. Sci. 9 (2014) 7712–7724.

[68] S. Zhang, C. Deng, S.Y. Yang, H. Niu, An improved carbonate co-precipitation method for the preparation of spherical Li[Ni1/3Co1/3Mn1/3]O2 cathode material, J. Alloys Compd. 484 (2009) 519–523. doi:10.1016/j.jallcom.2009.04.149.

[69] D. Liu, J. Han, J.B. Goodenough, Structure, morphology, and cathode performance of Li1-x[Ni0.5Mn1.5]O4 prepared by coprecipitation with oxalic acid, J. Power Sources. 195 (2010) 2918–2923. doi:10.1016/j.jpowsour.2009.11.024.

[70] E. Zhao, M. Chen, D. Chen, X. Xiao, Z. Hu, A Versatile Coating Strategy to Highly Improve the Electrochemical Properties of Layered Oxide LiMO2(M = Ni0.5Mn0.5and Ni1/3Mn1/3Co1/3), ACS Appl. Mater. Interfaces. 7 (2015) 27096–27105. doi:10.1021/acsami.5b08777.

[71] D. Wang, I. Belharouak, G.M. Koenig, G. Zhou, K. Amine, Growth mechanism of Ni0.3Mn0.7CO3precursor for high capacity Li-ion battery cathodes, J. Mater. Chem. 21 (2011) 9290–9295. doi:10.1039/c1jm11077b.

[72] D. Wang, I. Belharouak, S. Gallagher, G. Zhou, K. Amine, Chemistry and electrochemistry of concentric ring cathode Li1.42Ni0.25Mn0.75O2+γfor lithium batteries, J. Mater. Chem. 22 (2012) 12039–12045. doi:10.1039/c2jm31285a.

[73] Z. Zhu, D. Zhang, H. Yan, W. Li, Qilu, Precise preparation of high performance spherical hierarchical LiNi0.5Mn1.5O4 for 5 V lithium ion secondary batteries, J. Mater. Chem. A. 1 (2013) 5492. doi:10.1039/c3ta10980a.

[74] G.M. Koenig, I. Belharouak, H. Deng, Y.-K. Sun, K. Amine, Composition-Tailored Synthesis of Gradient Transition Metal Precursor Particles for Lithium-Ion Battery Cathode Materials, Chem. Mater. 23 (2011) 1954–1963. doi:10.1021/cm200058c.

[75] S.J. Harris, P. Lu, Effects of Inhomogeneities—Nanoscale to Mesoscale—on the Durability of Li-Ion Batteries, J. Phys. Chem. C. 117 (2013) 6481–6492. doi:10.1021/jp311431z.

[76] D. Wang, I. Belharouak, G. Zhou, K. Amine, Synthesis of Lithium and Manganese-Rich Cathode Materials via an Oxalate Co-Precipitation Method, J. Electrochem. Soc. 160 (2013) A3108–A3112. doi:10.1149/2.016305jes.

[77] F. Wu, H. Lu, Y. Su, N. Li, L. Bao, S. Chen, Preparation and electrochemical performance of Li-rich layered cathode material, Li[Ni0.2Li0.2Mn0.6]O2, for lithium-ion batteries, J. Appl. Electrochem. 40 (2010) 783–789. doi:10.1007/s10800-009-0057-2.

[78] K. Amine, H. Tukamoto, H. Yasuda, Y. Fujita, Preparation and electrochemical investigation of LiMn2 − xMexO4 (Me: Ni, Fe, and x = 0.5, 1) cathode materials for secondary lithium batteries, J. Power Sources. 68 (1997) 604–608. doi:10.1016/S0378-7753(96)02590-6.

[79] M.C. López, J.L. Tirado, C. Pérez Vicente, Structural and comparative electrochemical study of M(II) oxalates, M = Mn, Fe, Co, Ni, Cu, Zn, J. Power Sources. 227 (2013) 65–71. doi:10.1016/j.jpowsour.2012.08.100.

[80] J. Vázquez, P.L. López-Alemany, P. Villares, R. Jiménez-Garay, A theoretical study on the crystallized fraction and the kinetic parameters by continuous heating techniques. Application to the devitrification of the Sb0.16As0.36Se0.48 alloy, Mater. Lett. 35 (1998) 50–57. doi:10.1016/S0167-577X(97)00216-4.

[81] A. Huizing, H.A.M. van Hal, W. Kwestroo, C. Langereis, P.C. van Loosdregt, Hydrates of Manganese (II) Oxalate, Mater. Res. Bull. 12 (1977) 605–611.

[82] X. Zhang, F. Cheng, K. Zhang, Y. Liang, S. Yang, J. Liang, J. Chen, Facile polymer-assisted synthesis of LiNi0.5Mn1.5O4 with a hierarchical micro–nano structure and high rate capability, RSC Adv. 2 (2012) 5669. doi:10.1039/c2ra20669b.

[83] F. Cheng, Y. Xin, J. Chen, L. Lu, X. Zhang, H. Zhou, Monodisperse Li1.2Mn0.6Ni0.2O2 microspheres with enhanced lithium storage capability, J. Mater. Chem. A. 1 (2013) 5301. doi:10.1039/c3ta00153a.

[84] W. Luo, Effect of morphology on the physical and electrochemical properties of the high-voltage spinel cathode LiMn1.5Ni0.5O4, J. Alloys Compd. 636 (2015) 24–28. doi:10.1016/j.jallcom.2015.02.163.

[85] A.S. Moskvin, A.S. Ovchinnikov, The singlet-triplet magnetism and induced spin fluctuations in the high-Tc copper oxides, Phys. C Supercond. Its Appl. 296 (1998) 250–268. doi:10.1016/S0921-4534(97)01843-1.

[86] R. Zauner, A.G. Jones, Determination of nucleation, growth, agglomeration and disruption kinetics from experimental precipitation data: the calcium oxalate system, Chem. Eng. Sci. 55 (2000) 4219–4232. doi:10.1016/S0009-2509(00)00059-2.

[87] D. Milan, D. Peal, US patent US 2016/0093872 A1, 2013. doi:10.1016/j.(73).

[88] J. Ying, C. Wan, C. Jiang, Y. Li, Preparation and characterization of high-density spherical LiNi0.8Co0.2O2 cathode material for lithium secondary batteries, J. Power Sources. 99 (2001) 78–84.

[89] M.-H. Lee, Y.-J. Kang, S.-T. Myung, Y.-K. Sun, Synthetic optimization of Li[Ni1/3Co1/3Mn1/3]O2 via co-precipitation, Electrochim. Acta. 50 (2004) 939–948. doi:10.1016/j.electacta.2004.07.038.

[90] S. Park, H. Shin, S. Myung, C.S. Yoon, Synthesis of Nanostructured Li[Ni1/3Co1/3Mn1/3]O2 via a Modified Carbonate Process, Chem. Mater. 17 (2005) 6–8. doi:10.1021/cm048433e.

2: Compositional control of precipitate precursors for lithium-ion battery active materials: role of solution equilibrium and precipitation rate

2.1 Overview

Multicomponent transition metal oxides are among the most successful lithium-ion battery cathode materials, and many previous reports have described the sensitivity of final electrochemical performance of the active materials to the detailed composition and processing. Coprecipitation of a precursor template is a popular, scalable route to synthesize these transition metal oxide cathode materials because of the homogeneous mixing of the transition metals within the particles, and the morphology control provided by the precursors. However, the deviation of the precursor composition from feed conditions is a challenge that has generally not been reported in previous studies. Using a target final material of the high voltage spinel $LiMn_{1.5}Ni_{0.5}O_4$ as an example, we show in this study that the compositional deviation caused by coprecipitation can be significant under certain conditions, impacting the calcined final material structure and electrochemical properties. The study herein provides insights into the role of solution equilibrium and rate of precipitation of the transition metals during precipitate formation on precursor, and thus final active material, composition. Such knowledge is necessary to rationally predict and tune multicomponent battery precursor compositions synthesized via coprecipitation with high levels of accuracy.

The content of this chapter has been published in the following journal:

☐ Dong, H., & Koenig Jr, G. M. (2017). Compositional control of precipitate precursors for lithium-ion battery active materials: role of solution equilibrium and precipitation rate. Journal of Materials Chemistry A, 5(26), 13785-13798.

2.2 Introduction

Due to their high energy density, lithium-ion (Li-ion) batteries have become a popular choice for applications ranging in scale from consumer electronics to electric vehicles to stationary energy storage systems.[1] Especially with regards to cathode materials, Li-ion batteries do not have a single material structure or composition that dominates but have many different materials that may be suited to a particular performance or cost objective.[2,3,12–21,4,22–31,5,32–35,6–11] Many current and future commercial cathode materials are multicomponent transition metal (TM) oxides including $LiNi_{0.80}Co_{0.15}Al_{0.05}O_2$,[7,18–22], $LiNi_{1/3}Mn_{1/3}Co_{1/3}O_2$,[14–17] $LiNi_{0.5}Mn_{0.5}O_2$,[36–38] $LiMn_{1.5}Ni_{0.5}O_4$,[7,23,32–34,24–31] and $xLiMn_2O_3\cdot(1-x)LiNi_{1/3}Mn_{1/3}Co_{1/3}O_2$.[8,39–42] Such materials have been reported to have material structure and electrochemical performance that is highly sensitive to the stoichiometry of the final material.

Various routes have been reported in the literature to synthesize multicomponent metal oxide cathode materials, including direct solid-state conversion of individual precursors, [43–49] hydrothermal synthesis, [50–53] spray pyrolysis, [54–58] and various deposition techniques. [59–62] One method that is very popular in the literature is coprecipitation of precursors followed by calcination to final active materials. Coprecipitation has the advantages that it is relatively easy to perform in the lab, scalable, allows tunable and monodisperse particle morphologies, [19,63–70] and provides homogeneous mixing of the multiple TM components throughout the secondary particles. While coprecipitation has many advantages and there are many reports synthesizing high performance materials using this method, one common assumption of materials produced via coprecipitation is that the particles retain the stoichiometry of the feed solution. However, depending on solution conditions this may not be a reasonable assumption. Van Bommel *et al.* previously showed through equilibrium calculations that the fractions of Ni, Mn, and Co that remained as soluble species during hydroxide coprecipitation with a chelating agent were highly variable and pH dependent.[71] While these results suggest that predictive calculations should be done to adjust the feed stoichiometry to target the desired precipitate stoichiometry, the use of such analysis has rarely been reported. Many reports of multicomponent TM battery active materials that used coprecipitation of precursors for the final active material do not confirm the stoichiometry of the TMs in the precipitate. If calculations were performed, generally only solution equilibrium was considered; and the calculations were not used to guide decisions on precursor solution feed conditions. Also, no reports have considered whether the relative rate of coprecipitation varied for the different TMs. In this paper, a technique for determining the extent of coprecipitation of each TM independently in solution during synthesis will be described. Rates of coprecipitation from these measurements were used in combination with equilibrium calculations to achieve the goal of explicit composition control. We will demonstrate the impact of such control on material structural and electrochemical properties using an exemplar cathode material.

For this study, we have chosen the target cathode material LiMn1.5Ni0.5O4 (LMNO), and to produce the material an oxalate precursor ($Mn_{0.75}Ni_{0.25}C_2O_4 \cdot 2H_2O$) was synthesized via coprecipitation with a 3:1 target Mn:Ni ratio. LMNO has a high operating voltage of 4.7 V vs. Li, and the power and energy density advantages have made LMNO a good candidate as the cathode active material for transportation and energy storage [33,35,72–77]. The sensitivity of LMNO material properties to TM stoichiometry, [67,78] coupled with the material having only two TM cations to consider, made this material an ideal candidate for this initial study.

We have chosen oxalate coprecipitation chemistry for LMNO synthesis because in isolation both Mn and Ni form stable oxalate dihydrate precipitates in aqueous solutions exposed to air, and oxalates have been previously used as battery precursors. [65,66,69,70,79] Carbonate coprecipitation is another popular method to synthesize 3:1 Mn:Ni precursor; however, $NiCO_3$ is difficult to form as a stable precipitate.[80–86] Hydroxide coprecipitation is more complex because of the tendency of Mn to oxidize to MnOOH.[70,71,87–91] Moreover, oxalate ions in the solution play a dual role as both the precipitation reagent and a complexing agent.[92–94] The formation of metal complexes with oxalate ions as the ligand slows down the precipitation rate and thus the nucleation and particle growth process becomes more controllable. According to previous reports, oxalate coprecipitation can be used to synthesize precursor particles of narrow size distribution, and particle morphologies were successfully tuned by careful control over solution conditions.[64,95] Explicit control over particle morphology can be important for battery active materials due to the role that morphology plays in electrode packing, electrode microstructure, and active material transport limitations.[26,96–101] However, synthesis that incorporates morphology control of precursor is often performed at low feed reagent concentrations where equilibrium and rate of precipitation need to be carefully considered and predefined. For the particular Mn-Ni blend oxalate coprecipitation reaction, previous reports have even explicitly noted adjustment of TM feed ratios using an empirical approach to compensate for the composition deviation.[102]

Equilibrium calculations in this study will show that feed stoichiometry can deviate significantly from the precipitate stoichiometry, and thus resulting final material composition. In addition, we will demonstrate that rate of precipitation of TMs needs to be considered, though experimental evidence will suggest the formation of seeds of the faster forming precipitate likely mitigates the impact of different rates of precipitation under some solution conditions. The techniques in this report should be translatable to other precursor systems such as hydroxides and carbonates.

2.3 Experimental and Method

2.3.1 Preparation of Oxalate Precursor and Cathode Active Material Particles.

Laboratory grade $MnSO_4$ H_2O, $NiSO_4$ $6H_2O$, and $Na_2C_2O_4$ (all from Fisher) were used for the coprecipitation synthesis. TM sulfate and oxalate reagents were dissolved separately in deionized (DI) water to prepare TM solution and oxalate solution, and both solutions were heated to 60 °C. The TM solution was then poured all at once into the oxalate solution to start the coprecipitation reaction. The total volumes of the mixed solutions were 0.8 L (within a 1 L beaker) for all syntheses, and the reagent masses were adjusted to each desired solution concentration and TM feed ratio. The temperature was maintained during the reaction at 60 °C using a hot plate. The coprecipitation solution was stirred continuously at 300 rpm with a magnetic stirrer to keep the solution homogeneous during the precipitate formation and to prevent particles from settling within the suspension. The particles were collected by vacuum filtration after 30 minutes, and then rinsed with ~2 L DI water before drying in the oven (Carbolite) at 80 °C overnight. The precursor particles were mixed with 5% excess LiOH with 1:2 Li:TM ratio using a mortar and pestle by hand for 5 minutes. This mixture was then fired in the furnace (Carbolite CWF 1300 box furnace) in an air atmosphere at 850°C for 6 hours to obtain the final active material (with the target composition generally being $LiMn_{1.5}Ni_{0.5}O_4$). The furnace temperature ramp rate was set at

1°C / minute, and during the firing process the temperature was programmed for holds at 200 °C and 350 °C each for 2 hours to complete the individual steps of the structural water loss and oxalate decomposition, respectively.

2.3.2 Solution Equilibrium Calculations.

Equilibrium calculations were performed using OLI$^{\text{TM}}$ Studio 9.2. Calculations were also performed using an appropriate system of equations including solubility constants and complexation constants [103] combined with an appropriate numerical optimization package [71]. We noted that the equilibrium concentrations of the various solution species did not deviate significantly when using literature data and numerical optimization compared to commercial OLI$^{\text{TM}}$ calculations; however, the OLI$^{\text{TM}}$ values are the only ones reported in this study because they incorporated temperature influences, and this information was not readily available in the literature.

2.3.3 Rate of Precipitation of Ni and Mn.

Experiments were conducted to determine the concentration of each soluble TM remaining in the solution as a function of coprecipitation time. The reactor vessels were 1L beakers and solutions were prepared in the same manner as described above. At periodic time intervals during the coprecipitation, a sample (~2 mL) was withdrawn from the 1L beaker using a 3 mL syringe. For the withdrawn sample, the aqueous phase was quickly separated from the solid precipitate particles by forcing the solution through a 33 mm diameter syringe filter with 0.22 μm pore size (Fisherbrand). The aqueous phase was further digested using aqua regia and diluted with DI water into a proper concentration for inductively coupled plasma optical emission spectroscopy (ICP) analysis (PerkinElmer Optima 8000). The typical concentration range for ICP analysis was 0.1 to 100 ppm for Mn and Ni. Samples were continuously collected along the course of the reaction and the TM concentrations remaining in the aqueous phase were obtained as a function of reaction time. The total volume collected during the experiment for compositional analysis was typically 30 mL, or 3.5% of the total initial solution volume.

2.3.4 Material Characterization and Electrochemical Evaluation.

The chemical compositions of the precursors were measured using ICP analysis after the powders were digested with aqua regia and diluted to appropriate concentrations for analysis. The morphologies of the oxalate precursor and calcined final active materials were characterized with a scanning electron microscope (SEM, FEI Quanta 650). The crystal structure of the materials were analyzed by powder X-ray diffraction (XRD) with a PANalytical X'pert ProMPD using a Cu-Kα radiation source. Thermal gravimetrical analysis (TGA, TA Q50) was conducted to confirm the amount of the structural water and the weight loss profile of the oxalate precursors. All thermal measurements were performed in air at a heating rate of 10°C min-1. Electrochemical testing was performed using CR2032-type coin cells. The cathodes were fabricated by blending 80 wt% active material, 10 wt% acetylene black as the conductive additive, and 10 wt% polyvinylidene difluoride binder (dissolved in N-methyl-2-pyrrolidone as the solvent) first by hand with mortar and pestle and then in a slurry mixer (Thinky) for 6 minutes. The mixed electrode slurry was then pasted onto an aluminum foil current collector with an AFA-3 automatic film coater (MTI) and using a doctor blade with a gap thickness of 200 µm. The electrode was dried at 80 °C overnight in an oven in air, followed by another 3 hour vacuum drying at 80 °C prior to punching into 14 mm diameter electrode disks. The loading of active material in electrodes evaluated were all between 7.2 and

12.8 mg (4.5 and 8.0 mg cm-2). Coin cells were assembled inside an argon-filled glove box (<1 ppm O2 and H2O) with a single thin film of lithium metal as the counter and reference anode. Celgard 2325 trilayer membrane was used as the separator. The electrolyte was 1.2M LiPF6 dissolved in ethylene carbonate (EC) and ethyl methyl carbonate (EMC) (3:7 vol. %). The cells were tested in the voltage range of 3.6–4.9 V at room temperature using a MACCOR battery cycler. Where C rates are given, 1C was assumed to correspond to 14.7 mA/g LMNO active material.

2.4 Results and Discussion

2.4.1 Concentration Influence on Deviation between Actual and Feed Ratios.

At equilibrium, stoichiometry deviations of the solid precipitates relative to the stoichiometry ratio of the feed solutions is primarily a result of the solubility differences between the TMs. [64,104] As will be shown later, all TMs in this study precipitate as oxalate dihydrates. At room temperature the solubility of $NiC_2O_4 \cdot 2H_2O$ is 0.0018g/100g water, whereas $MnC_2O_4 \cdot 2H_2O$ solubility is significantly greater at 0.0309g/100g water.[64] This solubility difference between $MnC_2O_4 \cdot 2H_2O$ and $NiC_2O_4 \cdot 2H_2O$ leads to the prediction that during a coprecipitation of a blend of Mn and Ni using oxalate the precipitate would be relatively enriched in Ni.[102] The proportional deviation from stoichiometry of the precipitate would be expected to become more significant as the total solution concentration of the TMs and oxalate is decreased, because the solubility limit would have a greater relative impact at lower concentrations. Figure 1 displays the calculated Mn:Ni ratios in the precipitates at equilibrium as a function of total feed concentrations. Note that these are detailed calculations with many solution species at 60 °C, and not a result of only using the TM oxalate solubility values. Tabulated values are also listed in Table S1. In all cases the Mn:Ni feed solution ratio was 3:1 and the TM:oxalate ratio was 1:1, and if all of the TM were to precipitate as oxalate the 3:1 ratio would be retained. It is observed that the Mn:Ni ratio drops sharply away from the 3:1 feed ratio as the total feed concentration decreases below 50 mM. The calculated ratio is 1.7 at 10 mM, which is nearly a 50% deviation from the feed ratio. Figure 1 also contains the experimentally measured Mn:Ni ratios of the collected precursor powders determined by digesting the powders and using ICP analysis. All the precursors were collected 30 minutes after the TM and oxalate solutions were mixed together at 60 °C. In comparison to equilibrium calculations, all the measured ratios are higher and closer to the feed ratio; and the gap increases as the total feed concentration decreases. As will be discussed later, our experiments suggest that this gap reflects the differences in the rate of precipitation of the Mn relative to Ni. As the concentration increases, the difference between the measured values and the calculated values decreases because the solution moves closer to equilibrium conditions faster with the rate of precipitation increasing at higher initial solution concentrations.

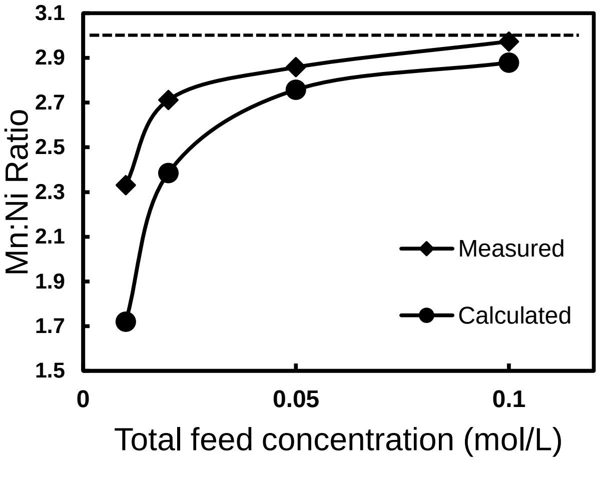

Figure 1. The measured (diamonds) and calculated at equilibrium (circles) Mn:Ni stoichiometric ratio in the precipitate as a function of total TM feed concentration. The feed ratio of Mn:Ni is 3:1

in all cases, and a dashed line is added at Mn:Ni = 3.0 for comparison. Lines between data points added to guide the eye.

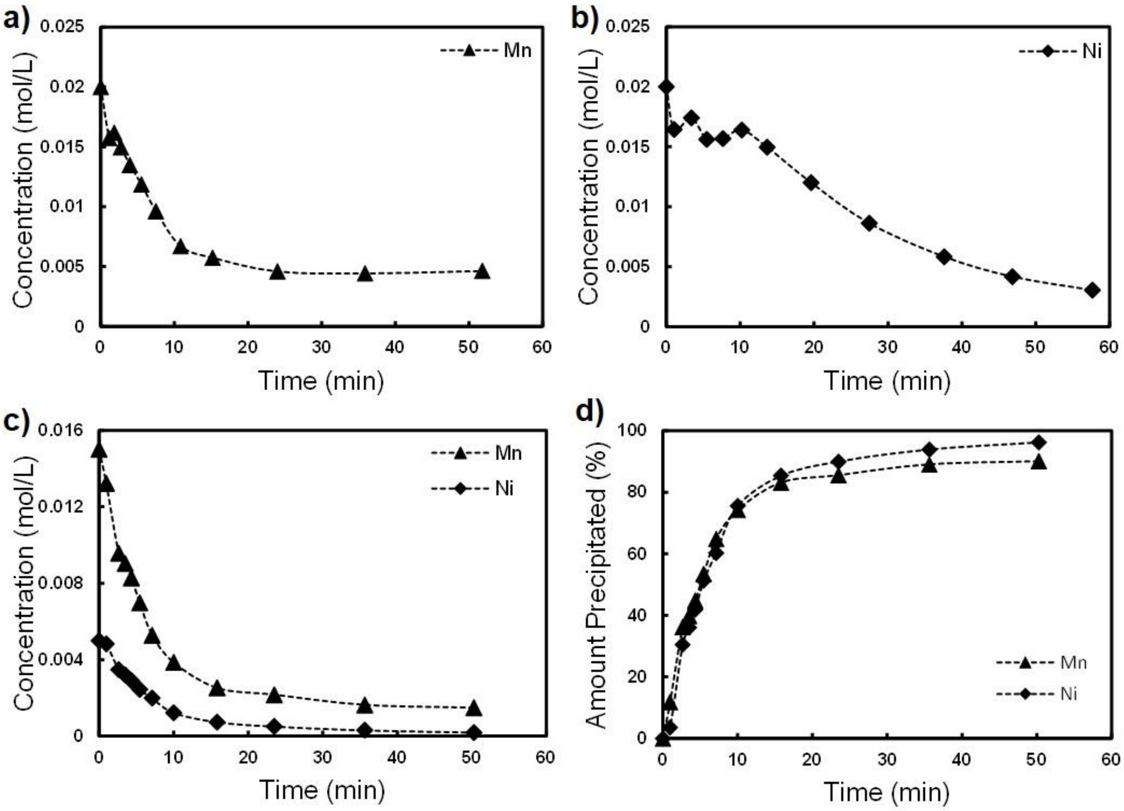

Figure 2. Residual soluble a) Mn and b) Ni in solution during coprecipitation of pure $MnC_2O_4{\cdot}2H_2O$ and $NiC_2O_4{\cdot}2H_2O$. c) Residual soluble Mn (triangles) and Ni (diamonds) during coprecipitation of feed with 3:1 Mn:Ni ratio. The total concentrations of TM and oxalate at the beginning of the coprecipitation for all solutions were 20 mM. d) Fraction of Mn and Ni ions in precipitate. Dashed lines added to guide the eye.

2.4.2 Precipitation Timescales for Pure and Blend systems.

The differences between equilibrium calculations and measured stoichiometries for the oxalate precipitates led to investigations of the concentration of the TM left in solution as a function of time. Before determining the concentration profile for the 3:1 Mn:Ni feed, first experiments were conducted with solutions containing only pure Mn or Ni at 20 mM. We chose to use 20 mM total TM (and oxalate) as the initial feed concentration for these experiments because 1) the concentration was low enough that it resulted in significant deviation between the equilibrium calculated and measured precipitate ratios (Figure 1), and 2) this concentration was high enough to provide adequate amounts of precipitate powder for lithiation and calcination to final battery active material as well as materials characterization. Figure 2a shows the concentration of soluble Mn as a function of time during coprecipitation of $MnC_2O_4\cdot 2H2O$. Figure 2b shows the results of the same experiment where the only difference was the substitution of Mn with Ni. The soluble Mn concentration decreased faster than Ni for the pure TM experiments, indicating that pure $MnC_2O_4\cdot 2H2O$ initially precipitated faster than pure $NiC_2O_4\cdot 2H_2O$. These results indicated that the manganese coprecipitation reaction had a lower activation barrier, resulting in $MnC_2O_4\cdot 2H2O$ crystalizing and precipitating faster than $NiC_2O_4\cdot 2H_2O$ at the early nucleation stages. As discussed earlier, initial coprecipitation experiments were 30 minutes. The concentration of residual TM in the pure Ni experiment has not plateaued in this time frame, indicating that 30 minutes was not a sufficient timescale to approach equilibrium. We also note that while the pure Mn concentration appears to have reached a plateau in less than 30 minutes, the residual concentration still exceeds equilibrium (0.0045 mol/L compared to 0.0036 mol/L). SEMs of the resulting $MnC_2O_4\cdot 2H_2O$ and $NiC_2O_4\cdot 2H_2O$ precipitates collected after 30 minutes can be found in the Appendix, Figure S1. The faster precipitating MnC2O4·2H2O particles were larger and had rougher surfaces than the $NiC_2O_4·2H_2O$ material.

Although $MnC_2O_4·2H_2O$ initially precipitated faster, after a sufficient time period (40 minutes), the soluble Ni concentration was significantly lower than the soluble Mn concentration. At long times, the precipitation of $NiC_2O_4·2H_2O$ was more complete, consistent with the solubilities of the two TM oxalates. Based on the extent of coprecipitation measured for the two pure TM oxalate systems, the precipitate collected from the blend precipitation after 30 minutes would be expected to be relatively enriched in Mn; however, the opposite Mn-lean precipitate was observed experimentally (Figure 1). These results indicated that there were additional considerations when Mn and Ni were coprecipitated from the same solution. Another interesting outcome from the experiments in Figures 2a-b is that if the TMs precipitate at different rates, the resulting precursor would not be expected to be homogenous with regards to TM distribution in the precursor, which is a commonly cited advantage of coprecipitation synthesis for battery precursor materials. The pure Mn and Ni coprecipitation data suggests a Mn-rich core and Ni-rich shell, or separately Mn-rich and then Ni-rich precipitate particles, would likely result. To gain further insights, we conducted the same residual concentration as a function of time analysis for both Mn and Ni during the coprecipitation of a 3:1 Mn:Ni feed.

Figure 2c displays the residual soluble Ni and Mn during precipitation of a feed 20 mM 3:1 Mn:Ni TM solution. Due to the difference in initial concentration of Ni and Mn, Figure 2d shows the extent of Ni and Mn precipitated as a function of time, which is more instructive for comparing the homogeneity of the coprecipitation. Interestingly, in this synthesis with the blended TM feed both species precipitate at a nearly 1:1 ratio throughout the synthesis, contrary to expectations based on the pure Mn and Ni precipitation experiments. This implies an interaction between the two TMs and/or the TMs and the oxalate precipitates were facilitating this process. The precipitation of Ni in the 3:1 blend feed solution proceeds much faster than for the pure Ni feed, even though the 3:1 blend has the same total TM and oxalate concentration and lower Ni concentration. The blend coprecipitation resulted in higher overall extent of precipitation for both species after 30 minutes. Quantitatively, 87% of manganese ion and 92% of nickel ion precipitated, compared to 77% and 60% in their pure oxalate precipitation reactions, respectively. The resulting precipitate was now Ni-rich, which was consistent with previous observations (Figure 1). These results led us to speculate that the faster-forming $MnC_2O_4 \cdot 2H_2O$ particles were providing seeds in the blend system to facilitate $NiC_2O_4 \cdot 2H2O$ coprecipitation. To provide support for this speculation, we then conducted seeding experiments by adding 0.34 g of pure $MnC_2O_4 \cdot 2H_2O$ seeds at the beginning of a coprecipitation of 20 mM pure Ni2+ with oxalate (identical conditions to Figure 2b except for seed addition). The mass of the seeds was chosen such that the amount of Mn atoms was 10% of the Ni atoms in the solution. Residual soluble nickel as a function of time during coprecipitation of pure Ni, pure Ni with $MnC_2O_4 \cdot 2H_2O$ seeds, and the Mn:Ni 3:1 system are shown in Figure 3a. Figure 3b is the fraction of Ni that has been precipitated as a function of time for the same experiments. It can be seen from Figure 3a that adding $MnC_2O_4 \cdot 2H_2O$ seeds facilitated faster coprecipitation of nickel. However, inspection of Figure 3b reveals that the coprecipitation of Ni in the seeded experiment was still slower than for the Mn:Ni 3:1 blend. We speculate that this difference was largely due to differences in surface area between the initial particles in the 3:1 blend synthesis and the $MnC_2O_4 \cdot 2H_2O$ particles in the seeded experiment. We expect that the initial precipitates that formed in the 3:1 blend synthesis were very small, though detailed characterization of their size was challenging and is a focus of current investigations in our lab. In contrast, the seed particles were from pure $MnC_2O_4 \cdot 2H_2O$ synthesis experiments and these particles were quite large, with an average size of ~20 um that was consistent with previous reports.[39,68,105] A SEM image of the seeds can be found in the Appendix, Figure S1. The smaller particles that form in-situ during synthesis in the 3:1 blend system provide more surface for the coprecipitation, speeding up the loss of residual Ni in the solution to the precipitate phase relative to the lower surface area seeded experiments. In summary, the seeded precipitation experiments provided evidence that the $MnC_2O_4 \cdot 2H_2O$ in the 3:1 blend facilitates faster initial precipitate formation, which speeds up the precipitation of $NiC_2O_4 \cdot 2H_2O$. These results indicated that at least in some cases TMs with very different precipitation rates can precipitate almost at the same rate in blends because seeds of faster forming precipitates will facilitate increasing the precipitation rate of the slower precipitation compounds. Further investigation is needed to determine how general this observation is with regards to concentration regimes, TM species, and coprecipitation anions; however, it provides evidence that coprecipitation does indeed provide homogeneous TM precipitates – even if the rates of precipitation are quite different.

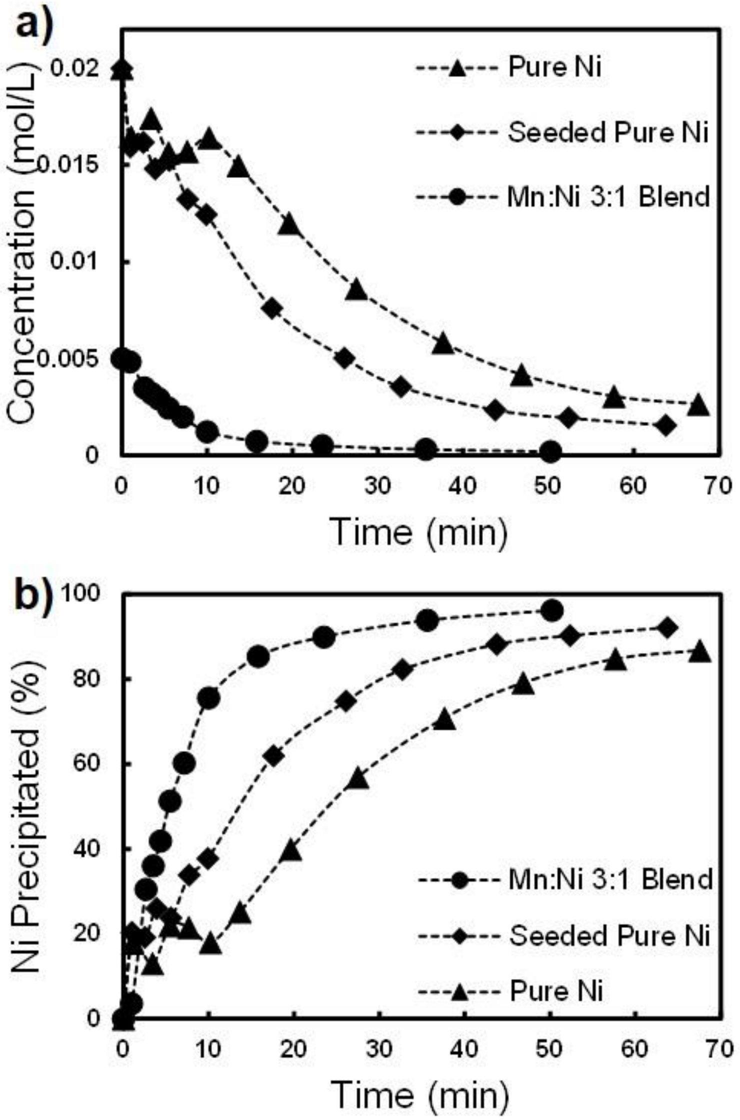

Figure 3. a) Measured soluble Ni as a function of time during coprecipitation of 20 mM oxalate with 20 mM Ni (triangles), 20 mM Ni with $MnC_2O_4 \cdot 2H_2O$ seeds(diamonds), and 20 mM 3:1 Mn:Ni (circles). b) The fraction of Ni lost to the precipitate phase using the data in a). Dashed lines added to guide the eye.

2.4.3 Oxalates Structural and Thermal Characterization.

According to previous reports, both Mn and Ni oxalates may exist in an α-phase dihydrate oxalate[94,106] whose prototype is the mineral Humbodtine α-$FeC_2O_4 \cdot 2H_2O$ with monoclinic space group C2/c.[92] Nickel oxalate dihydrates have also been reported to crystallize in the orthorhombic system in space group Cccm,[94,106] whose X-ray peaks are indexed with β-$FeC_2O_4 \cdot 2H_2O$.[92] Mn oxalate, unlike the other d-block TM oxalates, does not present an orthorhombic β-MIIC2O4·2H2O (where M stands for the d-block TM) modification.[94,106] It has another dihydrate, however, denominated as γ-$MnC_2O_4 \cdot 2H_2O$ which is also orthorhombic while belonging to space group P212121 and is found to crystallize under high pH conditions. [68]

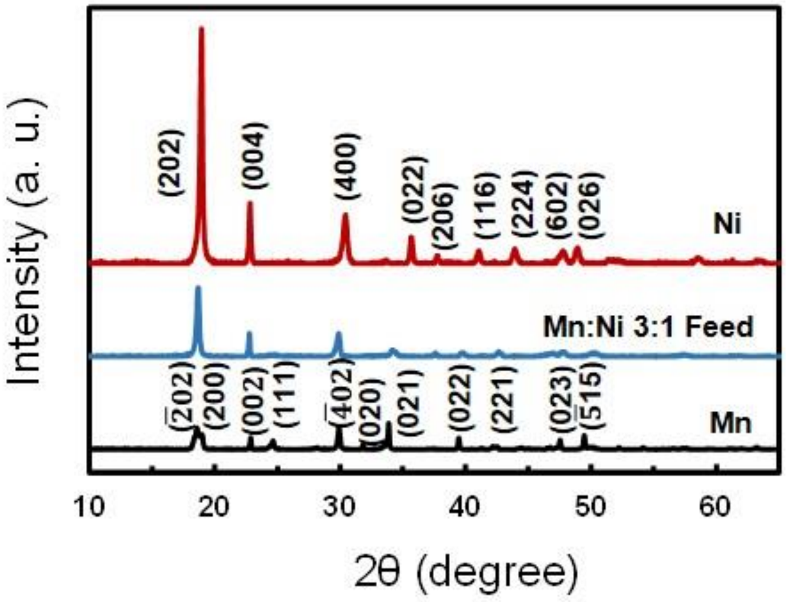

Figure 4. XRD patterns of NiC2O4·2H2O (red), Mn:Ni 3:1 feed oxalate dihydrate (blue), and $MnC_2O_4 \cdot 2H_2O$ (black). Miller indices correspond to orthorhombic and monoclinic symmetries for $NiC_2O_4 \cdot 2H_2O$ and $MnC_2O_4 \cdot 2H_2O$, respectively.

XRD patterns of the pure and blend TM oxalate powders were analysed to determine the resulting structures (Figure 4). The pure Mn oxalate was indexed with the α-$FeC_2O_4·2H_2O$ monoclinic phase and the pure Ni oxalate was indexed with the β-$FeC_2O_4·2H_2O$ orthorhombic phase.[92] The XRD pattern of the blend 3:1 feed TM oxalate (note: ICP composition was 2.6:1 Mn:Ni) powder was identical to the pattern of Ni oxalate powder, consistent with the β-oxalate, rather than a co-existence of the two oxalate polymorphs. The peaks in the blend oxalate, however, are less sharp and intense compared to the pure Ni oxalate dihydrate, which indicates some non-ideal mixing of the cations in the lattice structure and/or smaller crystallite sizes.[92] The peaks of the blend powder were also shifted to lower 2θ values compared to the peaks of pure Ni oxalate powder, which indicated expansion of the crystal lattice.[107] The lattice parameters calculated for the blend oxalate dihydrate were a=11.99 Å, b=5.53 Å, and c=15.62 Å, compared with those of NiC2O4·2H2O being a=11.75 Å, b=5.28 Å, and c=15.52 Å.[108] The shift in the lattice parameters with the addition of Mn to the precipitation solution indicated incorporation of larger size Mn ions (Mn2+ = 0.81 Å, Ni2+ = 0.69 Å) into the crystal, consistent with homogeneous precipitation of the TM oxalates and not independent precipitation of individual $MnC_2O_4·2H_2O$ and $NiC_2O_4·2H_2O$ particles.

Previous studies have also shown Mn-Ni forms a solid solution when precipitated with oxalate. [102,107,109] Unexpectedly, even though the blend system has 75% Mn and $MnC_2O_4·2H_2O$ precipitates faster than $NiC_2O_4·2H_2O$, the resulting phase was consistent with the β-$NiC_2O_4·2H_2O$ instead of α-$MnC_2O_4·2H_2O$. Thus, the β-$NiC_2O_4·2H_2O$ phase was favorable at these solution conditions. Whether the blend oxalate is α- or β-oxalate is dependent on the synthesis conditions. [92] We are currently exploring the detailed phase diagram for these oxalate materials and this topic will be the subject of a future publication; however, it appears that under the majority of solution compositions in the Mn-Ni blend system, adjusting only the Mn:Ni ratio, the β-$NiC_2O_4 \cdot 2H_2O$ was the preferred structure. The extent of Mn precipitation was greater in the blend system compared to pure $MnC_2O_4 \cdot 2H_2O$ (Figure 2). This observation also suggested that the β-$NiC_2O_4 \cdot 2H_2O$ structure facilitated a greater extent of Mn precipitation relative to the α phase crystal structure that forms in the pure Mn precipitation.

TGA analyses were conducted on the three oxalate samples. The dehydration step, which occurs below 200 °C, caused a mass loss of ~20% for all samples, which indicated the oxalate precursors synthesized were dihydrates (Mn and Ni composition of Mn0.72Ni0.28C2O4·2H2O for the blend precursors from ICP, feed was 3:1 Mn:Ni). Both the dehydration temperature and the oxalate decomposition temperature are greater for $NiC_2O_4 \cdot 2H_2O$ than for $MnC_2O_4 \cdot 2H_2O$, indicating that the thermal stability of $NiC_2O_4 \cdot 2H_2O$ was greater. In the case of $Mn_{0.72}Ni_{0.28}C_2O_4 \cdot 2H_2O$, the dehydration and oxalate decomposition peaks were between the values for $NiC_2O_4 \cdot 2H_2O$ and $MnC_2O_4 \cdot 2H_2O$. The relatively broad and high temperature for the dehydration peak, however, suggested the structural water was in an environment more similar to that of $NiC_2O_4.2H_2O$. This observation was consistent with the XRD patterns indicating that the blend oxalate structure was consistent with $NiC_2O_4 \cdot 2H_2O$. TGA profiles and full discussions can be found in the Appendix, Figure S2.

2.4.4 Synthesis of Slight Variations of Mn:Ni Ratio Stoichiometry Materials.

As discussed above, solution equilibrium calculations provide insights into selecting feed stoichiometry, but these calculations alone were not quantitative enough to use for predictive synthesis, particularly at low solution concentrations desirable for tuneable particle morphologies. Quantitative predictive models incorporating the precipitation rate will be a long-term goal;

however, further study and information on particle size distribution as a function of time will be needed to appropriately normalize the precipitation rate. To further demonstrate the importance of working towards these predictive synthesis methods, two additional blend oxalate precipitates were synthesized such that three resulting precursors were made: one that was almost exactly at the desired 3:1 Mn:Ni stoichiometry, one that was enriched in Ni (<3:1), and one that was enriched in Mn (>3:1). All oxalates were synthesized using 20 mM total TM and the particles were collected after 30 minutes to be consistent with earlier procedures. The 3:1 Mn:Ni feed from the earlier experiments resulted in 2.6:1 Mn:Ni, confirmed using ICP on digested powders, and this served as the Ni-rich sample. A feed ratio of 3.52:1 resulted in 3.02:1 Mn:Ni (the stoichiometric sample), and 3.82:1 feed resulted in 3.33:1 Mn:Ni (Mn-rich sample). The compositional deviation between equilibrium calculations and measurements varied from ~5-15%. After calcination of the oxalate samples in the presence of lithium, the detailed compositions of the three "LMNO" materials were $LiMn_{1.46}Ni_{0.54}O_4$, $LiMn_{1.5}Ni_{0.5}O_4$, and $LiMn_{1.54}Ni_{0.46}O_4$ which will be referred to as Ni-rich, stoichiometric, and Mn-rich LMNO, respectively. These listed compositions have Mn:Ni ratios consistent with ICP measurements on the final active material and assume a Li:TM ratio of 1:2 and TM:O ratio of 1:2. Actual Li:TM ratios and a summary of compositional information determined by ICP can be found in the Appendix, Table S2.

2.4.5 Characterization of the Stoichiometric and Non-stoichiometric LMNO Materials.

The three LMNO samples were synthesized to demonstrate that small compositional variations during coprecipitation synthesis, when not accounting for the deviation from feed stoichiometry, can result in detectable changes to the final active material after calcination. LMNO is cubic with Li on the tetrahedral sites of the structure. Depending on the distribution of Mn and

Ni ions in the lattice, LMNO has two different crystallographic structures: with disordered Ni and Mn on the octahedral sites the cubic spinel has the space group Fd-3m, while with higher ordering of Ni2+ and Mn4+ it has the space group P4332. In synthesizing spinel LMNO the high calcination temperature leads to the reduction of manganese from Mn4+ to Mn3+, which results in the Fd-3m disordered structure.[110] Annealing at 700□C for extended periods has been reported to reoxidize the Mn3+ back to Mn4+ and may convert the spinel to the primitive cubic ordered structure.[34,111]

Achieving the appropriate chemical composition is essential for extracting the maximum capacity from LMNO materials. For the molecular ratio of Mn:Ni 3:1, theoretically all the electrochemical capacity comes from the Ni2+/Ni4+ redox couple. When there is Mn:Ni deviation from 3:1; however, either Mn-rich or Ni-rich materials may result in changes to the oxidation state and/or the crystal phase, thus influencing the electrochemical performance. Since Ni in LiNi0.5Mn1.5O4 is Ni2+, we assume that nickel ions in the whole series of Mn-rich LiNixMn2-xO4 materials with 0<x<0.5 are also Ni2+. $\mathrm{LiNi_{x}^{2+}Mn_{1\text{-}2x}^{3+}Mn_{1+x}^{4+}O_4}$. Assuming that the 4.7 V high voltage capacity comes from the Ni redox, and that Mn^{3+}/Mn^{4+} redox gives a ~4.1 V plateau during cycling, we expect to get 2x Li capacity per formula unit at ~4.7V and (1-2x) Li capacity at ~4.1V, which have been observed experimentally.[6,72,79,112–114] Within the Mn-rich range, the material should be stable in the spinel phase, LiMn2O4 being the extreme case, though more Mn content results in a higher fraction of Mn3+ ions which potentially results in Jahn-Teller distortion, being detrimental to the structural stability. For Ni-rich materials (0.5<x<1), we assume the Mn4+ will not be further oxidized, and thus the oxidation state of Ni ions will be increased from Ni2+ to Ni3+ to meet charge neutrality and the result would be $\mathrm{LiNi_{1\text{-}x}^{2+}Ni_{2x\text{-}1}^{3+}Mn_{2\text{-}x}^{4+}O_4}$. Summing up the Ni^{2+}/Ni^{4+} and the Ni^{3+}/Ni^{4+} couples, the high voltage capacity would be constant through the compositional range, $LiNi^{3+}Mn^{4+}O_4$ being the extreme case. Based on the analysis above, if the compositional deviation was Ni-rich, a reduction in the high voltage electrochemical capacity would not be expected. However, as the Ni content increases, the risk of forming a rock-salt impurity phase significantly increases, which potentially deteriorates both the electronic conductivity, ionic conductivity, and total active material and thus energy density. The end point material, $LiNi^{3+}Mn^{4+}O_4$ was previously reported to have a rock-salt structure, showing XRD patterns consistent with $LiNiO_2$.[72,74,110] This means that there are likely multiple phases coexisting across some range of compositions in the Ni-rich regime. The formation of layered structures also presents the risk of phase segregation in the material, because Li-Mn-O has limited stability as a layered structure.[6,72,79,112,113] SEM images of the three precursors and their corresponding final oxide samples can be found in the Appendix, Figure S3. All the precursors exhibit hexagonal platelet secondary particle morphologies and similar secondary particle sizes of about 20 µm. The secondary particles were comprised of multi-faceted primary particles with length scales of approximately a couple hundred nanometers. The overall morphologies of the LMNO samples exhibit no significant differences and were not expected to contribute significantly to any observed differences in electrochemical cell performance.

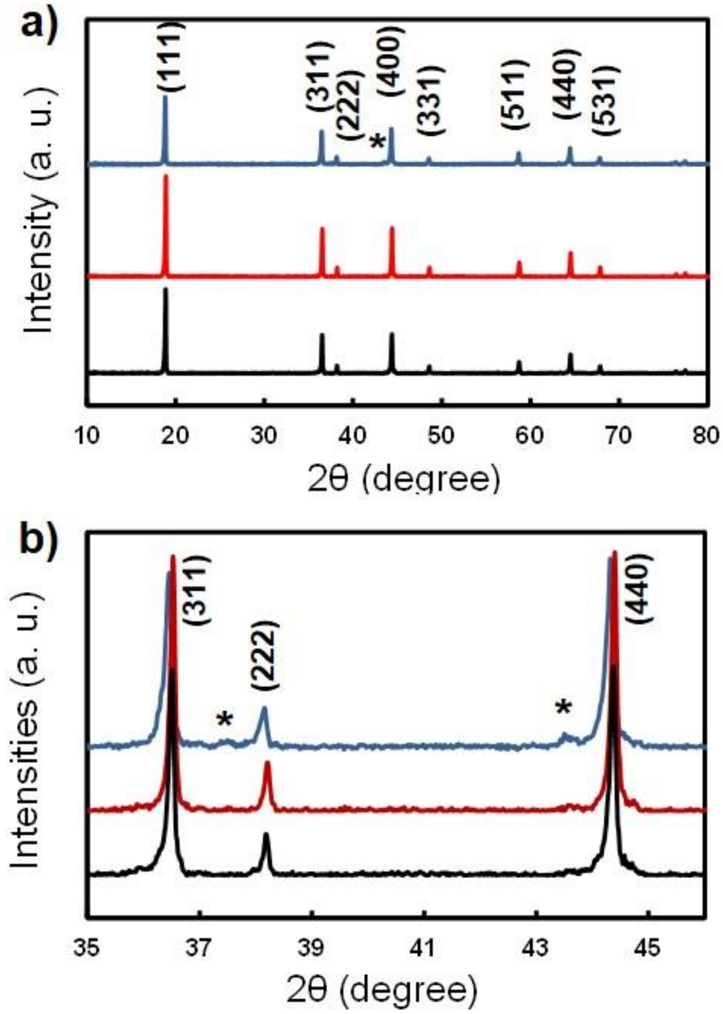

Figure 5. a) XRD patterns of Ni-rich (blue), stoichiometric (red), and Mn-rich (black) LMNO. b) Close up of patterns in a) between 35-46 degrees to better highlight the rock-salt impurity phase peaks (marked with *).

XRD patterns for Ni-rich, stoichiometric, and Mn-rich LMNO powders are shown in Figure 5. The peaks, except those marked with an *, all can be indexed to Fd-3m spinel cubic structures. The Ni-rich sample contains impurity peaks, and their location was consistent with previous reports of $Li_xNi_{1-x}O_2$ structures. [72,74,110] This implies that the higher fraction of nickel cannot be accommodated in the LMNO structure and thus the Ni enrichment facilitates the formation of the rock-salt impurity. The impurity phase was not observed in the Mn-rich LMNO sample.

Rietveld refinements were done using only the Fd-3m space group and the resulting lattice parameters of the three LMNO samples were 8.2046 Å, 8.1909 Å, and 8.1934 Å for Ni-rich, stoichiometric, and Mn-rich samples, respectively. The larger lattice parameter for the Ni-rich LMNO sample was attributed to the higher Ni ion content, since the ionic radius of Ni3+ (0.70 Å) is larger than the average of Mn4+ (0.53 Å) and Ni2+ (0.69 Å) [30]. Though some of the Ni distributes into the impurity phase, the high Ni content likely helps to ensure high Ni within the LMNO structure as well. The slightly higher lattice parameter of the Mn-rich LMNO sample relative to the stoichiometric sample may have been due to the relatively increased amount of Mn3+ (0.645 Å), whose ionic radius is greater than the average of Mn4+ (0.53 Å) and Ni2+ (0.69 Å). Relative peak intensities reflect the relative exposure degree of surface orientations in the spinel structure. [72,115,116] By normalizing to the (311) peak of the three patterns, the relative intensities were compared of the high-active (111) crystal facet, which were 2.066, 2.100, and 2.186 for Ni-rich, stoichiometric, and Mn-rich LMNO samples respectively. The similar values implied that the exposure degrees of the high-active (111) facet was not expected to contribute to differences in electrochemical measurements.

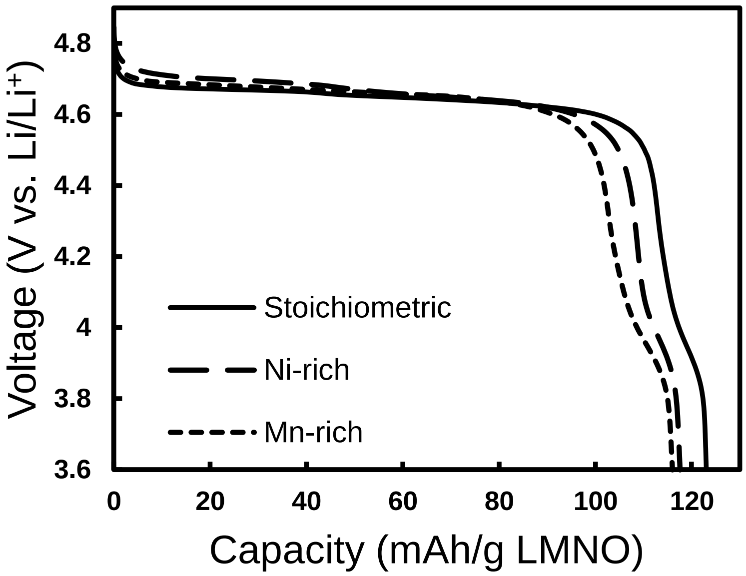

Figure 6. Discharge profiles of stoichiometric, Ni-rich, and Mn-rich Li/LMNO cells cycled at a rate of C/10 (147 mA/g LMNO).

The discharge curves of Li/LMNO coin cells, all charged/discharged at a rate of C/10, are shown in Figure 6. The stoichiometric LMNO had the highest first cycle discharge capacity of 123 mAh/g, while the Mn-rich and Ni-rich LMNO show similar capacities of around 115 mAh/g. The discharge capacity was divided into the high (4.9 to 4.1 V, vs. Li/Li+) and low (4.1 to 3.6 V, vs. Li/Li+) voltage ranges for comparison, corresponding to primarily Ni2+/Ni4+ and Mn3+/Mn4+ redox couples, respectively. Table 1 lists the electrochemical capacities of the three LMNO materials within these potential ranges, and also the calculated Mn3+ and Ni2+amounts based on these capacities. All the discharge capacities in Table 1 were averages of results from three different cells for each representative LMNO sample. The low voltage capacities of the Ni-rich LMNO and stoichiometric LMNO were nearly identical, and thus so were the calculated amounts of Mn3+. The Mn3+ formation occurs to some extent during the high temperature calcination procedure, regardless of the composition of the samples. The Mn-rich LMNO, however, had a greater Mn-rich LMNO, however, had a greater capacity within the low voltage range, which was attributed to higher amounts of Mn3+ in the structure. The higher fraction of Mn3+ observed was also consistent with the larger lattice parameters and expected composition of $LiNi_{0.46}^{2+}Mn_{0.08}^{3+}Mn_{1.46}^{4+}O_4$ with 0.08 mol Mn^{3+} per formula, which was close to 0.09 mol Mn3+ per mole of LMNO calculated based on the low voltage range capacity. In comparing Mn-rich LMNO and stoichiometric LMNO, the amount of Ni2+ in the materials was calculated by assuming that all the high voltage capacity came from the Ni2+/Ni3+/Ni4+ redox couple(s) (Table 1). Even in the stoichiometric sample, the Ni redox couple cannot be fully exploited during charge or discharge, possibly due to ion diffusion or electron exchange limitations.[25,63,117] The Ni^{2+} amount calculated from the electrochemical capacities of the Mn-rich material contains 94% the Ni^{2+} of the stoichiometric sample, close to the theoretical Ni2+ percentage of 92% obtained by comparing $LiNi_{0.46}^{2+}Mn_{0.08}^{3+}Mn_{1.46}^{4+}O_4$ to $LiNi_{0.5}Mn_{1.5}O_4$. This implies that the intrinsic capacity losses relative to the theoretical capacity appears to be proportionally lost by Ni^{2+} in the materials. Therefore, the detailed chemical composition of LMNO samples provides insights into the expected relative capacities in the low voltage and high voltage regions of the material, in particular when comparing Mn-rich and stoichiometric LMNO materials. This analysis was consistent with previous reports in the literature and was consistent with analysis of the dQ/dV plots of the electrode materials (see Figure S4 in the Appendix for the dQ/dV plots and further discussion).[78,110,114] Detailed comparison between Ni-rich and stoichiometric LMNO was not quite as straightforward because the impurity phase in the Ni-rich sample complicates the analysis. The quantity of the impurity phase for the Ni-rich LMNO appears to have been insufficient to significantly reduce the material capacity, though capacity decreases caused by more substantial proportions of the rock-salt impurity for Ni-rich LMNO samples have been previously established in the literature.[72] Similar levels of exposure of the high-active facet, as aforementioned, and similar Mn3+ in the stoichiometric and Ni-rich materials (Table 1) likely made identification of the electrochemical performance differences due to the compositional variation more difficult to observe.

Table 1. Summaries of the Ni-rich, stoichiometric, and Mn-rich LMNO discharge capacities. Standard deviations for capacity values were based on 5 discharge cycles of 3 cells for each material.

Sample	Mn:Ni (ICP)	Specific Capacity (mAh/g)			TM Ion Amount per Mole of LMNO based on Capacities	
		Total	Low Voltage	High Voltage	Mn^{3+} (mol)	Ni^{2+} (mol)*
Nickel-Rich	1.46 : 0.54	118.6±5.0	9.9±1.3	108.7±3.7	0.07	0.37
Stoichiometric	1.50 : 0.50	121.8±2.4	9.5±1.0	112.3±3.0	0.06	0.38
Manganese-Rich	1.54 : 0.46	118.2±1.9	12.6±1.0	105.5±1.0	0.09	0.36

*The Ni^{2+} amount was calculated assuming all the high voltage capacity was from Ni^{2+}/Ni^{4+} redox couple.

Cycle life testing of Li/LMNO coin cells was also conducted and the results can be found in Appendix Figure S5. All cells had similar capacity fade after 200 charge/discharge cycles at C/10. The specific discharge capacities after 200 cycles were 112.9 mAh/g, 115.9 mAh/g, and 107.1 mAh/g with capacity retentions of 95.2%, 97.4%, and 91.9% (relative to the 10th cycle) for the stoichiometric, Ni-rich, and Mn-rich LMNO materials, respectively. All cells appeared to have an activation-related capacity increase for the first several cycles, thus the 10th cycle was chosen for relative capacity retention.[63,73,118,119] While the stoichiometric LMNO had encouraging results both with regards to total capacity and capacity retention, the relatively small differences between the three materials makes it premature to assign achieving the stoichiometric composition as improving these two metrics without more extensive cell testing and analysis. Interestingly, the first cycle coulombic efficiency (CE) was significantly different for the three materials, where the values were 90.8%, 85.9%, and 88.7% for stoichiometric, Ni-rich, and Mn-rich LMNO, respectively. The CE of the first few cycles is an indicator of the stability of the electrode-electrolyte interface and high CE indicates a stable interface.[72] The high CE of the stoichiometric LMNO suggested it formed a relatively stable electrode-electrolyte interface, though more detailed investigations would be needed to confirm the stoichiometry at the interface of these materials with differing bulk compositions and the potential impact on the resulting solid-electrolyte interphase.

2.5. Conclusion

Coprecipitation is a popular route to synthesize Li-ion battery precursors, and performing coprecipitation in low solution concentration regimes can enable explicit tuning of morphology of battery precursor materials. A study was conducted to determine how significant the deviation in composition of multicomponent TM precursors may be from feed stoichiometries in a low concentration condition, using a model system containing Mn2+, Ni2+, and C2O42- as coprecipitation species. Equilibrium calculations suggest deviation between feed and resulting precursor stoichiometry, which had qualitative but not quantitative agreement. Experiments tracking the extent of precipitation of each of the TM species suggests that while TMs have very different rates in isolation, the faster precipitating species results in seed particles that result in nearly 1:1 precipitation of Ni and Mn when precipitated from the same solution. Synthesis of precursor particles that were produced using 3:1 Mn:Ni feed (Ni-enriched precipitate), 3:1 Mn:Ni precipitate, and an intentionally Mn-enriched precipitate demonstrated that even small deviations in relative Mn:Ni stoichiometry can have detectable impacts on material structure and electrochemical properties – though for these relatively small compositional deviations the material properties were not extreme. These results suggested that careful consideration of solution chemistry, including equilibrium distribution of TM and the rate at which different TM are precipitated, should be given more careful consideration during the synthesis of battery materials using coprecipitation methods. While in this study low concentrations of TM were used which was more relevant to morphology tuning of active materials important for investigating morphology effects on electrochemical properties, these results are also extendable to some effects observed with more concentrated solutions. In particular, the incorporation of chelating agents commonly used in larger scale coprecipitation will intensify compositional deviations between feed stoichiometry and particle stoichiometry even at relatively high TM concentrations. This topic will be toughed in the last chapter.

2.6. Reference

[1] M. Armand, J.-M. Tarascon, Building better batteries, Nature. 451 (2008) 652–657. http://dx.doi.org/10.1038/451652a.

[2] E. Lee, K.-W. Nam, E. Hu, A. Manthiram, Influence of Cation Ordering and Lattice Distortion on the Charge-Discharge Behavior of LiMn1.5Ni0.5O4 Spinel between 5.0 and 2.0V, Chem. Mater. 24 (2012) 3610–3620. doi:10.1039/c2ta01171a.

[3] M. Casas-Cabanas, C. Kim, J. Rodriguez-Carvajal, J. Cabana, Atomic scale drivers of ordering transitions in LiNi0.5Mn1.5O4 and relationship with electrochemical properties, J. Mater. Chem. A. (2016) 8255–8262. doi:10.1039/C6TA00424E.

[4] T. Kozawa, T. Murakami, M. Naito, Insertion of lattice strains into ordered LiNi0.5Mn1.5O4 spinel by mechanical stress: A comparison of perfect versus imperfect structures as a cathode for Li-ion batteries, J. Power Sources. 320 (2016) 120–126. doi:10.1016/j.jpowsour.2016.04.086.

[5] K. Saravanan, A. Jarry, R. Kostecki, G. Chen, A study of room-temperature LixMn1.5Ni0.5O4 solid solutions., Sci. Rep. 5 (2015) 8027. doi:10.1038/srep08027.

[6] H. Duncan, B. Hai, M. Leskes, C.P. Grey, G. Chen, Relationships between Mn 3+ Content, Structural Ordering, Phase Transformation, and Kinetic Properties in LiNi x Mn 2– x O 4 Cathode Materials, Chem. Mater. 26 (2014) 5374–5382. doi:10.1021/cm502607v.

[7] S. Patoux, L. Daniel, C. Bourbon, H. Lignier, C. Pagano, F. Le Cras, S. Jouanneau, S. Martinet, High voltage spinel oxides for Li-ion batteries: From the material research to the application, J. Power Sources. 189 (2009) 344–352. doi:10.1016/j.jpowsour.2008.08.043.

[8] M.M. Thackeray, C.S. Johnson, J.T. Vaughey, N. Li, S.A. Hackney, Advances in manganese-oxide “composite” electrodes for lithium-ion batteries, J. Mater. Chem. 15 (2005) 2257–2267. doi:10.1039/B417616M.

[9] S.-H. Kang, P. Kempgens, S. Greenbaum, A.J. Kropf, K. Amine, M.M. Thackeray, Interpreting the structural and electrochemical complexity of 0.5Li2MnO3-0.5LiMO2 electrodes for lithium batteries(M = Mn0.5−xNi0.5−xCo2x, 0 ≤x≤ 0.5), J. Mater. Chem. 17 (2007) 2069–2077. doi:10.1039/B618715C.

[10] S.-H. Kang, C.S. Johnson, J.T. Vaughey, K. Amine, M.M. Thackeray, The Effects of Acid Treatment on the Electrochemical Properties of 0.5 Li2MnO3 · 0.5 LiNi0.44Co0.25Mn0.31O2 Electrodes in Lithium Cells, J. Electrochem. Soc. . 153 (2006) A1186–A1192. doi:10.1149/1.2194764.

[11] J.-S. Kim, C.S. Johnson, M.M. Thackeray, Layered xLiMO2·(1−x)Li2M′O3 electrodes for lithium batteries: a study of 0.95LiMn0.5Ni0.5O2·0.05Li2TiO3, 2002. doi:10.1016/S1388-2481(02)00251-5.

[12] D. Kim, S.-H.H. Kang, M. Balasubramanian, C.S. Johnson, High-energy and high-power Li-rich nickel manganese oxide electrode materials, Electrochem. Commun. 12 (2010) 1618–1621. doi:10.1016/j.elecom.2010.09.009.

[13] J. Zheng, M. Gu, J. Xiao, B.J. Polzin, P. Yan, X. Chen, C. Wang, J.-G. Zhang, Functioning Mechanism of AlF3 Coating on the Li- and Mn-Rich Cathode Materials, Chem. Mater. 26 (2014) 6320–6327. doi:10.1021/cm502071h.

[14] S. Hwang, S.M. Kim, S.-M. Bak, S.Y. Kim, B.-W. Cho, K.Y. Chung, J.Y. Lee, E.A. Stach, W. Chang, Using Real-Time Electron Microscopy To Explore the Effects of Transition-Metal

Composition on the Local Thermal Stability in Charged LixNiyMnzCo1–y–zO2 Cathode Materials, Chem. Mater. 27 (2015) 3927–3935. doi:10.1021/acs.chemmater.5b00709.

[15] F. Yang, Y. Liu, S.K. Martha, Z. Wu, J.C. Andrews, G.E. Ice, P. Pianetta, J. Nanda, Nanoscale Morphological and Chemical Changes of High Voltage Lithium–Manganese Rich NMC Composite Cathodes with Cycling, Nano Lett. 14 (2014) 4334–4341. doi:10.1021/nl502090z.

[16] J. Li, R. Klöpsch, M.C. Stan, S. Nowak, M. Kunze, M. Winter, S. Passerini, Synthesis and electrochemical performance of the high voltage cathode material Li[Li0.2Mn0.56Ni0.16Co0.08]O2 with improved rate capability, J. Power Sources. 196 (2011) 4821–4825. doi:10.1016/j.jpowsour.2011.01.006.

[17] D. Mohanty, S. Kalnaus, R.A. Meisner, K.J. Rhodes, J. Li, E.A. Payzant, D.L. Wood, C. Daniel, Structural transformation of a lithium-rich Li1.2Co0.1Mn0.55Ni0.15O2 cathode during high voltage cycling resolved by in situ X-ray diffraction, J. Power Sources. 229 (2013) 239–248. doi:10.1016/j.jpowsour.2012.11.144.

[18] I. Lee, J. Kim, S. Han, J.-I. Park, J.-M. Lee, D.-H. Kim, S.-C. Nam, S. Yoon, Communication—Preparation of Highly Monodisperse Ni-Rich Cathode Material for Lithium Ion Batteries, J. Electrochem. Soc. . 163 (2016) A1336–A1339. doi:10.1149/2.1021607jes.

[19] R. Robert, C. Bünzli, E.J. Berg, P. Novák, Activation Mechanism of LiNi0.80Co0.15Al0.05O2: Surface and Bulk Operando Electrochemical, Differential Electrochemical Mass Spectrometry, and X-ray Diffraction Analyses, Chem. Mater. 27 (2015) 526–536. doi:10.1021/cm503833b.

[20] N. Wu, H. Wu, H. Liu, Y. Zhang, Solvothermal coating LiNi0.8Co0.15Al0.05O2 microspheres with nanoscale Li2TiO3 shell for long lifespan Li-ion battery cathode materials, J. Alloys Compd. 665 (2016) 48–56. doi:10.1016/j.jallcom.2016.01.044.

[21] S. Hwang, W. Chang, S.M. Kim, D. Su, D.H. Kim, J.Y. Lee, K.Y. Chung, E.A. Stach, Investigation of Changes in the Surface Structure of LixNi0.8Co0.15Al0.05O2 Cathode Materials Induced by the Initial Charge, Chem. Mater. 26 (2014) 1084–1092. doi:10.1021/cm403332s.

[22] F. Dogan, J.T. Vaughey, H. Iddir, B. Key, Direct Observation of Lattice Aluminum Environments in Li Ion Cathodes LiNi1–y–zCoyAlzO2 and Al-Doped LiNixMnyCozO2 via 27Al MAS NMR Spectroscopy, ACS Appl. Mater. Interfaces. 8 (2016) 16708–16717. doi:10.1021/acsami.6b04516.

[23] G. Liu, K.-S. Park, J. Song, J.B. Goodenough, Influence of thermal history on the electrochemical properties of Li[Ni0.5Mn1.5]O4, J. Power Sources. 243 (2013) 260–266. doi:http://dx.doi.org/10.1016/j.jpowsour.2013.05.189.

[24] M. Hu, X. Pang, Z. Zhou, Recent progress in high-voltage lithium ion batteries, J. Power Sources. 237 (2013) 229–242. doi:10.1016/j.jpowsour.2013.03.024.

[25] M. Kunduraci, G.G. Amatucci, The effect of particle size and morphology on the rate capability of 4.7 V LiMn1.5+δNi0.5-δO4 spinel lithium-ion battery cathodes, Electrochim. Acta. 53 (2008) 4193–4199. doi:10.1016/j.electacta.2007.12.057.

[26] J.B. Goodenough, K.-S.S. Park, The Li-Ion Rechargeable Battery: A Perspective, J. Am. Chem. Soc. 135 (2013) 1167–1176. doi:10.1021/ja3091438.

[27] J.B. Goodenough, Y. Kim, Challenges for rechargeable Li batteries, Chem. Mater. 22 (2010) 587–603. doi:10.1021/cm901452z.

[28] T.F. Yi, J. Mei, Y.R. Zhu, Key strategies for enhancing the cycling stability and rate capacity of LiNi0.5Mn1.5O4 as high-voltage cathode materials for high power lithium-ion batteries, J. Power Sources. 316 (2016) 85–105. doi:10.1016/j.jpowsour.2016.03.070.

[29] R. Van Noorden, The rechargeable revolution: A better battery, Nature. 507 (2014) 26–28. doi:10.1038/507026a.

[30] C.M. Julien, A. Mauger, Review of 5-V electrodes for Li-ion batteries: Status and trends, Ionics (Kiel). 19 (2013) 951–988. doi:10.1007/s11581-013-0913-2.

[31] D. Liu, J. Han, J.B. Goodenough, Structure, morphology, and cathode performance of Li1-x[Ni0.5Mn1.5]O4 prepared by coprecipitation with oxalic acid, J. Power Sources. 195 (2010) 2918–2923. doi:10.1016/j.jpowsour.2009.11.024.

[32] A. VAN DER VEN, J. BHATTACHARYA, A.A. Belak, Understanding Li Diffusion in Li-Intercalation Compounds, Acc. Chem. Res. 46 (2013) 1216–1225.

[33] D. Liu, W. Zhu, J. Trottier, C. Gagnon, F. Barray, A. Guerfi, A. Mauger, H. Groult, C.M. Julien, J.B. Goodenough, K. Zaghi, Spinel materials for high-voltage cathodes in Li-ion batteries, Rsc Adv. 4 (2014) 154–167. doi:10.1039/c3ra45706k.

[34] L. Wang, H. Li, X. Huang, E. Baudrin, A comparative study of Fd-3m and P4332 “LiNi0.5Mn1.5O4,” Solid State Ionics. 193 (2011) 32–38. doi:10.1016/j.ssi.2011.04.007.

[35] K.R. Chemelewski, E.S. Lee, W. Li, A. Manthiram, Factors influencing the electrochemical properties of high-voltage spinel cathodes: Relative impact of morphology and cation ordering, Chem. Mater. 25 (2013) 2890–2897. doi:10.1021/cm401496k.

[36] B.L. Cushing, J.B. Goodenough, Influence of carbon coating on the performance of a LiMn0.5Ni0.5O2 cathode, Solid State Sci. 4 (2002) 1487–1493. doi:10.1016/S1293-2558(02)00044-4.

[37] X.-Q. Yang, J. McBreen, W.-S. Yoon, C.P. Grey, Crystal structure changes of LiMn0.5Ni0.5O2 cathode materials during charge and discharge studied by synchrotron based in situ XRD, Electrochem. Commun. 4 (2002) 649–654. doi:10.1016/S1388-2481(02)00406-X.

[38] W.-S. Yoon, C.P. Grey, M. Balasubramanian, X.-Q. Yang, J. McBreen, In Situ X-ray Absorption Spectroscopic Study on LiNi0.5Mn0.5O2 Cathode Material during Electrochemical Cycling, Chem. Mater. 15 (2003) 3161–3169. doi:10.1021/cm030220m.

[39] F. Amalraj, D. Kovacheva, M. Talianker, L. Zeiri, J. Grinblat, N. Leifer, G. Goobes, B. Markovsky, D. Aurbach, Synthesis of Integrated Cathode Materials xLi2MnO3· (1 − x) LiMn1 / 3Ni1 / 3Co1 / 3O2 (x = 0.3 , 0.5 , 0.7) and Studies of Their Electrochemical Behavior, J. Electrochem. Soc. . 157 (2010) A1121–A1130. doi:10.1149/1.3463782.

[40] C.S. Johnson, N. Li, C. Lefief, J.T. Vaughey, M.M. Thackeray, Synthesis, Characterization and Electrochemistry of Lithium Battery Electrodes: xLi2MnO3·(1 − x)LiMn0.333Ni0.333Co0.333O2 (0 ≤ x ≤ 0.7), Chem. Mater. 20 (2008) 6095–6106. doi:10.1021/cm801245r.

[41] P. Lanz, C. Villevieille, P. Novák, Ex situ and in situ Raman microscopic investigation of the differences between stoichiometric LiMO2 and high-energy xLi2MnO3·(1–x)LiMO2 (M = Ni, Co, Mn), Electrochim. Acta. 130 (2014) 206–212. doi:10.1016/j.electacta.2014.03.004.

[42] M.M. Thackeray, S.-H. Kang, C.S. Johnson, J.T. Vaughey, R. Benedek, S.A. Hackney, Li2MnO3-stabilized LiMO2 (M = Mn, Ni, Co) electrodes for lithium-ion batteries, J. Mater. Chem. 17 (2007) 3112–3125. doi:10.1039/B702425H.

[43] Y.-F. Deng, S.-X. Zhao, Y.-H. Xu, K. Gao, C.-W. Nan, Impact of P-Doped in Spinel LiNi0.5Mn1.5O4 on Degree of Disorder, Grain Morphology, and Electrochemical Performance, Chem. Mater. 27 (2015) 7734–7742. doi:10.1021/acs.chemmater.5b03517.

[44] G.T.-K. Fey, C.-Z. Lu, T.P. Kumar, Preparation and electrochemical properties of high-voltage cathode materials, LiMyNi0.5−yMn1.5O4 (M=Fe, Cu, Al, Mg; y=0.0–0.4), J. Power Sources. 115 (2003) 332–345. doi:10.1016/S0378-7753(03)00010-7.

[45] L. Shen, H. Li, E. Uchaker, X. Zhang, G. Cao, General Strategy for Designing Core–Shell Nanostructured Materials for High-Power Lithium Ion Batteries, Nano Lett. 12 (2012) 5673–5678. doi:10.1021/nl302854j.

[46] L. Wang, T. Maxisch, G. Ceder, A First-Principles Approach to Studying the Thermal Stability of Oxide Cathode Materials, Chem. Mater. 19 (2007) 543–552. doi:10.1021/cm0620943.

[47] N. Yabuuchi, Y. Makimura, T. Ohzuku, Solid-State Chemistry and Electrochemistry of LiCo1∕3Ni1∕3Mn1∕3O2 for Advanced Lithium-Ion Batteries: III. Rechargeable Capacity and Cycleability , J. Electrochem. Soc. . 154 (2007) A314–A321. doi:10.1149/1.2455585.

[48] N. Yabuuchi, K. Yoshii, S.-T. Myung, I. Nakai, S. Komaba, Detailed Studies of a High-Capacity Electrode Material for Rechargeable Batteries, Li2MnO3−LiCo1/3Ni1/3Mn1/3O2, J. Am. Chem. Soc. 133 (2011) 4404–4419. doi:10.1021/ja108588y.

[49] I. Belharouak, G.M. Koenig, K. Amine, Electrochemistry and safety of Li4Ti5O12 and graphite anodes paired with LiMn2O4 for hybrid electric vehicle Li-ion battery applications, J. Power Sources. 196 (2011) 10344–10350. doi:10.1016/j.jpowsour.2011.08.079.

[50] F. Brochu, A. Guerfi, J. Trottier, M. Kopeć, A. Mauger, H. Groult, C.M. Julien, K. Zaghib, Structure and electrochemistry of scaling nano C–LiFePO4 synthesized by hydrothermal route: Complexing agent effect, J. Power Sources. 214 (2012) 1–6. doi:10.1016/j.jpowsour.2012.03.092.

[51] F. Wu, M. Wang, Y. Su, L. Bao, S. Chen, A novel method for synthesis of layered LiNi1/3Mn1/3Co1/3O2 as cathode material for lithium-ion battery, J. Power Sources. 195 (2010) 2362–2367. doi:10.1016/j.jpowsour.2009.10.043.

[52] J. Liu, R. Jiang, X. Wang, T. Huang, A. Yu, The defect chemistry of LiFePO4 prepared by hydrothermal method at different pH values, J. Power Sources. 194 (2009) 536–540. doi:10.1016/j.jpowsour.2009.05.007.

[53] F. Wu, Z. Wang, Y. Su, Y. Guan, Y. Jin, N. Yan, J. Tian, L. Bao, S. Chen, Synthesis and characterization of hollow spherical cathode Li1.2Mn0.54Ni0.13Co0.13O2 assembled with nanostructured particles via homogeneous precipitation-hydrothermal synthesis, J. Power Sources. 267 (2014) 337–346. doi:10.1016/j.jpowsour.2014.05.097.

[54] S. Deng, D. Mao, H. Wang, B. Wang, J. Liu, Y. Ma, H. Yan, Preparation and electrochemical properties of double-shell LiNi0.5Mn1.5O4 hollow microspheres as cathode materials for Li-ion batteries, RSC Adv. 6 (2016) 45369–45375. doi:10.1039/C6RA05620B.

[55] T. Doi, Y. Iriyama, T. Abe, Z. Ogumi, Electrochemical Insertion and Extraction of Lithium Ion at Uniform Nanosized Li4/3Ti5/3O4 Particles Prepared by a Spray Pyrolysis Method, Chem. Mater. 17 (2005) 1580–1582. doi:10.1021/cm047848x.

[56] X. Huang, Y. You, Y. Ren, H. Wang, Y. Chen, X. Ding, B. Liu, S. Zhou, F. Chu, Spray drying-assisted synthesis of hollow spherical Li2FeSiO4/C particles with high performance for Li-ion batteries, Solid State Ionics. 278 (2015) 203–208. doi:10.1016/j.ssi.2015.06.019.

[57] T. Li, X. Li, Z. Wang, H. Guo, W. Peng, K. Zeng, Electrochemical properties of LiNi0.6Co0.2Mn0.2O2 as cathode material for Li-ion batteries prepared by ultrasonic spray pyrolysis, Mater. Lett. 159 (2015) 39–42. doi:10.1016/j.matlet.2015.06.075.

[58] B. Pişkin, M.K. Aydinol, Development and characterization of layered Li(NixMnyCo1−x−y)O2 cathode materials for lithium ion batteries, Int. J. Hydrogen Energy. 41 (2016) 9852–9859. doi:10.1016/j.ijhydene.2016.03.127.

[59] T.J. Boyle, M.A. Rodriguez, D. Ingersoll, T.J. Headley, S.D. Bunge, D.M. Pedrotty, S.M. De'Angeli, S.C. Vick, H. Fan, A Novel Family of Structurally Characterized Lithium Cobalt Double Aryloxides and the Nanoparticles and Thin Films Generated Therefrom, Chem. Mater. 15 (2003) 3903–3912. doi:10.1021/cm020902u.

[60] J.S. Park, A.U. Mane, J.W. Elam, J.R. Croy, Amorphous Metal Fluoride Passivation Coatings Prepared by Atomic Layer Deposition on LiCoO2 for Li-Ion Batteries, Chem. Mater. 27 (2015) 1917–1920. doi:10.1021/acs.chemmater.5b00603.

[61] J.S. Park, X. Meng, J.W. Elam, S. Hao, C. Wolverton, C. Kim, J. Cabana, Ultrathin Lithium-Ion Conducting Coatings for Increased Interfacial Stability in High Voltage Lithium-Ion Batteries, Chem. Mater. 26 (2014) 3128–3134. doi:10.1021/cm500512n.

[62] V.A. Sugiawati, F. Vacandio, M. Eyraud, P. Knauth, T. Djenizian, Porous NASICON-Type Li3Fe2(PO4)3 Thin Film Deposited by RF Sputtering as Cathode Material for Li-Ion Microbatteries, Nanoscale Res. Lett. 11 (2016) 365. doi:10.1186/s11671-016-1574-7.

[63] X. Zhang, F. Cheng, K. Zhang, Y. Liang, S. Yang, J. Liang, J. Chen, Facile polymer-assisted synthesis of LiNi0.5Mn1.5O4 with a hierarchical micro–nano structure and high rate capability, RSC Adv. 2 (2012) 5669. doi:10.1039/c2ra20669b.

[64] D. Wang, I. Belharouak, G. Zhou, K. Amine, Synthesis of Lithium and Manganese-Rich Cathode Materials via an Oxalate Co-Precipitation Method, J. Electrochem. Soc. 160 (2013) A3108–A3112. doi:10.1149/2.016305jes.

[65] L. Zhang, W. Borong, L. Ning, W. Feng, Hierarchically porous micro-rod lithium-rich cathode material Li1.2Ni0.13Mn0.54Co0.13O2 for high performance lithium-ion batteries, Electrochim. Acta. 118 (2014) 67–74. doi:10.1016/j.electacta.2013.11.186.

[66] Z. Yang, J. Lu, D. Bian, W. Zhang, X. Yang, J. Xia, G. Chen, H. Gu, G. Ma, Stepwise co-precipitation to synthesize LiNi1/3Co1/3Mn1/3O2 one-dimensional hierarchical structure for lithium ion batteries, J. Power Sources. 272 (2014) 144–151. doi:http://dx.doi.org/10.1016/j.jpowsour.2014.08.052.

[67] H. Liu, G. Zhu, L. Zhang, Q. Qu, M. Shen, H. Zheng, Controllable synthesis of spinel lithium nickel manganese oxide cathode material with enhanced electrochemical performances through a modified oxalate co-precipitation method, J. Power Sources. 274 (2015) 1180–1187. doi:10.1016/j.jpowsour.2014.10.154.

[68] A. Huizing, H.A.M. van Hal, W. Kwestroo, C. Langereis, P.C. van Loosdregt, Hydrates of Manganese (II) Oxalate, Mater. Res. Bull. 12 (1977) 605–611.

[69] R. Zhao, Z. Chen, Y. Zhang, P. Du, H. Chen, Ultrasonic/microwave-assisted co-precipitation method in the synthesis of Li1.1Mn0.433Ni0.233Co0.233O2 cathode material for lithium-ion batteries, Mater. Lett. 136 (2014) 160–163. doi:10.1016/j.matlet.2014.08.060.

[70] L. Li, X. Zhang, R. Chen, T. Zhao, J. Lu, F. Wu, K. Amine, Synthesis and electrochemical performance of cathode material Li1.2Co0.13Ni0.13Mn0.54O2 from spent lithium-ion batteries, J. Power Sources. 249 (2014) 28–34. doi:10.1016/j.jpowsour.2013.10.092.

[71] A. Van Bomme, J.R. Dahn, Analysis of the growth mechanism of coprecipitated spherical and dense nickel, manganese, and cobalt-containing hydroxides in the presence of aqueous ammonia, Chem. Mater. 21 (2009) 1500–1503. doi:10.1021/cm803144d.

[72] L. Wan, Y. Deng, C. Yang, H. Xu, X. Qin, G. Chen, Ni/Mn ratio and morphology-dependent crystallographic facet structure and electrochemical properties of the high-voltage spinel LiNi0.5Mn1.5O4 cathode material, RSC Adv. 5 (2015) 25988–25997. doi:10.1039/C5RA03602J.

[73] W. Luo, Effect of morphology on the physical and electrochemical properties of the high-voltage spinel cathode LiMn1.5Ni0.5O4, J. Alloys Compd. 636 (2015) 24–28. doi:10.1016/j.jallcom.2015.02.163.

[74] K.R. Chemelewski, D.W. Shin, W. Li, A. Manthiram, Octahedral and truncated high-voltage spinel cathodes: the role of morphology and surface planes in electrochemical properties, J. Mater. Chem. A. 1 (2013) 3347. doi:10.1039/c3ta00682d.

[75] Y. Qian, Y. Deng, L. Wan, H. Xu, X. Qin, G. Chen, Investigation of the Effect of Extra Lithium Addition and Postannealing on the Electrochemical Performance of High-Voltage Spinel LiNi0.5Mn1.5O4 Cathode Material, J. Phys. Chem. C. 118 (2014) 15581–15589. doi:10.1021/jp503584k.

[76] H. Kawai, M. Nagata, H. Tukamoto, A.R. West, High-voltage lithium cathode materials, J. Power Sources. 81–82 (1999) 67–72. doi:10.1016/S0378-7753(98)00204-3.

[77] H.B. Lin, Y.M. Zhang, H.B. Rong, S.W. Mai, J.N. Hu, Y.H. Liao, L.D. Xing, M.Q. Xu, X.P. Li, W.S. Li, Crystallographic facet- and size-controllable synthesis of spinel LiNi0.5Mn1.5O4 with excellent cyclic stability as cathode of high voltage lithium ion battery, J. Mater. Chem. A. 2 (2014) 11987–11995. doi:10.1039/C4TA01810A.

[78] W. Ren, R. Luo, Z. Liu, X. Tan, Z. Fu, S. Liao, Effect of Ni/Mn ratio on the performance of LiNi x Mn2 − x O4 cathode material for lithium-ion battery, Ionics (Kiel). 20 (2014) 1361–1366. doi:10.1007/s11581-014-1114-3.

[79] K. Amine, H. Tukamoto, H. Yasuda, Y. Fujita, Preparation and electrochemical investigation of LiMn2 − xMexO4 (Me: Ni, Fe, and x = 0.5, 1) cathode materials for secondary lithium batteries, J. Power Sources. 68 (1997) 604–608. doi:10.1016/S0378-7753(96)02590-6.

[80] G.M. Koenig, I. Belharouak, H. Deng, Y.-K. Sun, K. Amine, Composition-Tailored Synthesis of Gradient Transition Metal Precursor Particles for Lithium-Ion Battery Cathode Materials, Chem. Mater. 23 (2011) 1954–1963. doi:10.1021/cm200058c.

[81] G.M. Koenig, I. Belharouak, H.M. Wu, K. Amine, Hollow lithiated metal oxide particles as lithium-ion battery cathode materials, Electrochim. Acta. 56 (2011) 1426–1431. doi:10.1016/j.electacta.2010.10.066.

[82] J. Fan, G. Li, D. Luo, C. Fu, Q. Li, J. Zheng, L. Li, Hydrothermal-Assisted Synthesis of Li-Rich Layered Oxide Microspheres with High Capacity and Superior Rate-capability as a Cathode for Lithium-ion Batteries, Electrochim. Acta. 173 (2015) 7–16. doi:10.1016/j.electacta.2015.05.028.

[83] Z. Zheng, X. Guo, S. Chou, W. Hua, H. Liu, Electrochimica Acta Designed Synthesis and Their Improved Electrochemical Performance, Electrochim. Acta. 191 (2016) 401–410. doi:10.1016/j.electacta.2016.01.092.

[84] H. Groult, T. Nakajima, N. Kumagai, Characterization and Electrochemical Properties of LiNi0.5Mn1.5O4 Prepared by a Carbonate Co-Precipitation Method, Int. J. Electrochem. Sci. 9 (2014) 7712–7724.

[85] D. Wang, I. Belharouak, G.M. Koenig, G. Zhou, K. Amine, Growth mechanism of Ni0.3Mn0.7CO3 precursor for high capacity Li-ion battery cathodes, J. Mater. Chem. 21 (2011) 9290. doi:10.1039/c1jm11077b.

[86] S. Zhang, C. Deng, B.L. Fu, S.Y. Yang, L. Ma, Synthetic optimization of spherical Li[Ni1/3Mn1/3Co1/3]O2 prepared by a carbonate co-precipitation method, Powder Technol. 198 (2010) 373–380. doi:10.1016/j.powtec.2009.12.002.

[87] M. Noh, J. Cho, Optimized Synthetic Conditions of LiNi0.5Co0.2Mn0.3O2 Cathode Materials for High Rate Lithium Batteries via Co-Precipitation Method, J. Electrochem. Soc. . 160 (2013) A105–A111. doi:10.1149/2.004302jes.

[88] H. Wang, X.-Z. Liao, Y. Yang, X. Yan, Y.-S. He, Z.-F. Ma, Large-Scale Synthesis of NaNi1/3Fe1/3Mn1/3O2 as High Performance Cathode Materials for Sodium Ion Batteries, J. Electrochem. Soc. . 163 (2016) A565–A570. doi:10.1149/2.0011605jes.

[89] H. Xie, G. Hu, K. Du, Z. Peng, Y. Cao, An improved continuous co-precipitation method to synthesize LiNi0.80Co0.15Al0.05O2 cathode material, J. Alloys Compd. 666 (2016) 84–87. doi:10.1016/j.jallcom.2016.01.064.

[90] G.B. Liu, H. Liu, Y.F. Shi, Electrochimica Acta The synthesis and electrochemical properties of x Li 2 MnO 3 –(1 − x) MO 2 (M = Mn 1 / 3 Ni 1 / 3 Fe 1 / 3) via co-precipitation method, Electrochim. Acta. 88 (2013) 112–116. doi:10.1016/j.electacta.2012.10.054.

[91] L. Li, S. Song, X. Zhang, R. Chen, J. Lu, F. Wu, K. Amine, Ultrasonic-assisted co-precipitation to synthesize lithium-rich cathode Li1.3Ni0.21Mn0.64O2+d materials for lithium-ion batteries, J. Power Sources. 272 (2014) 922–928. doi:10.1016/j.jpowsour.2014.08.063.

[92] A. Angermann, J. Töpfer, Synthesis of nanocrystalline Mn-Zn ferrite powders through thermolysis of mixed oxalates, Ceram. Int. 37 (2011) 995–1002. doi:10.1016/j.ceramint.2010.11.019.

[93] U. García-Couceiro, O. Castillo, A. Luque, G. Beobide, P. Román, A new hydrated phase of cobalt(II) oxalate: crystal structure, thermal behavior and magnetic properties of {[Co(μ-

ox)(H2O)2]·2H2O}n, Inorganica Chim. Acta. 357 (2004) 339–344. doi:10.1016/S0020-1693(03)00434-1.

[94] M.C. López, J.L. Tirado, C. Pérez Vicente, Structural and comparative electrochemical study of M(II) oxalates, M = Mn, Fe, Co, Ni, Cu, Zn, J. Power Sources. 227 (2013) 65–71. doi:10.1016/j.jpowsour.2012.08.100.

[95] S. Guillemet-Fritsch, M. Aoun-Habbache, J. Sarrias, A. Rousset, N. Jongen, M. Donnet, P. Bowen, J. Lemaître, High-quality nickel manganese oxalate powders synthesized in a new segmented flow tubular reactor, Solid State Ionics. 171 (2004) 135–140. doi:10.1016/S0167-2738(03)00282-0.

[96] J.C. Arrebola, A. Caballero, M. Cruz, L. Hernán, J. Morales, E.R. Castellón, Crystallinity Control of a Nanostructured LiNi0.5Mn1.5O4 Spinel via Polymer-Assisted Synthesis: A Method for Improving Its Rate Capability and Performance in 5 V Lithium Batteries, Adv. Funct. Mater. 16 (2006) 1904–1912. doi:10.1002/adfm.200500892.

[97] P. Axmann, G. Gabrielli, M. Wohlfahrt-Mehrens, Tailoring high-voltage and high-performance LiNi0.5Mn1.5O4 cathode material for high energy lithium-ion batteries, J. Power Sources. 301 (2016) 151–159. doi:10.1016/j.jpowsour.2015.10.010.

[98] F. Cheng, Y. Xin, J. Chen, L. Lu, X. Zhang, H. Zhou, Monodisperse Li1.2Mn0.6Ni0.2O2 microspheres with enhanced lithium storage capability, J. Mater. Chem. A. 1 (2013) 5301. doi:10.1039/c3ta00153a.

[99] Z. Qin, X. Zhou, Y. Xia, C. Tang, Z. Liu, Morphology controlled synthesis and modification of high-performance LiMnPO4 cathode materials for Li-ion batteries, J. Mater. Chem. 22 (2012) 21144. doi:10.1039/c2jm30821e.

[100] J. Zhang, X. Guo, S. Yao, W. Zhu, X. Qiu, Tailored synthesis of Ni0.25Mn0.75CO3 spherical precursors for high capacity Li-rich cathode materials via a urea-based precipitation method, J. Power Sources. 238 (2013) 245–250. doi:10.1016/j.jpowsour.2013.03.094.

[101] J.P. Robinson, G.M. Koenig, Tuning solution chemistry for morphology control of lithium-ion battery precursor particles, Powder Technol. 284 (2015) 225–230. doi:10.1016/j.powtec.2015.06.070.

[102] D.G. Wickham, SOLID-PHASE EQUILIBRIA IN THE SYSTEM NiO-Mn2O3-O2, J. Inorg. Nucl. Chem. 26 (1964) 1369–1377.

[103] J.G. Speight, N.A. Lange, Lange’s handbook of chemistry, McGraw-Hill Professional, Maidenhead, 2005.

[104] J. Vázquez, P.L. López-Alemany, P. Villares, R. Jiménez-Garay, A theoretical study on the crystallized fraction and the kinetic parameters by continuous heating techniques. Application to the devitrification of the Sb0.16As0.36Se0.48 alloy, Mater. Lett. 35 (1998) 50–57. doi:10.1016/S0167-577X(97)00216-4.

[105] M.E. Brown, A.K. Galwey, Thermal Decomposition of Manganese(II) Oxalate in Vacuum and in Oxygen, J. Chem. Soc. Faraday Trans. 1 Phys. Chem. Condens. Phases. 70 (1974) 1316–1324.

[106] N. Mancilla, V. Caliva, M.C. D’Antonio, A.C. González-Baró, E.J. Baran, Vibrational spectroscopic investigation of the hydrates of manganese(II) oxalate, J. Raman Spectrosc. 40 (2009) 915–920. doi:10.1002/jrs.2200.

[107] J. Topfer, J. Jung, Thermal decomposition of mixed crystals NixMn3-x(C2O4)3.6H2O, Thermochim. Acta. 202 (1992) 281–289.

[108] D.B. Wiles, R.A. Young, A new computer program for Rietveld analysis of X-ray powder diffraction patterns, J. Appl. Crystallogr. 14 (1981) 149–151. doi:10.1107/S0021889881008996.

[109] A. Feltz, J. Töpfer, F. Schirrmeister, Conductivity data and preparation routes for NiMn 2 O 4 thermistor ceramics, J. Eur. Ceram. Soc. 9 (1992) 187–191.

[110] J. Song, D.W. Shin, Y. Lu, C.D. Amos, A. Manthiram, J.B. Goodenough, Role of Oxygen Vacancies on the Performance of Li[Ni0.5−xMn1.5+x]O4 (x = 0, 0.05, and 0.08) Spinel Cathodes for Lithium-Ion Batteries, Chem. Mater. 24 (2012) 3101–3109.

[111] W.W. Wu, H.F. Xiang, G.B. Zhong, W. Su, W. Tang, Y. Zhang, Y. Yu, C.H. Chen, Ordered LiNi0.5Mn1.5O4 hollow microspheres as high-rate 5V cathode materials for lithium ion batteries, Electrochim. Acta. 119 (2014) 206–213. doi:10.1016/j.electacta.2013.12.017.

[112] M.M. Thackeray, Lithiated Oxides for Lithium Ion Batteries, J. Electrochem. Soc. 142 (1995) 2558–2563. doi:10.1149/1.2050053.

[113] K. Dokko, M. Mohamedi, N. Anzue, T. Itoh, I. Uchida, In situ Raman spectroscopic studies of LiNixMn2-xO4 thin film cathode materials for lithium ion secondary batteries, J. Mater. Chem. 12 (2002) 3688–3693. doi:10.1039/b206764a.

[114] Q. Zhong, A. Bonakclarpour, M. Zhang, Y. Gao, J.R. Dahn, Synthesis and Electrochemistry of LiNixMn2-xO4, J Electrochem Soc. 144 (1997) 205–213. doi:10.1149/1.1837386.

[115] W. Tang, Y. Hou, F. Wang, L. Liu, Y. Wu, K. Zhu, LiMn2O4 nanotube as cathode material of second-level charge capability for aqueous rechargeable batteries, Nano Lett. 13 (2013) 2036–2040. doi:10.1021/nl400199r.

[116] J.S. Kim, K. Kim, W. Cho, W.H. Shin, R. Kanno, J.W. Choi, A truncated manganese spinel cathode for excellent power and lifetime in lithium-ion batteries, Nano Lett. 12 (2012) 6358–6365. doi:10.1021/nl303619s.

[117] Y.-C. Jin, J.-G. Duh, Nanostructured LiNi0.5Mn1.5O4 cathode material synthesized by polymer-assisted co-precipitation method with improved rate capability, Mater. Lett. 93 (2013) 77–80. doi:10.1016/j.matlet.2012.11.039.

[118] W. Shao, S. Chen, L. He, H. Li, X. Guo, H. Zhu, H. Zhao, Y. Zhang, Electrochemical performances discharged to lower potential for co-precipitation method, 5th Int. Conf. Inf. Eng. Mech. Mater. (2015) 502–506.

[119] S.-K. Hong, S.-I. Mho, I.-H. Yeo, Y. Kang, D.-W. Kim, Structural and electrochemical characteristics of morphology-controlled Li[Ni0.5Mn1.5]O4 cathodes, Electrochim. Acta. 156 (2015) 29–37. doi:10.1016/j.electacta.2015.01.027.

3: Role of Coprecipitation and Calcination of Precursors on Phase Homogeneity and Electrochemical Properties of Battery Active Materials

3.1. Overview

Coprecipitation has previously been demonstrated to produce diverse compositions of battery precursor particles, frequently under the assumption that the precipitation of transition metals from the solution results in advantages with regards to efficient homogeneous local mixing of transition metal cations within the solid particles. Such mixing is generally considered as an advantage relative to solid state reaction of solid powders with the equivalent starting stoichiometry; however, very few studies have attempted to quantitatively confirm the impact of this local mixing on the resulting final materials. The extent to which local mixing from coprecipitation facilitates the mass transport of transition metals during the calcination process, which would be expected to aid in producing well crystallized single-phase particles, is not clear. Herein, this study will systematically compare the phase purity and crystallinity of oxide powders comprised of a blend of transition metals that were produced from either physical mixture of single transition metal precursors or multicomponent precursors produced via coprecipitation from solution. These experiments provide quantitative support for the role that local mixing, achieved via precipitation, plays in forming high crystallinity final materials with the desired phase. $LiMn_{1.5}Ni_{0.5}O_4$ was used as a model multicomponent target final material after calcination.

The element of this chapter has been published in the following journal:

Dong, H., Wang, A., & Koenig, G. M. (2018). Role of coprecipitation and calcination of precursors on phase homogeneity and electrochemical properties of battery active materials. Powder technology, 335, 137-146.

3.2. Introduction

Multicomponent transition metal (TM) oxides are the most commonly used cathode active materials in lithium-ion (Li-ion) batteries due to their broad capabilities in power and energy densities that can be tuned depending on the transition metal stoichiometry [1–5]. Many techniques have been developed to synthesize multicomponent TM oxides materials at both research and industrial scales [6–11]. Solid state synthesis is straightforward in that single component powders of each desired element can be measured at the desired stoichiometry directly and then physically mixed, but high temperature and/or long calcination times are required due to large diffusion distances for ions to form homogeneous final active materials [12–14]. Sol-gel synthesis is a modified solid state method that achieves very good mixing of the constituent elements, but the control over particle morphology is relatively limited [15–18]. Spray pyrolysis, a synthesis route commonly utilized in industry, is very scalable and has local mixing homogeneity but also limited particle morphology control [19–21]. Coprecipitation is another popular method to synthesize precursors for multicomponent TM oxides materials. Mixing between different TMs is assumed to be achieved at the atomic level during coprecipitation reactions, which in principle will reduce the requirement for aggressive firing conditions. The particle morphologies can be adjusted by tuning the reaction conditions and the particle morphologies can be well retained after the calcination process, which makes particle morphology control possible [22–25]. The method is fast, has low equipment needs, and is scalable. However, there are no reports on quantitative confirmation of the advantages of the assumed local mixing of precursors produced via coprecipitation, or to what extent the mixing facilitates ion diffusion during subsequent calcination. The focus of this study is to understand to what extent coprecipitation provides an advantage with local mixing of transition metals in the precursor particles, and for comparison we will also use solid state synthesis with physical mixing of single transition metal precursors.

$LiMn_{1.5}Ni_{0.5}O_4$ (LMNO) was chosen as the example final calcined material for this study. LMNO is commonly referred to as high voltage spinel due to its high redox potential at 4.7 V vs. Li/Li+ and because the material forms a spinel crystalline structure [1,26]. Depending on the distribution of Mn and Ni ions, LMNO may form two different crystallographic structures: the ordered P4332 space group and the disordered Fd-3m space group [27]. Correct stoichiometry is essential for extracting the maximum capacity from LMNO materials. According to previous reports, either Mn or Ni enrichment relative to the target Mn:Ni 3:1 stoichiometry may cause decreased material capacity and/or material stability during electrochemical charge/discharge [17,26]. The sensitivity of electrochemical properties to stoichiometry necessitates good mixing between Mn and Ni ions in the final active material particles, since localized Mn or Ni segregation will result in phase impurities and deteriorate resulting electrochemical properties of the materials. In this study, we will show the influence of local mixing and processing conditions on resulting final material crystal structure and electrochemical properties. The advantage of local mixing via coprecipitation relative to solid state physical blends of precursors is quantitatively characterized.

3.3. Material and Methods

3.3.1. Precursor Synthesis and Calcination

For the coprecipitation reaction, oxalate was used as the precipitation anion for all materials synthesized. Oxalate was chosen because Mn, Ni, and blends of Mn and Ni form stable oxalate dihydrates across the entire range of Mn:Ni ratios [17,28]. Other common precipitation anions, such as hydroxide and carbonate, have challenges with regards to impurity phases in the precipitate within certain stoichiometric ratios of Mn:Ni [10,24]. The dual functions of oxalate ions as both a precipitation reagent and a complexing agent also has the advantage of slowing down the precipitation rate which enables better control over the process within low concentration regimes [29].

The pure Mn and pure Ni TM precursors and the Mn:Ni 3:1 precursors were synthesized using coprecipitation via reaction of TM sulfate solutions with sodium oxalate solution. The synthesis was basically the same as used in the project of chapter 2. In brief, a pre-determined amount of TM sulfate salts (containing either Mn, Ni, or Mn:Ni 3:1 feed) was dissolved in 400 mL deionized water (DI water) and heated to 60°C. Separately, sodium oxalate was dissolved and heated to 60°C in 400 mL DI water. The precipitation was initiated by pouring the TM sulfate solution into the sodium oxalate solution all at once with vigorous stirring. The solution was assumed to be homogeneous upon mixing, with the total concentrations of TM and oxalate both 0.15 M after the initial mixing step. The reaction was allowed to proceed for 30 minutes after mixing the two solutions together, at which time the precipitates were filtered and rinsed with DI water. The initial solution concentrations for TM and oxalate were chosen to mitigate the deviation of the precipitate composition relative to the feed conditions for the Mn:Ni 3:1 and to result in high yield of precursor particles [30]. The composition of the resulting precursor from the 3:1 Mn:Ni feed was determined by inductively coupled plasma – optical emission spectroscopy (ICP-OES, Perkin Elmer Optima 8000) to be Mn: Ni 2.82:1. As reported in the literature [31,32], the pure Ni, pure Mn, and 3:1 Mn:Ni precursors all were oxalate dihydrates as determined via thermal gravimetric analysis. After filtration and rinsing, all precursor material powders were dried in a vacuum oven at 80°C overnight.

All precursor materials were calcined with a lithium salt to form lithium transition metal oxides. The obtained blend or pure precursor powders were mixed with 5% stoichiometric excess of LiOH for a target stoichiometric ratio of Li:TM 1.05:2. The mixing was conducted by hand using mortar and pestle for 10 minutes, and the mass of the powder for each batch of material mixed was kept around 3 grams for consistency. The powder mixtures were then transferred into crucibles and put into a furnace (Carbolite CWF 1300 box furnace) and fired under an air atmosphere. All the calcination processes used 1°C/minute ramping rate for heating and the materials were held at the target top temperature for a specified period of time followed by naturally cooling down to room temperature. The top temperature and hold time were parameters that were varied and are specified in the manuscript text for a given material.

3.3.2. Materials Characterization

Powder morphologies were characterized using a scanning electron microscope (SEM, FEI Quanta 650). Over 100 particles from SEM images were counted to determine the average particle size and standard deviation. The SEM was also equipped with energy-dispersive X-ray spectroscopy (EDS), which was used to identify elemental composition and distribution in the particles. The crystal structure of precursors and calcined materials was determined using powder X-ray diffraction (XRD, PANalytical X’pert ProMPD). Thermal gravimetric analysis (TGA, TA

Q50) was performed to determine the water stoichiometry in the precipitates and to locate the temperatures where decomposition processes occurred for the precursors. All the TGA tests were conducted in an air atmosphere with the ramping rate of 10°C/minute.

Electrochemical characterization of the final calcined active materials was conducted by using the calcined powders as the cathode active material in Li-ion battery cells paired with lithium metal anodes. The CR2032-type cells were fabricated with cathodes comprised of a blend of 80 wt% active materials, 10 wt% acetylene black, and 10 wt% polyvinylidene difluoride binder (dissolved in N-methyl-2-pyrrolidone). The electrode was cast from a slurry onto aluminum foil with a doctor blade set at a gap height of 250 □m. The electrode was first dried in air at 80°C for 24 hours, and then subsequently further dried under vacuum at 70°C for 3 hours. From the electrode foil, smaller disks with 1.6 cm2 area were punched to be used as cathodes in the coin cells. The cells, with the composite cathodes paired with lithium metal foil anode, were assembled inside an argon-filled glove box with polymer trilayer membrane as separators and LiPF6 dissolved in 3:7 vol. % ethylene carbonate:ethy methyl carbonate as the electrolyte. The cells were cycled within a voltage window of 3.6 - 4.9 V at room temperature using a MACCOR multichannel battery cycler. The cells were cycled galvanostatically at C/10, which corresponded to 14.67 mA g-1 of active material powder in the electrode, and the total charge/discharge current was adjusted by the amount of active material within a given electrode. The discharge profiles and dQ/dV profiles reported in this manuscript were from the fourth charge/discharge cycle, after the capacity stabilized from material structural activation during the first few cycles [33,34].

3.4. Results and Discussion

3.4.1. Experimental Results

Thermal gravimetrical analyses (TGA) were conducted on the pure manganese and nickel oxalates and the blend (3:1 Mn:Ni) oxalate. The TGA profiles can be found in the Appendix, Fig. S2. Two peaks in differential mass loss were observed for all precursors, one at lower temperature corresponding to structural water loss, and a peak at higher temperature which resulted from decomposition of the oxalate structure during formation of oxide. Even with the fast ramping speed (10°C min-1) in TGA, the dehydration and decomposition processes were completed below 350°C for all oxalate compounds. The melting point of LiOH is 450-471°C from ICSC data (CAS #: 1310-66-3), thus above this temperature the liquid LiOH should obtain good contact and distribution with the resulting TM oxide particles. Based on the TM oxalate decomposition temperatures and LiOH melting temperature, we chose a lowest target calcination temperature of 500°C. The highest calcination temperature was 850°C, which was a common calcination temperature for similar materials and has been reported to result in good crystallinity while producing desirable primary particle size [14,33,35]. An intermediate calcination temperature of 700°C was chosen because this temperature has been reported to promote formation of the ordered phase of LMNO [27,36]. The holding time at the target temperature of 700°C was also varied to understand how the hold duration impacts the crystallinity of the product materials, with the extended hold being expected to facilitate more significant ion diffusion which could help to anneal out metastable phases and enable improved crystallinity. The product samples were named in the format of M-T-t, where M designates the mixing method which was either physically mixing of the two precursors (P, which stands for ‘physical’ mixing the two TMs) or coprecipitation of the blend TM solution (S, which stands for ‘solution’ mixing the TMs); T represents for the target top temperature in degrees Celsius, and t is the holding time at the target temperature in hours. For example, the sample referred to as S-500-6 was obtained by calcining the coprecipitated precursor from the blend TM solution with LiOH at 500°C for 6 hours; whereas sample P-500-6 was obtained from calcining the physical mixture of the two pure TM precursors and LiOH at 500°C for 6 hours.

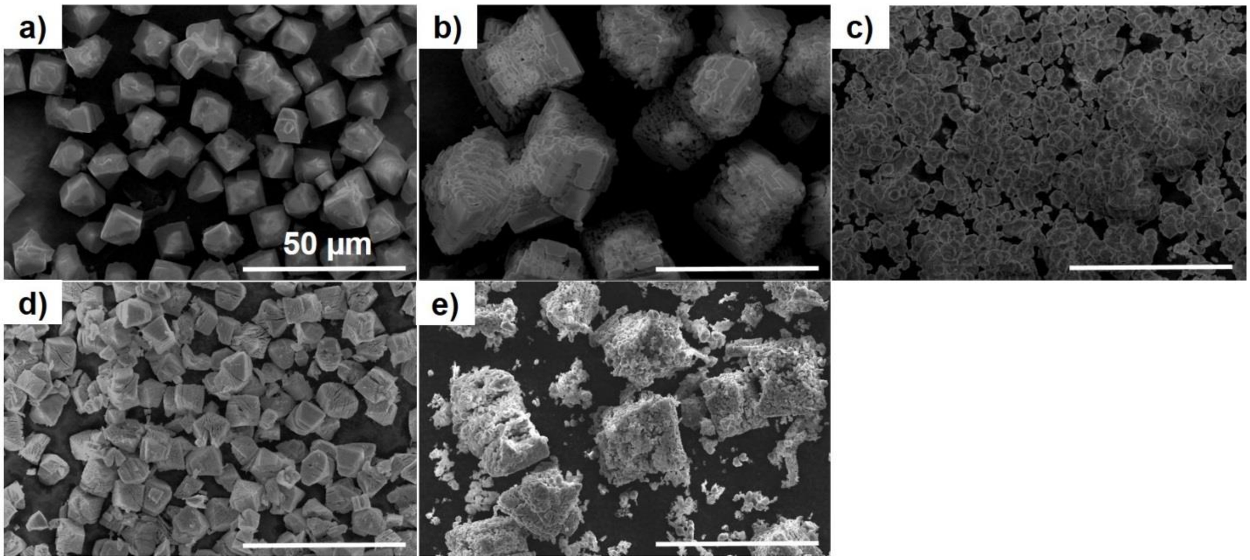

Figure 1. SEM images of oxalate precursor particles a) $Mn_{0.75}Ni_{0.25}C_2O_4 \cdot 2H_2O$, b) $MnC_2O_4 \cdot 2H_2O$, c) NiC2O4·2H2O; and calcined oxide particles of the d) solution mixed sample fired at 850°C for 6 hours (S-850-6) and e) physically mixed sample fired at 850°C for 6 hours (P-850-6). Scale bars all correspond to 50 um.

The manganese nickel blend oxalate (MnNiOx, chemical formula was $Mn_{0.74}Ni_{0.26}C_2O4 \cdot 2H_2O$ from ICP and TGA) particles exhibit octahedral secondary particle morphologies and average particle size of 10.2 +/- 1.0 µm (Fig. 1a). Pure manganese oxalate (MnOx, chemical formula $MnC_2O_4 \cdot 2H_2O$) precursors consisted of larger and more irregular particles, with overall particle dimensions of 24.0 +/- 1.9 µm (Fig. 1b). The pure nickel oxalate (NiOx, chemical formula NiC2O4·2H2O) precursors were aggregates of smaller primary particles, with secondary particle morphologies being roughly spherical with lengths of 3.6 +/- 0.7 µm (Fig. 1c). Significant aggregation of countable secondary particles can also be observed from the image. The SEM images of the solution mixed sample and physical mixed sample after firing with Li salt at 850 °C for 6 hours (S-850-6 and P-850-6) are shown in Fig. 1d, e, respectively. It can be clearly seen from Fig. 1d the S-850-6 particles retained the secondary morphology of the precursor (Fig. 1a) after calcination. However, calcination resulted in the formation of nanometers-scale primary particles agglomerated together, with new pores that resulted from the escape of H2O and CO2 gases from the inner structure during decomposition of the oxalate and shrinkage of the structure from crystallization [37,38]. SEMs of the calcined physically mixed samples (Fig. 1e), resulting from calcination of a blend of the precursors shown in Fig. 1b, c revealed secondary morphologies consistent with the initial morphologies of both MnOx and NiOx precursors. The larger particles were consistent with the initial morphology of MnOx particles (Fig. 1b) and the smaller irregular shaped particles were consistent with NiOx particles (Fig. 1c). The segregation of secondary particles after calcination indicates poor intermixing during firing of the physical mixture. This clear segregation of particles appeared with all the physically mixed samples, and additional SEMs can be found in Appendix, Fig. S6.

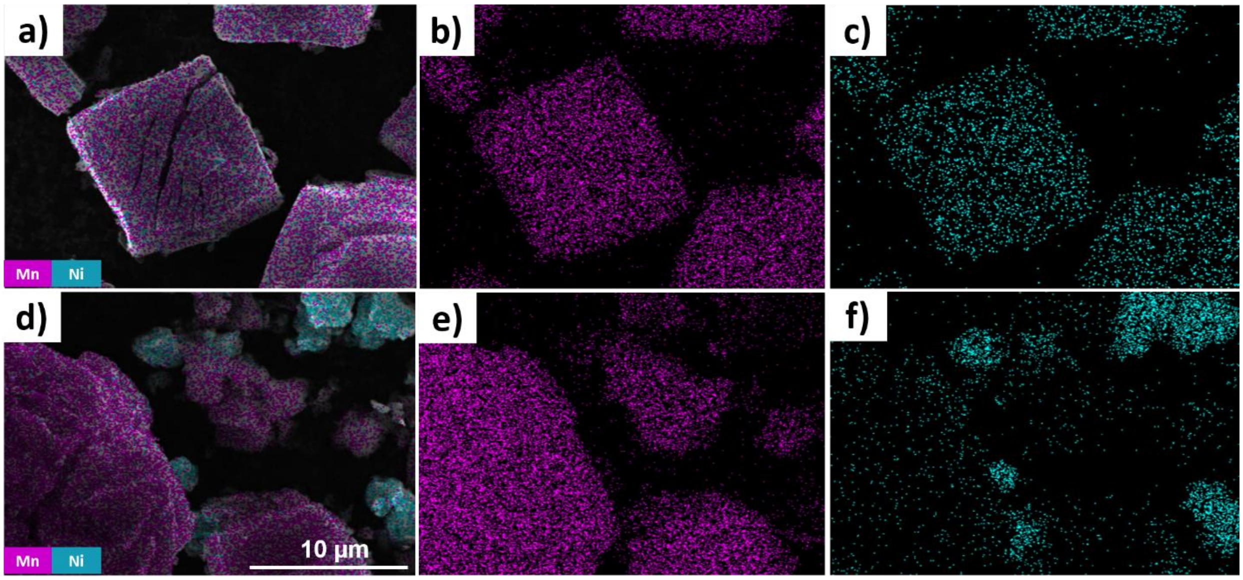

Figure 2. EDS elemental compositional maps of a) solution mixed sample fired at 500°C for 6 hours (S-500-6 particles). EDS maps of the same region as a) with individual maps of only b) Mn and c) Ni. EDS elemental compositional maps of d) physically mixed sample fired at 500°C for 6 hours (P-500-6 particles). EDS maps are also shown of the same region as d) with individual maps for e) Mn and f) Ni. For all images, magenta corresponds to Mn and blue corresponds to Ni. All scale bars correspond to 10 µm.

For further evidence to support the impact of TM ion mixing in the precursor, EDS was performed on calcined oxides prepared using precursors that were either solution mixed or physically mixed, and the results can be found in Fig 2. Fig. 2a shows the EDS elemental map of the solution mixed sample fired at 500°C for 6 hours (S-500-6) with Fig. 2b, c showing the individual maps of only Mn and Ni respectively. Fig. 2d shows the EDS elemental maps of the physically mixed sample fired at 500°C for 6 hours (P-500-6) with Fig. 2e, f showing the individual maps of only Mn and Ni respectively. As can be seen in the S-500-6 sample (Fig. 2a), Mn and Ni were evenly distributed in all the particles in the image region. Any elemental segregation would be at a length scale that could not be observed in the SEM-EDS. Solution mixed samples fired at higher temperature also appeared homogeneous in EDS maps (data not shown). In contrast, the physically mixed P-500-6 sample image (Fig. 2d) had clearly segregated regions of Mn and Ni within the original particles and there was relatively low inter-diffusion of TMs between constituent particles. The individual TM maps (Fig. 2e, f) show clear regions that are effectively pure Mn and pure Ni particles. Raising the calcination temperature and/or time did not significantly improve inter-diffusion level of TM ions observed in EDS (physically mixed samples fired at higher temperatures and longer times can be found in the Appendix, Fig. S7). In summary, EDS observations indicated there was significantly more inter-diffusion between Mn and Ni ions for samples with solution mixing compared to samples with physical mixing across all processing conditions. We do note that the physically mixed sample had more Mn and Ni inter-diffusion at the highest firing temperature (P-850-6) relative to samples fired at lower temperatures (Fig. S7a), and this observation will be discussed in the context of other characterization observations later in the manuscript.

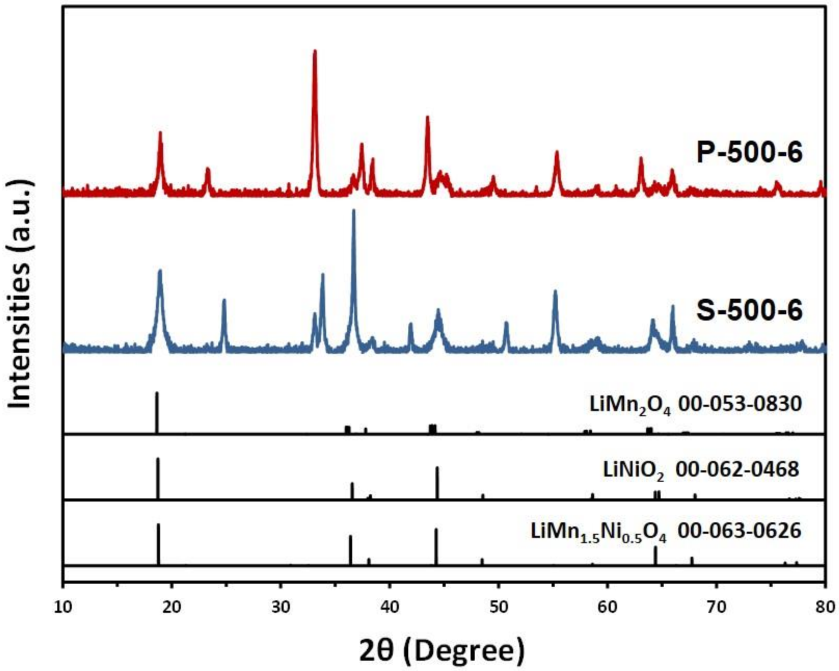

Figure 3. (Top) Powder XRD patterns and (Bottom) the relevant reference patterns from the literature. Collected patterns from top to bottom correspond to physically mixed sample fired at 500° for 6 hours (P-500-6, red) and solution mixed sample fired at 500°C for 6 hours (S-500-6, blue). The peak positions of the reference pattern of the potential lithiated TM oxide species are shown with their PDF card numbers at the bottom.

XRD patterns were obtained to understand the resulting crystal structure of the materials after different synthesis conditions. Fig. 3 shows the XRD patterns of the solution mixed and physically mixed samples fired at 500°C for 6 hours. The reference patterns of the potential lithiated TM oxide species are also shown at the bottom of Fig. 3. Oxide materials resulting from calcining the precursors in the absence of lithium salt were also obtained and analyzed, and the XRD patterns for these materials can be found in the Appendix, Fig. S8. The physically mixed sample fired with no LiOH added can be indexed with the patterns of Mn_2O_3 and NiO (PDF card codes being 04-007-0856 and 04-007-8202, respectively). This was consistent with the SEM images where Mn-dominant particles and Ni-dominant particles showed clear segregation, indicating that that the pure Mn precursor a pure Ni precursor formed pure Mn and Ni oxides, without much inter-diffusion of the two species. The peaks for these pure TM oxides also were present in the XRD pattern of the lithiated physically mixed sample (P-500-6, Fig. 3); the two most intense peaks: 2θ=33.1° and 2θ=43.4°, were consistent with Mn_2O_3 and NiO, respectively. Other peaks which appeared in the pattern were consistent with the patterns of LiMn2O4 and LiNiO2 (PFE card numbers being 00-053-0830 and 00-062-0468, respectively). This observation was consistent with Li diffusing into the individual pure TM particles and converting some of the Ni and Mn oxides into lithiated oxides of Ni and Mn. LMNO structure may also have formed to an extent, but it was difficult to confirm the presence of LMNO directly from the XRD due to the overlap between LMNO and the pure transition metal lithiated oxide¬ peaks [39]. The failure to form detectable amounts of target LMNO material for the physical mixture can be explained by the much greater distance between Mn and Ni TM ions when isolated in their particle domains, which made inter-diffusion of TM ions difficult. The XRD pattern of the S-500-6 sample, in contrast, exhibited intense peaks that were consistent with LMNO structures; and any peaks not consistent with LMNO were in line with those of the LiOH-free calcined control sample, and aligned well with the peaks from $MnNiO_3$ (PDF card number 04-002-0893, peaks at 2θ=24.8, 36.6, and 50.8°) and Mn_2O_3 (peaks at 2θ=33.6 and 55.2°). These lithium-free oxide peaks were much weaker in the lithiated sample. Tiny amounts of $LiMn_2O_4$ or $LiNiO_2$ may also exist in the lithiated material structure due to the incomplete inter-diffusion between Mn and Ni ions, but it is difficult to distinguish these materials from the LMNO peaks in the pattern. The comparison between the XRD patterns of S-500-6 and P-500-6 samples was consistent with the picture that better mixing between Mn and Ni ions in the solution mixed precursor from coprecipitation reactions facilitated formation of final active materials with collocated Mn and Ni ions in the final oxide structures after firing even at the most moderate temperature. The isolation of TM ions in larger particles for the physically mixed sample rendered the inter-diffusion more challenging to complete due to the long diffusion distance, and thus there was likely less LMNO formed for an equivalent firing procedure.

The XRD patterns of both the solution mixed and physical mixed samples which were fired at 700°C for 6 hours (S-700-6 and P-700-6), 850°C for 6 hours (S-850-6 and P-850-6), and 700°C for 12 hours (S-700-12 and P-700-12) are shown in Fig. 4, with the solution mixed samples in Fig. 4a and physically mixed samples in Fig. 4b for comparison. The peaks corresponding to the unlithiated TM oxide species are also marked on the patterns with designated symbols. Within the solution mixed series, S-700-6 still exhibited peaks corresponding to $MnNiO_3$ and Mn_2O_3 (marked with a star and triangle, respectively) which had been observed in the S-500-6 sample (Fig 3), whereas both S-700-12 and S-850-6 no longer contained these impurity peaks and all peaks were consistent with the LMNO spinel structure. The S-700-12 sample, however, had sharper peaks compared to S-850-6, which reflected higher crystallinity. The Scherrer formula, $d=K\lambda/(FWHM\cdot\cos\theta)$, was used to estimate the crystal sizes of the calcined samples, where the shape factor was set equal to 0.9, $\boldsymbol{\lambda}$ was the x-ray wavelength (1.5406 Å), and FWHM is the full width at half maximum for a peak located at the given 2θ [40]. Using the intense peaks at 2θ=18.88°, the crystal sizes calculated for the three samples S-700-6, S-850-6, and S-700-12 were 31.8, 25.6, and 34.7 nm (listed in Table 1, which were consistent with other reports for similar materials [41]. (Note that these are estimates of the crystal grain size, which could be significantly smaller than the primary particle size in the calcined material.) These results indicated that firing the solution mixed sample at 700°C for longer times facilitated crystal growth, while increasing the temperature from 700°C to 850°C may have stressed the material and crystal grains due to oxygen loss [42,43]. Comparing the XRD peaks of the physically mixed samples shown in Fig. 4b, P-700-6 peaks were at locations consistent with a mixture of both unlithiated TM oxides (Mn2O3 and NiO, marked with triangle and cube on Fig. 4b, respectively) and lithiated oxides (LiMn2O4 and LiNiO2). P-850-6 and P-700-12 samples resulted in less intense unlithiated oxide peaks and stronger peaks from the lithiated species; particularly, the unlithiated oxides peaks in sample P-850-6 almost disappeared (the peaks at $2\theta=33.6$ and 55.3° labeled in the pattern of P-700-6 which belong to Mn2O3). However, similar to the solution mixed samples, the physically mixed sample fired for a longer time at 700°C exhibited improved crystallinity, as indicated by stronger peak intensity. The crystal sizes calculated using the Scherrer formula for P-700-6, and P-850-6, and P-700-12 are listed in Table 1. The slight increase of grain size of P-700-12 relative to P-700-6 and the decrease of grain size after increasing the temperature from 700°C to 850°C followed the same trend as in the solution mixed samples. These results indicated that for the physically mixed sample higher temperature firing resulted in greater conversion of the unlithiated oxide to lithiated oxide, while this improved conversion was accompanied lower crystallinity relative to a longer firing time at a lower temperature.

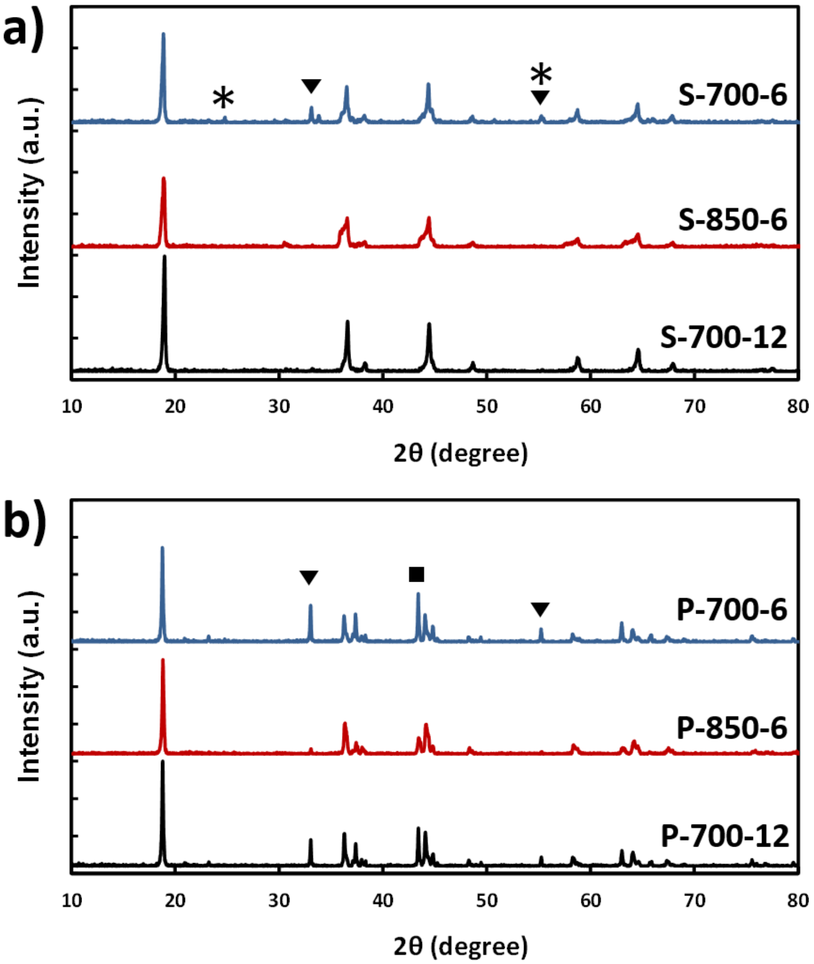

Figure 4. XRD patterns of the a) solution mixed and b) physical mixed samples calcined at different target temperatures (700°C or 850°C, as labeled on the Figure) and for different holding times at the target temperature (6 or 12 hours, as labeled on the Figure). Peaks of unlithiated oxides are marked with special labels: Mn2O3 marked by triangle, NiO marked by cube, and $MnNiO_3$ marked by *

According to conventional theory of crystallization in solid phase, the major driving force for grain growth results from the reduction of the system energy from decreasing the grain boundary. The kinetic equation of grain growth can be given by [44]:

$$d^n - d_0^n = kt \tag{1}$$

Where d is the average grain size from either calculation or experimental analysis, d_0 is the initial grain size, n is the scaling exponent, and t is the time that a material is held at a given temperature where grain growth is occurring. In the equation, k is a temperature dependent constant which follows Arrhenius scaling, $k = Ae^{-E/RT}$. Assuming the initial grain size, d_0, is far less than the grain size after calcination, d, the equation can be rearranged as:

$$\ln d = \frac{1}{n}\left(\ln t + lnA - \frac{E}{RT}\right) \tag{2}$$

where for Equation 2 there is a linear relationship between $\ln d$ and $\ln t$. The plot $\ln d$ vs. $\ln t$ using the samples fired at 700°C for 6 hours, 12 hours, and 48 hours for both the solution mixed and physically mixed samples is shown in the Appendix, Fig. S9. A linear least-squares fit for the solution mixed sample data resulted in a R2 of 0.996 and a calculated n value equal to 6.5, and this n value is within the range of typical observations for crystal growth [44]. The fitting of the data from the physically mixed samples gives a R2 of 0.75 and n of 74.6, which indicates both a poor fit of a linear function and an unreasonably high value for n to reflect the grain growth behavior – possibly indicating that the grains were not growing at these conditions, at least within the resolution of the Scherrer technique. In summary, the solution mixed precursor materials when fired to 700°C had steady increases in grain size as the dwell time increased, while the physically mixed precursors had very similar grain sizes for all holding times.

Contrary to the observations of increasing the holding time, increasing the temperature of both solution mixed and physically materials did not result in increased grain sizes. The calculated grain size decreased after increasing the temperature from 700°C to 850°C for both cases. One possible cause for the grain size reduction at 850°C, as mentioned earlier, could have been because

LMNO and other Mn spinel materials are known to undergo oxygen loss at this high temperature [42,43] and the loss of oxygen from the structure may have negatively impacted the grain growth and resulting sizes. We also note that the calculated grain sizes of the physically mixed samples were larger than those of the solution mixed samples fired under the same condition. This may have been due to the initially high segregation of the Mn and Ni in the physically mixed samples, where the highly separated Mn and Ni ions quickly formed very pure regions of Mn oxides and Ni oxides which were of higher initial phase purity.

Table 1. Grain sizes calculated using the Scherrer equation for samples fired using different target temperatures and hold times.

Calcination Condition		Grain Size (nm)	
		Solution Mixed sample	Physically Mixed Sample
500°C	6hr	27.9	33.8
700°C	6hr	31.8	54.4
	12hr	34.7	55.8
	48hr	43.6	56.2
850°C	6hr	25.6	44.3

Table 2. Total electrochemical gravimetric capacities, capacities within high voltage and low voltage ranges, and the calculated material amounts from the electrochemical profiles.

Sample mixing types	Sample Names	Total Capacity (mAh/g)	Low Voltage (3.9-4.4 V) Capacity (mAh/g)	High Voltage (4.4-4.9 V) Capacity (mAh/g)	Calculated LMO amount (g/g)	Calculated LMNO amount (g/g)
Solution mixed samples	S-700-6	99.3	18.5	80.8	0.12	0.55
	S-850-6	109.4	15.5	93.8	0.10	0.64
	S-700-48	103.7	12.6	91.2	0.08	0.62
Physically mixed samples	P-700-6	69.5	57.5	12.1	0.39	0.08
	P-850-6	103.4	51.2	52.2	0.34	0.36
	P-700-48	81.5	64.8	16.7	0.44	0.11

This difference observed in transition metal distribution and crystal structure for final calcined materials resulting from solution versus physically mixed precursors suggested that the resulting materials would also have significantly different electrochemical properties. Fig. 5 shows the dQ/dV curves of the solution mixed (Fig. 5a) and physical mixed (Fig. 5b) LMNO samples, where the LMNO material was used as the active material in a composite cathode which was paired with a lithium metal anode. The firing conditions were 700°C for 6 hours, 700°C for 48 hours, and

850°C for 6 hours – this enabled comparison of the impact of firing time versus firing temperature on electrochemical properties of the materials. Consistent with the observation of only LMNO-type peaks for the solution mixed samples processed using firing temperatures higher than 700°C, the solution mixed samples all show clear dQ/dV peaks in the high voltage range (4.6 – 4.8 V vs. Li/Li+) consistent with LMNO high voltage spinel (Fig. 5a) [17]. Small peaks in 3.9-4.1 V range were also observed. The lower voltage capacity may come from either existing $LiMn_2O_4$ or $LiNiO_2$ in the structure or some fraction of Mn ions in the LMNO structure being reduced from Mn4+ to Mn3+ during synthesis [39]. The total capacities and capacities separated by the high voltage (4.4-4.9 V) and low voltage (3.9-4.4 V) ranges are listed in Table 2. Compared to S-700-6, both S-850-6 and S-700-48 had higher capacities in the high voltage range; meanwhile the low voltage capacities of S-850-6 and S-700-48 were both less than that of S-700-6. This means higher temperature and longer time both facilitated improved inter-diffusion of Mn and Ni ions, and the more complete formation of the target high voltage LMNO structure. The slightly higher low voltage capacity of sample S-850-6 compared to S-700-48 suggests partial reduction of some Mn4+ to Mn3+ after firing under 850°C, which would be consistent with oxygen loss from the material at this high temperature [42,43]. Two separate peaks appear in the high voltage range in the profiles of S-700-6 and S-850-6; the S-700-48 sample, however, is dominate in the higher voltage peak while the other peak at slightly lower voltage disappeared, which may have resulted from a larger ordered spinel phase domain in the LMNO structure [45].

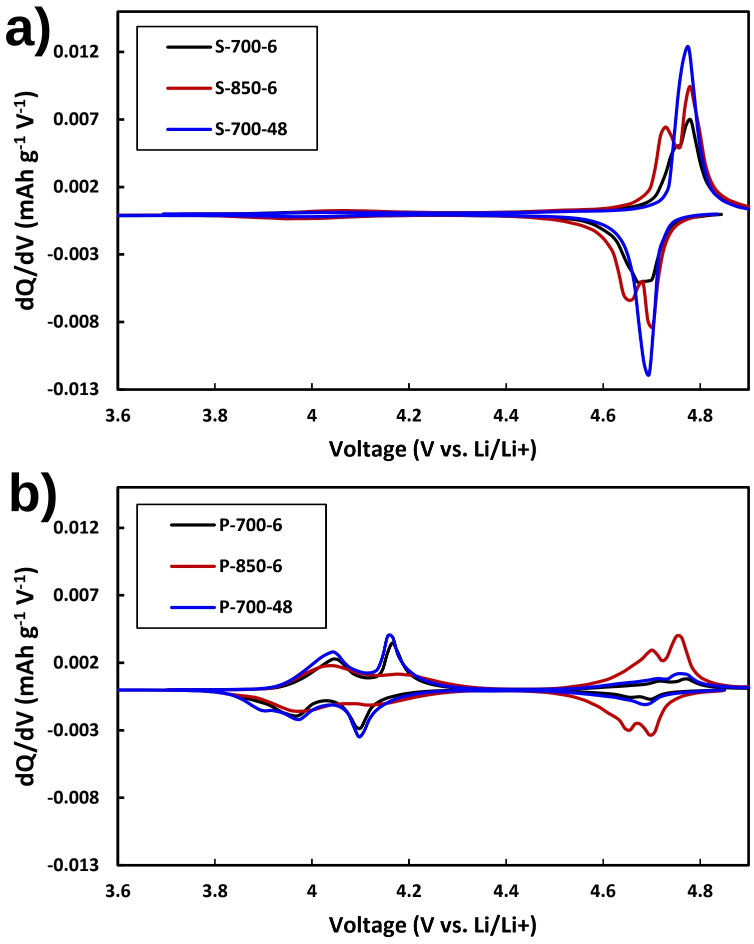

Figure 5. dQ/dV plots of coin cells using a) solution mixed and b) physically mixed LMNO samples as the cathode active materials paired with lithium metal anodes. dQ/dV was collected from the 4th cycle, and each cell was charged and discharged at a rate of C/10 in a voltage window between 3.6 to 4.9 V (vs. Li/Li+).

There were also clear differences in electrochemical properties for the physically mixed samples (Fig. 5b). All of the physically mixed samples had much lower total capacity and capacity in the high voltage range, indicating the initial segregation of the Mn and Ni significantly hindered the formation of the high voltage spinel phase which requires significant Mn and Ni intermixing at local level [45,46]. The P-700-6 sample showed two clear reversible peaks of Mn3+/Mn4+ redox activity in the range of 4.1 V vs. Li/Li+ [47]. We note there were very small peaks in the high voltage range consistent with Ni2+/Ni4+ redox couples in high voltage spinel structure [17], but the low capacity in this range indicated the conversion of the material to the high voltage spinel phase was minimal. The corresponding low voltage capacity and high voltage capacity were 57.4 and 12.06 mAh/g for the sample. In comparison, the P-850-6 sample had higher magnitude peaks and increased capacity in the high voltage range, which was accompanied by reductions in intensity and total capacity of the low voltage peaks; the high voltage capacity increased from 12.06 mAh/g to 52.21 mAh/g. The change in the distribution of electrochemical activity was consistent with the increased temperature facilitating increased inter-diffusion of the two transition metal ions, and thus the formation of new phases (high voltage LMNO spinel) in the solid samples. In contrast, the P-700-48 sample had no significant changes in dQ/dV profile relative to the P-700-6 sample, which indicated that the higher temperature was needed to facilitate the diffusion of the highly segregated TMs, and that increased time at 700°C was not sufficient to improve the formation of the high voltage LMNO spinel phase.

3.4.2. Model of Diffusion-Controlled Solid Reaction

Using the simplifying assumption that the precursor particles are all spheres, a model was applied to describe the ion diffusion and conversion of the particles to the desired LMNO phase during the solid reaction process initiated at the particle surface [48,49]. The schematic of the model is shown in Fig. 6. The initial solid component is represented as phase A with original radius r0. The diffusing species is represented as B and could be in either solid or liquid phase. The phase AB is the layer of the solid product that builds up as species B diffuses through the layer and reacts with A at the interface between A and AB. The growth of AB is assumed to be diffusion controlled, and at time t the product layer has a thickness of x, which results in the sphere of remaining phase A having a radius r, where $r = r_o - x$. The resulting volume of remaining A at time t is given by:

$$V = \frac{4}{3}\pi(r_o - x)^3. \tag{3}$$

Therefore, for a converted fraction of A, α, the unreacted fraction of component A is

$$(1-\alpha) = \frac{\frac{4}{3}\pi(r_o - x)^3}{\frac{4}{3}\pi {r_o}^3} = \frac{(r_o - x)^3}{{r_o}^3}. \tag{4}$$

Rearranging Equation 4 results in an expression for x:

$$x = r_o\left(1 - (1-\alpha)^{1/3}\right). \tag{5}$$

The above manipulation also assumed that the volume change of the product AB compared to species A was negligible. For the assumption that the diffusion across the product layer was the rate determining step, the parabolic diffusion law was also applied where the progression of product formation was proportional to the square root of time [49]:

$$x^2 = 2DV_mC_0t = k_1t \tag{6}$$

Where D is the diffusion coefficient of species B, V_m is the volume of product AB formed from per mole of species B, and C_0 is the concentration of B outside the sphere; therefore $k_1 = 2DV_mC_0$, was a constant used for convenience.

Combining Eq. (5) and (6) gives the relationship between reaction fraction and time:

$$\left(1 - (1-\alpha)^{1/3}\right)^2 = k' t \tag{7}$$

where $k' = {k_1}/{{r_0}^2} = \frac{2DV_mC_0}{{r_0}^2}$. Therefore, with estimates for the diffusion coefficient of the penetrating species at a given temperature and the original particle size, the reaction fraction can be calculated for a given firing time.

3.4.2.1. Solution Mixed Samples

For the case of solution mixed samples, Mn and Ni ions were assumed to be homogeneously distributed within the precursor particles and lithium ions were diffusing across the product layer and reacting with the unlithiated TM oxide to form the product LMNO. In other words, lithium ions were the penetrating species B in Fig. 6 and the sphere of A was a mixture of all the unlithiated TM oxides. AB in the schematic is the final product LMNO. The dependence of lithium ion diffusion coefficient through spinel structure can be represented using the Arrhenius equation:

$$D(T) = D_o e^{-E_0/kT} \tag{8}$$

Where D_o is the pre-exponential factor; E_0 is the diffusion activation energy; k is the Boltzmann constant which was equal to $8.617 \times 10^{-5} eV/K$ and T was the temperature in units of Kelvin. The pre-exponential factor and activation energy for lithium diffusion were taken from the literature and listed in Table 3. The original parameters were obtained for lithium ion diffusion through layered structures containing elements Mn, Ni, and Co, but provide a rough estimation for the materials in this study [50]. The diffusion coefficients at 700°C and 850°C were thus calculated using Eq. 8 and the values are listed in Table 3, along with the other two parameters needed to calculate $k^{'}$, in Eq.7. Further details for calculating these parameters can be found in the Appendix. Using the secondary particle size measured from SEM images, the original particle size $r_0 = 1.02 \times 10^{-5} m$, and thus value k' of lithium ions diffusion-controlled reaction process in Eq. 7 was obtained as 14.8 S^{-1}. Substituting the parameter in Equation 7, we calculated that at 700°C complete conversion to LMNO, corresponding to a reaction fraction of 1, would require only 0.068 seconds. The influence of the choice of original particle size will be discussed in further detail later, but has little influence in the current case because the lithium diffuses very quickly at the elevated temperature. The pores that develop in the secondary particles during calcination likely makes this timescale estimate based purely on lithium diffusion an overestimation.

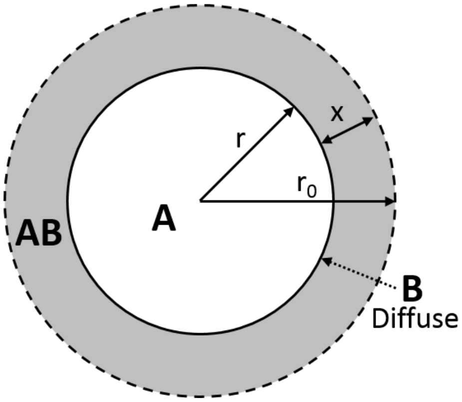

Figure 6. Schematic of model describing the ion diffusion into a sphere of one solid component and the reaction at the sphere surface producing the layer of product.

Even though the calculation above indicated that lithium diffusion was fast and should be complete within a second, the experimental LMNO amount in sample S-700-6 calculated based on the high voltage capacity during discharge, was only 0.55 g per gram of the sample (equivalently a conversion of only 0.61, the conversion calculation details can be found in the Appendix). While part of this lack of conversion was because spinel materials generally do not have complete delithiation during charge [43], the conversion of 0.61 suggested that lithium ion diffusion does not explicitly determine the conversion to the LMNO phase. We next considered that the inter-diffusion of Mn and Ni ions could be the process that limits the formation of LMNO high voltage spinel. To simplify the situation, we used the same diffusion-controlled reaction analysis and defined nickel ions as the penetrating species as in Fig. 6 and manganese ions along with other compounds (Li, O) as the static species in a fixed domain in phase A, although in reality the manganese ions also diffuse into nickel dominant regions during the inter-diffusion process [51]. Nickel was chosen as the penetrating species because according to a previous study it has greater diffusivity [52]. The diffusion coefficient parameters as well as other parameters for this case were also found in the literature [52] and are listed in Table 3. Given that at 700°C for 6 hours, the reaction fraction was 0.61, via substitution into Eq. 7 the original domain size was determined to be 386 nm. This large value relative to the atomic scale assumed for coprecipitation can be partially explained by the non-stoichiometry and impurity of the final active material - which hindered the full extraction of capacity and would result in a larger calculated domain size. By only considering diffusion of a single species, the energy associated with formation of the desired phase, as well as the formation and distribution of metastable phases and regions, has been ignored. These factors are essential for more accurate prediction of the reaction process during the calcination step and need further study. We do note that while the coprecipitation certainly results in improved local mixing of the TMs, it may not be truly atomic level mixing as has been described [53]. Further investigation into quantifying the extent of local mixing of TMs in the precursor will be the subject of future studies.

Table 3. Parameters used for diffusion-controlled solid reactions forming LMNO analysis [50,52].

	D_o (m^2/S)	E_o (eV)	$D_{700°C}$ (m^2/S)	$D_{850°C}$ (m^2/S)	V_m (m^3/mol)	C_0 (mol/m^3)
Li^+	1.7×10^{-7}	0.53	3.60×10^{-10}	7.11×10^{-10}	4.12×10^{-5}	6.10×10^{4}
Ni^{2+}	1.8×10^{-9}	2.10	2.40×10^{-20}	6.79×10^{-19}	8.23×10^{-5}	9.52×10^{4}

3.4.3.2. Physically Mixed Samples

In the case of physically mixed samples, the same calculation technique was applied as discussed above. Similar to the solution mixed samples, the lithium ion diffusion was estimated to be extremely fast due to the low activation energy and especially the high temperature applied, which would have completed the reaction in this idealized case within 0.1 seconds, resulting in lithiated products $LiMn_2O_4$ and LiNiO2. Although the operating voltage for the Mn3+/Mn4+ redox couple in $LiMn_2O_4$ and the Ni3+/Ni4+ redox couple in $LiNiO_2$ both have capacity close to 4.1 V vs. Li/Li+, and both could contribute to the low voltage capacity in the discharge profiles, for simplification of the materials comparison all the low voltage capacity was assigned to Mn3+/Mn4+ in $LiMn_2O_4$. The resulting calculated LMO was 0.39 g per gram of material for sample S-700-6, as given in Table 2 (all the other samples can also be found in the table). The sum of the LMO amount plus the LMNO amount, based on the low voltage and high voltage capacities, was still less than the unity. This indicated that all of the lithium could not be extracted from the active material. As stated above, we assumed that the nickel ions were the penetrating species diffusing from the NiO to form the product LMNO layer via reaction with lithiated manganese oxide LMO (refer to the schematic in Fig. 6). As in the case of the solution mixed samples, we used the secondary particle size from SEM image analysis as the original spherical size r0 and calculated the reaction fraction as a result of nickel ion diffusion for each physically mixed sample. The calculated values for samples P-700-6, P-850-6, and P-700-48 were 0.013, 0.21, and 0.038. The amount of final product LMNO per gram of the sample can then be calculated from the reaction fractions and the values are 0.01, 0.17, and 0.03 g/g. Further details on these calculations can be found in the Appendix. In order to see the influence of particle size on the reaction fraction for the three samples, we also used the primary particle size estimated from the SEM images as the original particle size (~ 1 µm) and used this value as the input for the calculation, resulting in reaction fractions increasing to 0.25, 0.86, and 0.59, and the calculated LMNO amounts were 0.21, 0.83, and 0.53 g/g for sample P-700-6, P-850-6, and P-700-48 respectively. For better comparison, the LMNO amounts calculated using either secondary or primary particle sizes are listed in Table 4 and are compared to the LMNO amounts determined from electrochemical data from Table 2. It can be seen that the electrochemically determined LMNO amounts were in between the two values for particle sizes. Though there were many simplifications to the calculation approach used, these results suggested that the average original particle size was between the primary and secondary particle sizes, which would be reasonable given that the secondary particle precursors have pores that open up during calcination and decomposition of the oxalate, and also that the primary particles fuse with each other making a network structure within the secondary particle as observed in the SEM images (Fig. S10) – both of these phenomena result in effective particle sizes between the observed primary and secondary particle length scales.

Comparing the reaction fractions calculated by using the secondary particle size between the three samples, we can see that increasing the firing temperature from 700°C to 850°C increased the reaction fraction as much as 16 times while expanding the firing time from 6 hours to 48 hours at 700°C only increased the conversion as much as 3 times, which were consistent with the XRD analyses. This observation was attributed to the large activation energy of TM ions diffusion which makes the diffusion coefficient highly sensitive to temperature, in particular the value of D850°C was more than one order of magnitude larger than D700°C (Table 3). Thus, for poorly mixed samples greater conversion to LMNO can be achieved with higher firing temperature as opposed to extended firing time at lower temperature – the P-850-6 sample had much more high voltage LMNO than the P-700-48 sample. In addition, the reaction fractions calculated from using the primary particle size decreased the gaps between sample P-850-6 and P-700-6, which indicated decreasing the initial particle size can aid in overcoming the diffusive intermixing limitation and promote lower temperature and/or time calcination to higher conversion of LMNO even though P-850-6 still gave the higher value.

Table 4. LMNO amounts in the physically mixed samples calculated using different particle sizes and determined from electrochemical data.

	Reaction fraction α		LMNO amounts (g/g of sample)		
Sample	Calculated using secondary particle size	Calculated using primary particle size	Calculated using secondary particle size	Calculated using primary particle size	Electrochemically determined
P-700-6	0.013	0.25	0.01	0.21	0.08
P-850-6	0.21	0.86	0.17	0.83	0.36
P-700-48	0.038	0.59	0.03	0.53	0.11

3.5. Conclusion

In this work we provided quantitative evidence that coprecipitation facilitates high levels of local mixing within precursor particles, and showed via different calcination procedures the advantages of local mixing from coprecipitation relative to physical mixing of individual single component precursors. Evidence of the improved mixing of the transition metals was provided by EDS, XRD, and electrochemical analysis. A simple diffusion limited reaction model suggested that the diffusion of Li+ was not limiting the conversion of solution mixed or physically mixed precursor materials to the resulting desired final material, and that the conversion was largely limited by the diffusion of transition metal species. The better local mixing of transition metal ions after coprecipitation reaction renders the synthesis process less energy consuming for conversion to final active material.

3.6. References

[1] J.B. Goodenough, K.-S.S. Park, The Li-Ion Rechargeable Battery: A Perspective, J. Am. Chem. Soc. 135 (2013) 1167–1176. doi:10.1021/ja3091438.

[2] J. Wang, X. Yao, X. Zhou, Z. Liu, Synthesis and electrochemical properties of layered lithium transition metal oxides, J. Mater. Chem. 21 (2011) 2544–2549. doi:10.1039/C0JM03388J.

[3] C.M. Julien, A. Mauger, Review of 5-V electrodes for Li-ion batteries: Status and trends, Ionics (Kiel). 19 (2013) 951–988. doi:10.1007/s11581-013-0913-2.

[4] H. Li, Q. Xu, X.-X. Shi, D.-W. Song, L.-Q. Zhang, Electrochemical performance of LiNi0.5Mn0.5O2 with different synthesis methods, Rare Met. 34 (2015) 580–585. doi:10.1007/s12598-013-0088-z.

[5] W. Ren, Y. Zhao, X. Hu, M. Xia, Preparation-microstructure-performance relationship of Li-rich transition metal oxides microspheres as cathode materials for lithium ion batteries, Electrochim. Acta. 191 (2016) 491–499. doi:10.1016/j.electacta.2016.01.089.

[6] L. Shen, H. Li, E. Uchaker, X. Zhang, G. Cao, General Strategy for Designing Core–Shell Nanostructured Materials for High-Power Lithium Ion Batteries, Nano Lett. 12 (2012) 5673–5678. doi:10.1021/nl302854j.

[7] X. Huang, Y. You, Y. Ren, H. Wang, Y. Chen, X. Ding, B. Liu, S. Zhou, F. Chu, Spray drying-assisted synthesis of hollow spherical Li2FeSiO4/C particles with high performance for Li-ion batteries, Solid State Ionics. 278 (2015) 203–208. doi:10.1016/j.ssi.2015.06.019.

[8] F. Wu, Z. Wang, Y. Su, Y. Guan, Y. Jin, N. Yan, J. Tian, L. Bao, S. Chen, Synthesis and characterization of hollow spherical cathode Li1.2Mn0.54Ni0.13Co0.13O2 assembled with nanostructured particles via homogeneous precipitation-hydrothermal synthesis, J. Power Sources. 267 (2014) 337–346. doi:10.1016/j.jpowsour.2014.05.097.

[9] J.S. Park, X. Meng, J.W. Elam, S. Hao, C. Wolverton, C. Kim, J. Cabana, Ultrathin Lithium-Ion Conducting Coatings for Increased Interfacial Stability in High Voltage Lithium-Ion Batteries, Chem. Mater. 26 (2014) 3128–3134. doi:10.1021/cm500512n.

[10] S. Zhang, C. Deng, B.L. Fu, S.Y. Yang, L. Ma, Synthetic optimization of spherical Li[Ni1/3Mn1/3Co1/3]O2 prepared by a carbonate co-precipitation method, Powder Technol. 198 (2010) 373–380. doi:10.1016/j.powtec.2009.12.002.

[11] G.M. Koenig, I. Belharouak, H. Deng, Y.-K. Sun, K. Amine, Composition-Tailored Synthesis of Gradient Transition Metal Precursor Particles for Lithium-Ion Battery Cathode Materials, Chem. Mater. 23 (2011) 1954–1963. doi:10.1021/cm200058c.

[12] G.T.-K. Fey, C.-Z. Lu, T.P. Kumar, Preparation and electrochemical properties of high-voltage cathode materials, LiMyNi0.5−yMn1.5O4 (M=Fe, Cu, Al, Mg; y=0.0–0.4), J. Power Sources. 115 (2003) 332–345. doi:10.1016/S0378-7753(03)00010-7.

[13] I. Belharouak, G.M. Koenig, K. Amine, Electrochemistry and safety of Li4Ti5O12 and graphite anodes paired with LiMn2O4 for hybrid electric vehicle Li-ion battery applications, J. Power Sources. 196 (2011) 10344–10350. doi:10.1016/j.jpowsour.2011.08.079.

[14] L. Wang, D. Chen, J. Wang, G. Liu, W. Wu, G. Liang, Synthesis of LiNi0.5Mn1.5O4cathode material with improved electrochemical performances through a modified solid-state method, Powder Technol. 292 (2016) 203–209. doi:10.1016/j.powtec.2016.02.002.

[15] Z.. Peng, C.. Wan, C.. Jiang, Synthesis by sol–gel process and characterization of LiCoO2 cathode materials, J. Power Sources. 72 (1998) 215–220. doi:10.1016/S0378-7753(97)02689-X.

[16] R. Thirunakaran, G.H. Lew, W.S. Yoon, Cerotic acid assisted sol-gel synthesis and electrochemical performance of double doped spinels (LiCrxMgyMn2-x-yO4) as cathode materials for lithium rechargeable batteries, Powder Technol. 301 (2016) 197–210. doi:10.1016/j.powtec.2016.05.064.

[17] K. Amine, H. Tukamoto, H. Yasuda, Y. Fujita, Preparation and electrochemical investigation of LiMn2 − xMexO4 (Me: Ni, Fe, and x = 0.5, 1) cathode materials for secondary lithium batteries, J. Power Sources. 68 (1997) 604–608. doi:10.1016/S0378-7753(96)02590-6.

[18] F. Wu, H. Lu, Y. Su, N. Li, L. Bao, S. Chen, Preparation and electrochemical performance of Li-rich layered cathode material, Li[Ni0.2Li0.2Mn0.6]O2, for lithium-ion batteries, J. Appl. Electrochem. 40 (2010) 783–789. doi:10.1007/s10800-009-0057-2.

[19] I. Taniguchi, N. Fukuda, M. Konarova, Synthesis of spherical LiMn2O4 microparticles by a combination of spray pyrolysis and drying method, Powder Technol. 181 (2008) 228–236. doi:10.1016/j.powtec.2007.05.011.

[20] M. Konarova, I. Taniguchi, Preparation of carbon coated LiFePO4 by a combination of spray pyrolysis with planetary ball-milling followed by heat treatment and their electrochemical properties, Powder Technol. 191 (2009) 111–116. doi:10.1016/j.powtec.2008.09.013.

[21] P. Yue, Z. Wang, W. Peng, L. Li, W. Chen, H. Guo, X. Li, Spray-drying synthesized LiNi0.6Co0.2Mn0.2O2 and its electrochemical performance as cathode materials for lithium ion batteries, Powder Technol. 214 (2011) 279–282. doi:10.1016/j.powtec.2011.08.022.

[22] D. Liu, J. Han, J.B. Goodenough, Structure, morphology, and cathode performance of Li1-x[Ni0.5Mn1.5]O4 prepared by coprecipitation with oxalic acid, J. Power Sources. 195 (2010) 2918–2923. doi:10.1016/j.jpowsour.2009.11.024.

[23] J.P. Robinson, G.M. Koenig, Tuning solution chemistry for morphology control of lithium-ion battery precursor particles, Powder Technol. 284 (2015) 225–230. doi:10.1016/j.powtec.2015.06.070.

[24] A. Van Bomme, J.R. Dahn, Analysis of the growth mechanism of coprecipitated spherical and dense nickel, manganese, and cobalt-containing hydroxides in the presence of aqueous ammonia, Chem. Mater. 21 (2009) 1500–1503. doi:10.1021/cm803144d.

[25] K.-M. Nam, H.-J. Kim, D.-H. Kang, Y.-S. Kim, S.-W. Song, Ammonia-free coprecipitation synthesis of a Ni-Co-Mn hydroxide precursor for high-performance battery cathode materials, Green Chem. 17 (2015) 1127–1135. doi:10.1039/C4GC01898B.

[26] Q. Zhong, A. Bonakdarpour, M. Zhang, Y. Gao, J.R. Dahn, Synthesis and Electrochemistry of LiNi x Mn2 − x O 4 , J. Electrochem. Soc. . 144 (1997) 205–213. doi:10.1149/1.1837386.

[27] L. Wang, H. Li, X. Huang, E. Baudrin, A comparative study of Fd-3m and P4332 “LiNi0.5Mn1.5O4,” Solid State Ionics. 193 (2011) 32–38. doi:10.1016/j.ssi.2011.04.007.

[28] D. Wang, I. Belharouak, G. Zhou, K. Amine, Synthesis of Lithium and Manganese-Rich Cathode Materials via an Oxalate Co-Precipitation Method, J. Electrochem. Soc. 160 (2013) A3108–A3112. doi:10.1149/2.016305jes.

[29] A. Angermann, J. Töpfer, Synthesis of nanocrystalline Mn-Zn ferrite powders through thermolysis of mixed oxalates, Ceram. Int. 37 (2011) 995–1002. doi:10.1016/j.ceramint.2010.11.019.

[30] H. Dong, G.M. Koenig Jr, Compositional control of precipitate precursors for lithium-ion battery active materials: role of solution equilibrium and precipitation rate, J. Mater. Chem. A. 5 (2017) 13785–13798. doi:10.1039/C7TA03653A.

[31] M.C. López, J.L. Tirado, C. Pérez Vicente, Structural and comparative electrochemical study of M(II) oxalates, M = Mn, Fe, Co, Ni, Cu, Zn, J. Power Sources. 227 (2013) 65–71. doi:10.1016/j.jpowsour.2012.08.100.

[32] N. Mancilla, V. Caliva, M.C. D'Antonio, A.C. González-Baró, E.J. Baran, Vibrational spectroscopic investigation of the hydrates of manganese(II) oxalate, J. Raman Spectrosc. 40 (2009) 915–920. doi:10.1002/jrs.2200.

[33] S.-K. Hong, S.-I. Mho, I.-H. Yeo, Y. Kang, D.-W. Kim, Structural and electrochemical characteristics of morphology-controlled Li[Ni0.5Mn1.5]O4 cathodes, Electrochim. Acta. 156 (2015) 29–37. doi:10.1016/j.electacta.2015.01.027.

[34] X. Zhang, F. Cheng, K. Zhang, Y. Liang, S. Yang, J. Liang, J. Chen, Facile polymer-assisted synthesis of LiNi0.5Mn1.5O4 with a hierarchical micro–nano structure and high rate capability, RSC Adv. 2 (2012) 5669. doi:10.1039/c2ra20669b.

[35] Q. Zhong, A. Bonakclarpour, M. Zhang, Y. Gao, J.R. Dahn, Synthesis and Electrochemistry of LiNixMn2-xO4, J Electrochem Soc. 144 (1997) 205–213. doi:10.1149/1.1837386.

[36] J.-H. Kim, S.-T. Myung, C.S. Yoon, S.G. Kang, Y.-K. Sun, Comparative Study of LiNi0.5Mn1.5O4-δ and LiNi0.5Mn1.5O4 Cathodes Having Two Crystallographic Structures: Fd 3̄m and P 4332, Chem. Mater. 16 (2004) 906–914. doi:10.1021/cm035050s.

[37] J. Topfer, J. Jung, Thermal decomposition of mixed crystals NixMn3-x(C2O4)3.6H2O, Thermochim. Acta. 202 (1992) 281–289.

[38] M.E. Brown, A.K. Galwey, Thermal Decomposition of Manganese(II) Oxalate in Vacuum and in Oxygen, J. Chem. Soc. Faraday Trans. 1 Phys. Chem. Condens. Phases. 70 (1974) 1316–1324.

[39] I. Belharouak, G.M. Koenig, J. Ma, D.P. Wang, K. Amine, Identification of LiNi0.5Mn1.5O4spinel in layered manganese enriched electrode materials, Electrochem. Commun. 13 (2011) 232–236. doi:10.1016/j.elecom.2010.12.021.

[40] R.B. Von Dreele, B.H. Toby, X-Ray Powder Diffraction, Charact. Mater. (2012) 1340–1360. doi:10.1002/0471266965.

[41] J.H. Kim, A. Huq, M. Chi, N.P.W. Pieczonka, E. Lee, C.A. Bridges, M.M. Tessema, A. Manthiram, K.A. Persson, B.R. Powell, Integrated nano-domains of disordered and ordered spinel phases in LiNi0.5Mn1.5O4 for li-ion batteries, Chem. Mater. 26 (2014) 4377–4386. doi:10.1021/cm501203r.

[42] A. Manthiram, K. Chemelewski, E.-S. Lee, A perspective on the high-voltage LiMn1.5Ni0.5O4 spinel cathode for lithium-ion batteries, Energy Environ. Sci. 7 (2014) 1339. doi:10.1039/c3ee42981d.

[43] J. Song, D.W. Shin, Y. Lu, C.D. Amos, A. Manthiram, J.B. Goodenough, Role of Oxygen Vacancies on the Performance of Li[Ni0.5−xMn1.5+x]O4 (x = 0, 0.05, and 0.08) Spinel Cathodes for Lithium-Ion Batteries, Chem. Mater. 24 (2012) 3101–3109.

[44] X. Song, D. Liu, Y. Zhang, Y. Ding, M. Li, S. Wang, X. He, Y. Qu, Grain growth kinetics of SnO2 nanocrystals synthesized by precipitation method, J. Wuhan Univ. Technol. Mater. Sci. Ed. 25 (2010) 929–934. doi:10.1007/s11595-010-0122-z.

[45] E.S. Lee, K.W. Nam, E. Hu, A. Manthiram, Influence of cation ordering and lattice distortion on the charge-discharge behavior of LiMn 1.5Ni 0.5O 4 Spinel between 5.0 and 2.0 v, Chem. Mater. 24 (2012) 3610–3620. doi:10.1021/cm3020836.

[46] K.R. Chemelewski, E.S. Lee, W. Li, A. Manthiram, Factors influencing the electrochemical properties of high-voltage spinel cathodes: Relative impact of morphology and cation ordering, Chem. Mater. 25 (2013) 2890–2897. doi:10.1021/cm401496k.

[47] J.M. Tarascon, The Spinel Phase of LiMn[sub 2]O[sub 4] as a Cathode in Secondary Lithium Cells, J. Electrochem. Soc. 138 (1991) 2859. doi:10.1149/1.2085330.

[48] R.E. Carter, Kinetic Model for Solid-State Reactions, J. Chem. Phys. 34 (1961) 2010–2015. doi:10.1063/1.1731812.

[49] C.F. Dickinson, G.R. Heal, Solid–liquid diffusion controlled rate equations, Thermochim. Acta. 340–341 (1999) 89–103. doi:10.1016/S0040-6031(99)00256-7.

[50] S. Yang, B. Yan, J. Wu, L. Lu, K. Zeng, Temperature-Dependent Lithium-Ion Diffusion and Activation Energy of Li1.2Co0.13Ni0.13Mn0.54O2Thin-Film Cathode at Nanoscale by Using Electrochemical Strain Microscopy, ACS Appl. Mater. Interfaces. 9 (2017) 13999–14005. doi:10.1021/acsami.6b16321.

[51] J. Li, R. Doig, J. Camardese, K. Plucknett, J.R. Dahn, Measurements of Interdiffusion Coefficients of Transition Metals in Layered Li-Ni-Mn-Co Oxide Core-Shell Materials during Sintering, Chem. Mater. 27 (2015) 7765–7773. doi:10.1021/acs.chemmater.5b03499.

[52] B.J. Wuensch, T. Vasilos, Diffusion of Transition Metal Ions in Single-Crystal MgO, J. Chem. Phys. 36 (1962) 2917. doi:10.1063/1.1732402.

[53] D.G. Wickham, SOLID-PHASE EQUILIBRIA IN THE SYSTEM NiO-Mn2O3-O2, J. Inorg. Nucl. Chem. 26 (1964) 1369–1377.

4: *In-Situ* Analysis of Nucleation and Growth of Transition Metal Oxalate Battery Precursor Particles via Time Evolution of Solution Composition and Particle Size Distribution

4.1. Overview

Precise control over particle composition and morphology is essential for the optimization of electroactive, multi-component transition metal oxides used as lithium-ion battery cathode materials. These transition metal oxides particles are often synthesized using precursors produced via coprecipitation reactions, in part due to the advantages provided by coprecipitation including scalability and homogeneous mixing of different transition metal ions. Understanding the kinetics of the nucleation and particle growth for each individual transition metal within a multicomponent blend solution is critical for rational and explicit control of particle composition, as well as to dictate the particle morphology. In this study, in-situ particle size distribution was measured during coprecipitation reactions using focused beam reflection. The transition metal concentrations were also in-situ tracked during the process which, in combination with the particle size information, provided detailed information on the reaction rate, reaction order, and mechanisms of particle nucleation and growth. This work is the first demonstration of application of such techniques to battery precursor particle synthesis, and provided insights into important observations during the coprecipitation process such as the change in the rate of coprecipitation of different transition metals when reacted in isolation or in a blend with other components. The techniques and analysis demonstrated in this paper could find application across other multicomponent transition metal coprecipitation systems important to many applications, including energy storage materials.

The element of this chapter has been published in the following journal:

Dong, H., Wang, A., Smart, G., Johnson, D., & Koenig Jr, G. M. (2018). *In-situ* analysis of nucleation and growth of transition metal oxalate battery precursor particles via time evolution of solution composition and particle size distribution. Colloids and Surfaces A: Physicochemical and Engineering Aspects, 558, 8-15.

4.2. Introduction

Lithium-ion (Li-ion) batteries have become a successful energy storage technology due to their high energy density and capability to meet a variety of power and energy requirements for a wide diversity of applications [1, 2]. The flexibility of Li-ion battery functionality results from the variety of battery active material options, and for the cathode particles comprised of multicomponent transition metal (TM) oxides are currently the most commonly used [3, 4]. To successfully design or choose a particular multicomponent TM oxide cathode material, careful control is needed over the chemical composition of the material because the material structure and electrochemical properties are highly sensitive to the TM composition, and even slight deviations in stoichiometry can significantly influence battery performance [5–9]. Coprecipitation is a popular route to synthesize the precursors used for TM oxide battery particles due to the homogeneous mixing of different TMs at the atomic level that is achieved with this method [5, 10, 11–19]. The obtained precursor materials are then converted to the final battery active materials via high temperature calcination processes. However, although achieving the appropriate TM composition and distribution during the initial coprecipitation synthesis process is critical for rational control over electrochemical properties of battery materials, little has been reported on the details of the coprecipitation solution chemistry using multiple TM cations. While often the TM composition of the precursor particles is assumed to reflect the stoichiometry of the dissolved TM feed to the process, under some solution conditions this assumption is not appropriate and can result in measurable deviations of the expected properties of the battery active material after calcination [5].

The technique was described in chapter 2 to track the TM composition as a function of time during the coprecipitation process, and the method was applied for pure precipitates containing one TM and multicomponent precipitates where each individual TM was tracked independently [5]. This technique used inductively coupled plasma optical emission spectroscopy (ICP-OES) to analyze the compositions of the solid and solution phase separately at multiple collection times during batch reactor coprecipitation. While this technique gives important insights into precipitate composition as a function of time, it cannot determine the normalized (by solid phase surface area) rate of TM precipitation onto the solid phase and cannot differentiate between particle nucleation and particle growth during the process because there was not information simultaneously collected on the particle size distribution (PSD). To obtain insights into these processes, the PSD must be collected in-situ during the coprecipitation process and combined with the compositional information. PSD measurements via image analysis (including both optical and electron microscopies) have been used in many crystallization phenomena studies [20–23]. While these methods have been successfully applied to many systems, it is challenging to image the particles directly in the batch reactor in-situ, and ex-situ observation has a lag time in transferring and/or preparing samples that will modify the solution chemistry relative to the simultaneously collected compositional information. Thus, a technique was needed to provide in-situ information during the coprecipitation process of the PSD with temporal resolution equal to or better than the compositional information. For the study described herein, the technique that was employed to obtain the in-situ PSD information was Focused Beam Reflectance Measurement (FBRM) [24–29]. FBRM operates using a probe that is directly inserted into the reaction solution. The probe has a laser which is focused in a focal plane beyond a sapphire window at the end of the cylindrical probe. The laser rotates at a high fixed speed and as the beam crosses over particles within the focal plane the focused laser beam intersects the edge of the particle and the laser light is backscattered. The backscattered light is transmitted back up the probe to the detector, and the backscattered signal continues until the beam has gone beyond the other side of the particle surface. Thus, the backscattered light is transmitted as it traverses the particle from edge to edge, and because the laser is scanned with a fixed speed, the edge-to-edge time scale is converted to a length scale which is known as chord length. The laser passes over many particles as it sweeps, and thus a chord length distribution (CLD) is obtained from the FBRM analysis. The PSD rather than the CLD is desired for the analysis in this study, and the CLD can be converted to a PSD using methods previously reported which will be discussed in further detail in the Experimental section [30]. The FBRM technique is fast and can produce large statistics on the particle populations as long as the number of particles in the suspension is sufficient.

In this study, we tracked the in-situ PSD of TM oxalate precipitates using FBRM, and combined this information with the precipitation rate of the TMs obtained from compositional analysis of the reaction solution as a function of time. With these combined techniques, the rate of precipitation normalized to the surface area of the precipitate was obtained. Such information is necessary to rationally control the synthesis of multicomponent TM precipitates, and this is the first report of applying such analysis to battery precursor particles. In addition, the in-situ tracking of the PSD during precipitation provided insights into the nucleation and growth processes these precipitate materials. The model system chosen was oxalate precipitation with pure and mixed solutions of manganese and nickel, an important system towards precursor synthesis for multiple battery active materials, such as $LiMn_{1.5}Ni_{0.5}O_4$, $LiMn_{10.5}Ni_{0.5}O_2$, and $LiNi_{1/3}Mn_{1/3}Co_{1/3}O_2$ [5, 31, 32]. In particular, a 3:1 Mn:Ni feed ratio was chosen because this precipitate stoichiometry is necessary for precursors used to form high purity $LiMn_{1.5}Ni_{0.5}O_4$, which is a promising high voltage cathode material [33, 34]. Oxalate precipitation was chosen because both nickel and manganese (and other TM of interest to battery precursors including cobalt) form stable oxalate dihydrate particles, whereas other popular battery precursor particle precipitate systems such as hydroxides or carbonates have the additional complexity of the simultaneous formation of multiple types of precipitates or the oxidation of the precipitate while still in solution [35, 36].

4.3. Experimental

4.3.1. Coprecipitation Synthesis

The coprecipitation synthesis was adapted from previous work, as detailed described in chapter 2 [5]. In brief, the TM solution and oxalate solution were prepared separately by dissolving laboratory grade $MnSO_4 \cdot H_2O$ and $NiSO_4 \cdot 6H_2O$ for the TM solution and $Na_2C_2O_4$ for the oxalate solution in deionized water (DI) heated to 60 °C (all reagents from Fisher). The two solutions were mixed by pouring the TM solution all at once into the oxalate solution. The concentrations of total TM ions, and oxalate, in the mixed solution were predetermined and were set at 20 mM at the initiation of all precipitation experiments. In the manganese and nickel blend coprecipitation, the TM solution contained manganese and nickel with 3:1 ratio, while the total TM concentration was still the same as oxalate. The fast pouring, as well as a magnetic stir bar spinning at 300 rpm, provided mixing to ensure a homogeneous solution. In addition to pre-heating to 60°C before mixing, during the reaction the temperature was kept at 60°C and the stir bar was maintained at

300 rpm. Syringes were used with syringe filters to collect the solute during periodic time intervals over the course of the reaction for compositional analysis. For solution compositional analysis, a sample (~2 mL) was withdrawn from the 1 L beaker reaction vessel using a 3 mL syringe. For the withdrawn sample, the aqueous phase was quickly separated from the solid precipitate particles by forcing the solution through a 33 mm diameter syringe filter with 0.22 mm pore size (Fisherbrand). The aqueous phase was further digested using aqua regia and diluted with DI water into a proper concentration for ICP-OES analysis (PerkinElmer Optima 8000), which was 0.1 to 10 ppm.

4.3.2. Characterization of Particle Size and Shape

During the coprecipitation reaction, a ParticleTrack G400 (Mettler Toledo) with FBRM capability was used for in-situ determination of the PSD throughout the coprecipitation reaction by immersing the FBRM probe directly into the reaction environment. The probe was inserted into the solution such that the laser window was located roughly at the center of the beaker reactor. The CLD averaged over a 10 second interval was collected throughout an experiment until negligible changes in either particle counts or CLD was observed. At the conclusion of one hour of the coprecipitation reaction proceeding, the particle shapes and sizes were also characterized using a scanning electron microscope (SEM, FEI Quanta 650) after filtering and complete drying. Thermal gravimetric analysis (TGA, TA Q50) was performed to determine the water stoichiometry of the precipitates. TGA analysis for all the precipitate particles synthesized for this study confirmed two structural water for each transition metal oxalate unit (e.g., dihydrates).

4.3.3. Conversion from CLD to PSD and Normalization of Reaction Rates

In the conversion from the directly measured CLD with the FBRM to a PSD, an essential assumption was made that the number of particles analyzed was large enough that the probability of measuring a chord within a particular size range was equated to the fraction of the total number of particles which would be measured as having the chord length within this size range. It is expected that the number of particles recorded by the FBRM was high enough that this assumption was valid [30]. The conversion from CLD to PSD was completed using the method described by Pandit at al. [30]. First, an initial guess was made for the mean and the variance of a normal distribution function that expressed a PSD. The number of independent normal distributions used in the fitting were dependent on the number of independent peaks in the CLD that were observed for each scan (e.g.; 1 normal distribution was fit for a single peak while 3 normal distributions were used for 3 peaks). Next, the discrete PSD was formed using the guessed normal distribution and converted to a discrete CLD with bin sizes the same as those of the CLD data. The two parameters for each normal distribution were adjusted using the least squares method to minimize the difference between the CLD from the FBRM experimental measurements and the calculated CLD using the fitted PSDs. The R2 values for the calculated compared to the measured CLDs were no less than 0.97, indicating good fits of the measured CLDs using the PSD parameters.

4.4. Results and Discussion

Measuring the concentrations of the TM remaining in solution at different time points during the coprecipitation was necessary to determine the reaction rates associated with the formation of the particle precipitates. The TM concentrations remaining in solution was determined during the precipitation with initial TM feeds of pure nickel, pure manganese, and a "blend" system (with the TM feed ratio being 3:1 Mn:Ni). The results for the three systems are in shown in Fig.1. The pure manganese oxalate ($MnC_2O_4\cdot 2H_2O$, referred to as MnO_x) coprecipitation proceeds quickly over the first ten minutes and plateaus after roughly 20 minutes. On the contrary, the pure nickel oxalate ($NiC_2O_4\cdot 2H_2O$, referred to as NiO_x) coprecipitation consumes the TM ion at a lower initial rate, and the residual Ni solution concentration does not reach a plateau until after an hour. In the blend system (Mn:Ni feed ratio 3:1, with the precipitate concentration slightly changing with reaction time and reaching $Mn_{0.72}$ $Ni_{0.28}C_2O_4\cdot 2H_2O$ at the one hour collection time, referred to as $Mn_3Ni_1O_x$), the reaction proceeds in a manner qualitatively more similar to the pure manganese reaction, and this system will be discussed in further detail later.

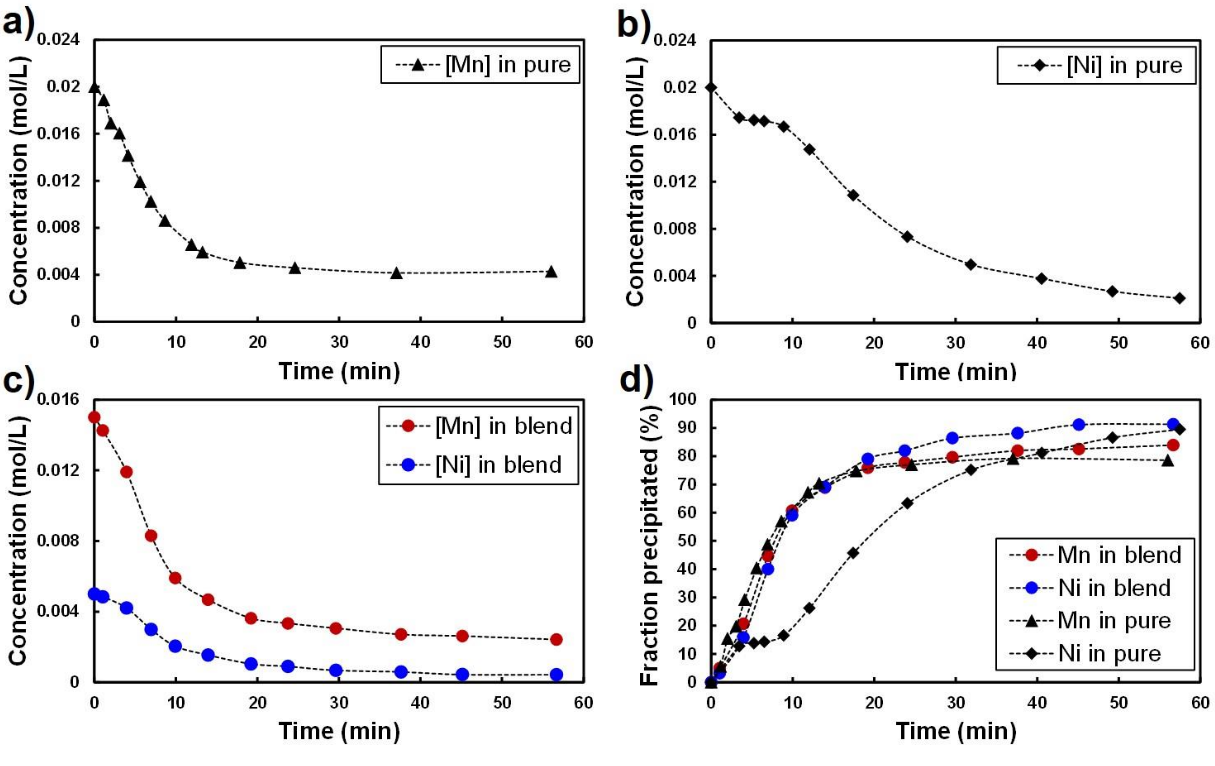

Figure 1. Residual soluble (a) Mn (triangles) and (b) Ni (diamonds) in solution during coprecipitation of pure manganese oxalate and pure nickel oxalate. (c) Residual soluble Mn (blue circles) and Ni (red circles) during coprecipitation of feed with 3:1 Mn:Ni ratio. The total

concentrations of TM and oxalate at the beginning of the coprecipitation for all solutions were 20 mM. (d) Fraction of Mn and Ni ions in precipitate phase. Dashed lines added to guide the eye.

Fig. 2 shows the total chord counts from the FBRM probe as a function of the time after initiating the coprecipitation for the NiO_x, MnO_x, and the $Mn_3Ni_1O_x$ reaction systems. A linear relationship has previously been reported between the particle density and FBRM particle count for suspensions that contain particles of similar and larger sizes than the particles in this study [27]. This linear relationship has been reported to hold until the FBRM particle count reaches as high as 10,000. The inset in Fig. 2 is the enlarged view of the first 10 minutes of the reaction. From this enlarged view it can be found that particles begin to form after around 1 minute for the pure manganese system, 4.5 minutes for the pure nickel system, and 1.5 minutes for the blend system. Note that the limit of detection for the FBRM is 0.5 um, thus this onset is the point where particles of at least this size were measured in the solution. These onset times were consistent with rough observations of the induction times, with the induction time being the time for the initial clear solutions to become cloudy to the naked eye. From the dissolved TM concentration vs. time plots (Fig. 1) it was observed that NiO_x coprecipitation had a relatively slower transition period for Ni going to the particle phase after the solutions were mixed. The time lag observed for detecting particles with the FBRM, slower detected loss of Ni from the solution phase, and longer induction times observed implied that NiO_x crystallization from the solution has a slower nucleation rate. After the increase in FBRM particle counts at ~4.5 minutes for the NiO_x system the particle counts continuously increased out to even 50 minutes after the solutions were mixed. Even though the particle counts passed the 10000 upper limits to meet the linear relationship between the count and particle density after 10 minutes, the increase in particle counts still reflected the continuous particle growth in the solution. In contrast, MnO_x and $Mn_3Ni_1O_x$ systems have their FBRM counts plateau much more quickly, after 3 minutes and 10 minutes respectively. Continuous particle formation rather than particle growth by solute depositing on existing particles may explain the lower rate of loss of the soluble Ni species in the NiO_x reaction even after the induction period. The pure Mn precipitation; however, had relatively rapid particle formation (marked by the short period of increase in FBRM counts and stable plateau in Fig. 1) followed closely by particle growth. Particle growth has previously been reported to be a lower energy barrier relative to nucleation [37], and thus this interpretation was consistent with the faster consumption of soluble Mn during MnO_x precipitation. For the $Mn_3Ni_1O_x$ coprecipitation system, there was relatively fast particle formation and a plateau in the FBRM counts similar to the observations for MnO_x system, although the timescale for a plateau in the counts was longer than for MnO_x system. We suspect the longer time to reach a plateau in particle counts for the $Mn_3Ni_1O_x$ system was due to the continuous formation of NiO_x crystals, as supported by the FBRM data (Fig. 2). In our earlier work [5], we also observed an increased reaction rate of nickel ions to the precipitate phase in the blend system. It was speculated that the fast crystallization of the MnO_x particles provided seeds for the nickel ions to deposit onto and thus to grow faster. Previous literature on nucleation and particle growth has reported the precipitation rate to be a linear function of the suspension density for several inorganic salts [29]. While suspension density and particle seeding heavily influence precipitation rate during the early nucleation stage, other factors including surface roughness have a great effect on precipitation rate during the later particle growth stage. The potential influence of surface roughness will be described in further detail for the oxalate particles later in the discussion.

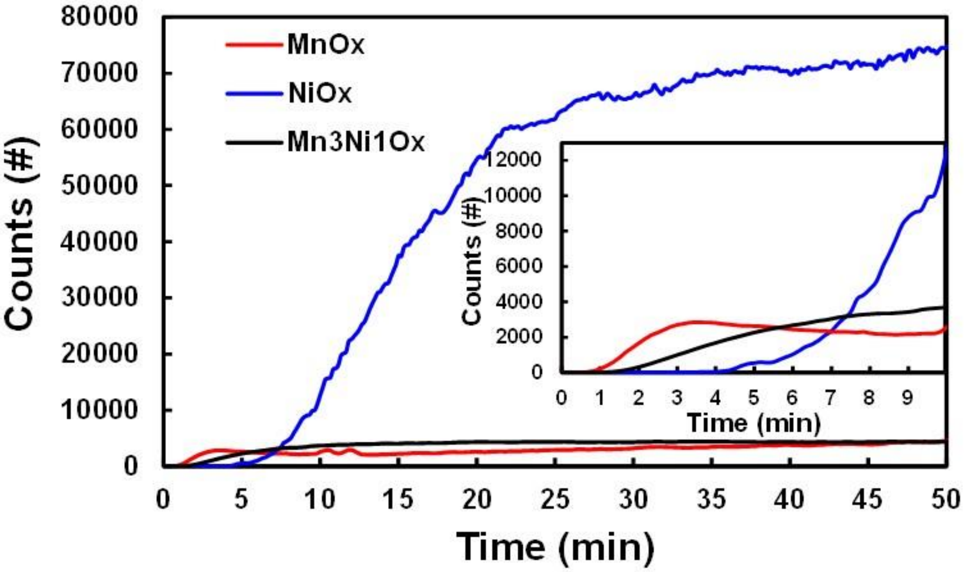

Figure 2. FBRM total counts as a function of reaction time for pure nickel oxalate (NiO_x, blue), pure manganese oxalate (MnO_x, red), and manganese nickel blend oxalate ($Mn_3Ni_1O_x$, black) coprecipitation. Inset is an expanded view of the first 10 minutes.

The 10-second averaged CLD as a function of reaction time for all three systems were obtained using the FBRM probe and converted to PSDs using the method described in the Experimental section. It is noted that the CLD was not square weighted such that information could be extracted at earlier times when only smaller particles were formed. The resulting PSDs from the FBRM measurements at 5, 10, and 30 minutes after the start of the coprecipitation reactions for each of the three systems are shown in Fig. 3. For the two faster precipitating systems, MnO_x and Mn3Ni1Ox, a distribution before 5 minutes is also shown to highlight the initial formation of small particles (due to the slower coprecipitation of the pure NiO_x, a PSD before 5 minutes was not collectable). The earliest PSD times were chosen as the earliest time where the CLD plot had clear peaks. From the PSD plots at different time points it is clear that following the initial formation of crystals, which was indicated by the very sharp peaks in the size range smaller than 10 um, the nucleated particles continued to grow. Especially for the MnO_x and $Mn_3Ni_1O_x$ particles, significant shifting of the peak positions was observed until 30 minutes after the coprecipitation was initiated. After 30 minutes the CLDs, and correspondingly the calculated PSDs, changed very little. Fig. 4 shows the SEM images of the particles collected from the three different coprecipitation systems after an hour of mixing, which was after the TM solution concentrations and FBRM counts had stabilized for all three systems (Fig. 1 and 2). The pure manganese particles and the blend particles both had a platelet morphology (Fig. 4a, c). We speculate that the two lengths associated with the plate morphology – the short plate thickness and larger plate length/width associated with the larger flat surface, resulted in the two peaks in the PSDs observed for these systems. The pure Ni system did not produce plate shape particles but also had two peaks in the PSD, however, in this case the second larger PSD peak was attributed to particle aggregates in the NiO_x system. The NiO_x particles were observed to have highly aggregated clumps in the SEM (Fig. 4b), and even though SEM sample preparation may have influenced the aggregation process the size of these aggregates were consistent with the PSD observations. From the SEM images, surface roughness can be clearly observed on the pure manganese and the blend precipitate particles whereas the surface of the NiO_x particles were relatively smooth. This observation of the smooth NiO_x particles provides one possibility to explain the preference of the nickel solute to continue nucleating rather than depositing on the crystal surface. In the NiO_x precipitate system the energy barrier of two-dimensional crystal growth on a perfect surface would be much larger than that from a defect or higher surface area substrate, and additional nucleation of NiO_x particles may instead be preferred. The conclusion of the nucleation stage in the blend system likely reflects the reduced driving force towards nucleation due to the decreasing Ni2+ concentration, combined with the surface roughness of the blend particles promoting precipitation through particle growth. The particle surface roughness, which favors particle growth over nucleation, decreased the distance between sites of growth on the particles, analogous to the critical distance between dislocation sites in 2-D particle nucleation and growth studies needing to be greater than the critical particle size to facilitate the nucleation over growth [38].

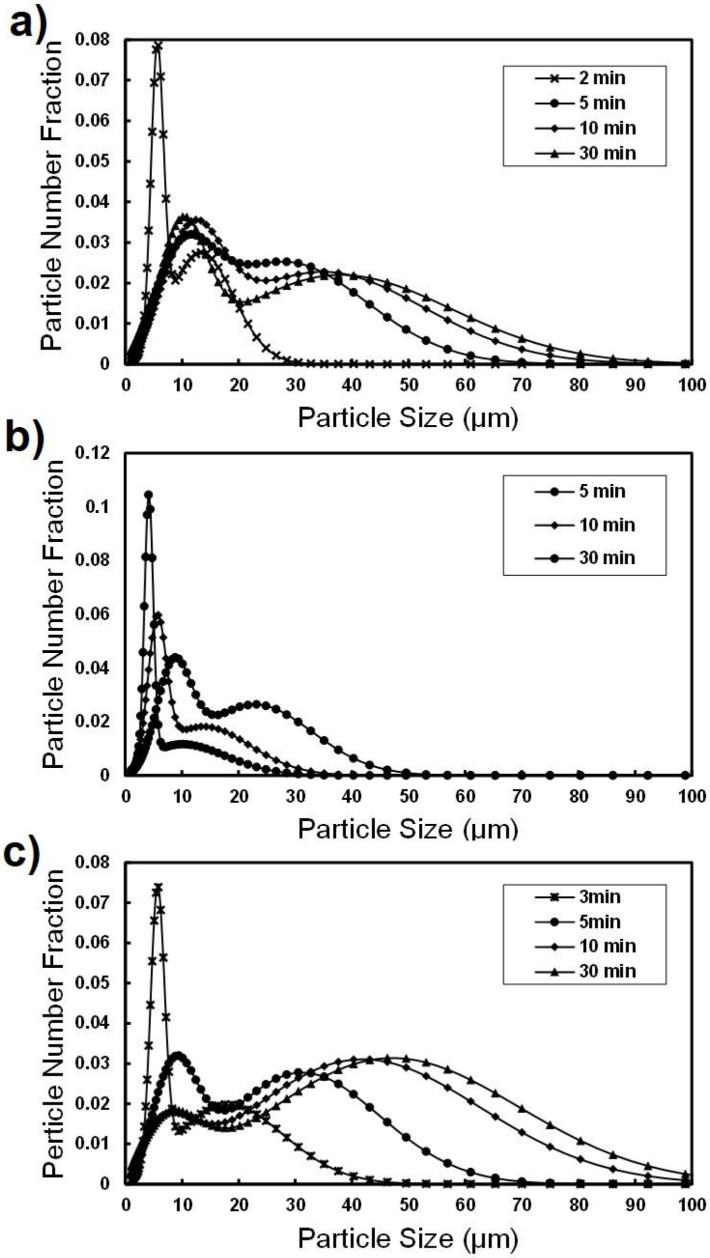

Figure 3. Particle size distributions at 5, 10, and 30 minutes after the start of the precipitation in a) pure manganese oxalate (MnO$_x$), b) pure nickel oxalate (NiO$_x$), and c) manganese nickel blend oxalate (Mn$_3$Ni$_1$O$_x$). For a) and c), an earlier distribution is shown to highlight the initial formation of smaller particles in these faster precipitating systems. Solid lines added to guide the eye.

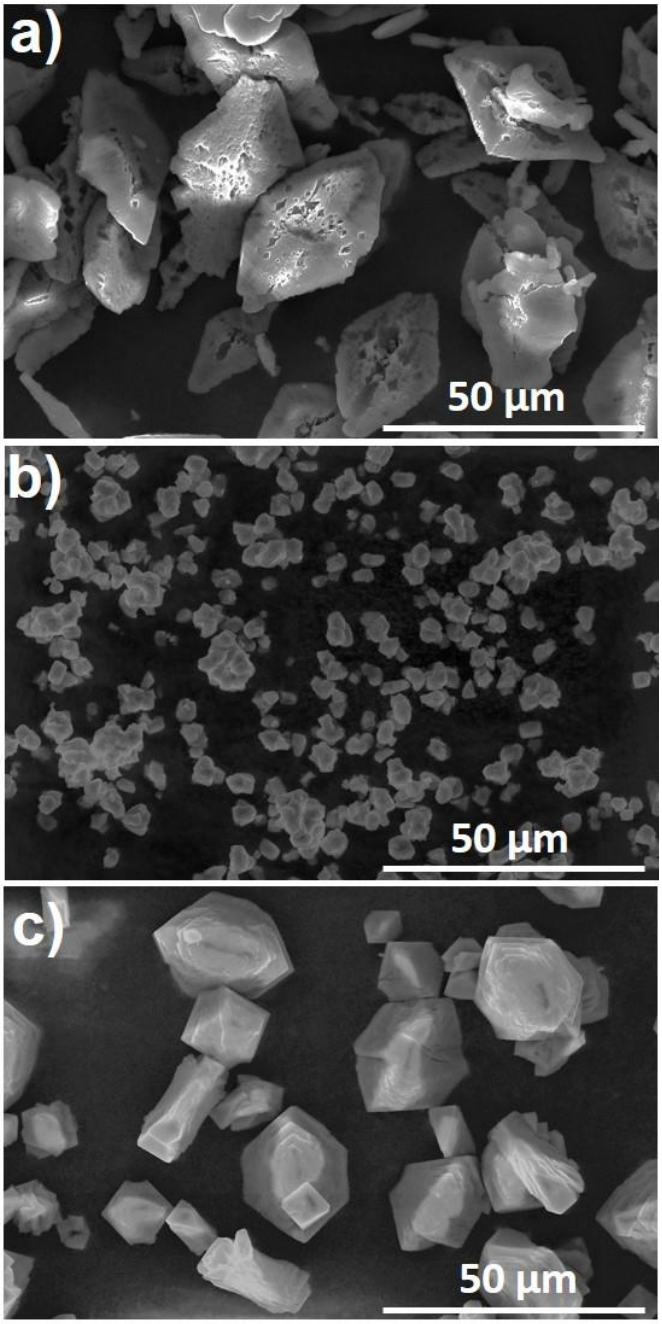

Figure 4. SEM images of a) MnO_x particles, b) NiO_x particles, and c) $Mn_3Ni_1O_x$ particles (from the 3:1 Mn:Ni blend feed coprecipitation reaction) collected after an hour of precipitating.

The nucleation and particle growth mechanisms can also be deduced by studying the evolution of PSDs, as described by Eberl *et al.* [27]. In many crystallization processes, the crystallite PSD has been observed to follow a lognormal distribution, which can be explained by the Law of Proportionate Effect (LPE): $X_{j+1} = X_j + \epsilon_j X_j$, stating that a particle's growth rate is determined by its size (X) plus the proportionality constant (ϵ) [207]. X_j is the particle size in an early time point and X_{j+1} is the particle size after an defined interval of particle growth. The proportionality constant is dependent on many system parameters, such as temperature and concentration. The lognormal distribution cannot fit well to the PSDs in the systems in this study due to either the particle size difference in different orientations (the platelet MnO_x and $Mn_3Ni_1O_x$ particles) or the segregation of tiny particles (NiO_x particles). Thus, a fit with 2 log-normal distributions was used representing each of the PSD peaks. The obtained CLD data was also analyzed using the lognormal mean ($\alpha = \sum \ln(x) f(x)$) and variance ($\beta^2 = \sum [\ln(x) - \alpha]^2 f(x)$), and the results were compatible with applying the approach of Eberl at al. In that study, it was proposed that in addition to considering the entire shape of the PSD, growth mechanisms can be extracted from the evolution of β^2 with respect to α for a series of sample sets. In Fig. 5, β^2 are plotted on the y-axis with respect to α on the x-axis. Since α scaled with particle size, smaller α values correspond to earlier time points in the precipitation and increasing α values correlate with later times for all the precipitation systems. As shown in Fig. 5, at smaller values of α (earlier times in the reaction) β^2 had a linear dependence on α for the pure manganese which indicated a surface-controlled growth, whereas for the pure nickel precipitation β^2 had an exponential dependence on α indicating a continuous nucleation and growth mechanism [27]. The slope of the curve for NiO_x in early stages of the coprecipitation was very gentle, indicating that the new particle nucleation occurred simultaneously during the growth of existing particles, but at a slow rate. The β^2 value dropped sharply after 30 minutes in NiOx coprecipitation, which could be due to Ostwald ripening where the smaller particles dissolved while the larger particles grow larger [27]. In contrast, the variance for the MnO_x precipitates remained almost constant in the later stages (after 30 minutes) of the reaction, which followed well the pattern of a supply-controlled growth mechanism [39]. The variance of the PSD in Mn3Ni1Ox reaction also increased linearly with the lognormal mean and the slope was identical with that of the pure manganese precipitation. The intercepts of the lines, however, were different, which was due to the different initial PSDs before the growth phase was initiated. The nucleation reaction in MnO_x coprecipitation ceased after the very short induction period and rendered the initial particles within a narrow size range, while in the blend precipitation the continuous nucleation of particles induced an asymptotic initial distribution to start with. It can be seen from Fig. 5 that the initial starting point of the blend system was between measured values of the pure MnO_x and NiO_x precipitations. Other than the initial PSDs, the blend precipitation exhibited the same pattern and thus followed the same surface-controlled growth mechanism as the MnO_x. This behavior was also consistent with the similar consumed ion fractions and rates (Fig. 1, d) for the MnO_x and Mn3Ni1Ox systems. We speculate that the rough crystal surface lowered the energy barrier of nickel ions to deposit and grow on the crystal surface during the $Mn_3Ni_1O_x$ coprecipitations and thus facilitated the precipitation of nickel ions in the blend system. At later times, the blend precipitation had a reduction in the rate of increase of β^2, which may have been due to both the ripening and supply-controlled growth mechanisms playing a role.

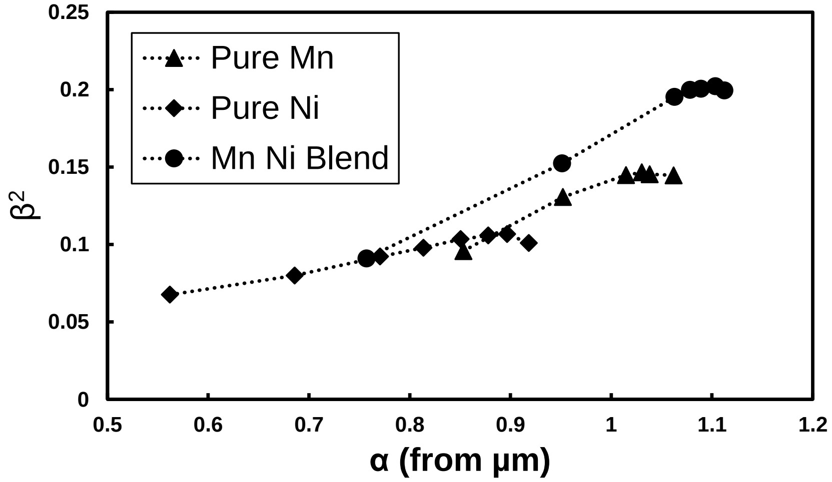

Figure 5. The lognormal variation β^2 vs. lognormal mean α of the experimentally measured chord length distributions for the pure manganese precipitate (MnO_x, triangles), pure nickel precipitate (NiO_x, diamonds), and the blend precipitate ($Mn_3Ni_1O_x$, circles). Dashed lines added to guide the eye.

Using the measured concentrations of the TMs for the three systems (Fig. 1), the rate of the coprecipitation reaction was determined for each TM by numerically calculating the change in concentration divided by the change in time at each time point. The rate of the coprecipitation reaction was also normalized by the total surface area of particles that was available at that time for the TMs to deposit onto, and the particle surface was determined from the PSDs extracted from the FBRM measurements with the assumption that the particle sizes in the PSDs corresponded to spherical particles. Fig. 5 displays the logarithm of the TM coprecipitation rate plotted against the total TM concentration (or equivalently total oxalate, since the feed had the same concentration of both and the TM and oxalate precipitated at a 1:1 ratio). Starting with a rate expression of the form: $r = k[M]^{\delta}[Ox]^{\Theta}$, because the total TM and oxalate concentration were always equal in all three systems, the formula was simplified to $r = k[M]^{\gamma}$, of which the logarithm of both sides resulted in $\log r = \log k + \gamma \log[M]$. A plot of log r as a function of log [M] thus had a slope which corresponded to the reaction order, and this plot for the three coprecipitation systems can be found in Fig. 6. As proposed by Doremus *et al.*, there are two mechanisms of surface-controlled particle growth from ionic solute, either the ions form a molecule which is then adsorbed by the kinks of the particle surface ("molecule" mechanism) or the ions get adsorbed to the correct sites on the surface directly from the solution ("direct adsorption" mechanism) [40]. For the one-to-one electrolyte as was the case for the TM oxalate coprecipitation in this study, the reaction rate would exhibit an order of three for the molecule mechanism and two for the direct adsorption mechanism. From linear fitting of the data from Fig. 6, the MnO_x had a reaction order of 2.0, which fit well with the direct adsorption model. The NiO_x precipitation, however, has a reaction order of 1.6. This deviation of reaction order below 2.0 may have been due to the simultaneous occurrence of both nucleation and particle growth during the NiO_x reaction, which consumed the solute in a relatively slower rate. The TM ion precipitation rate in the Mn3Ni1Ox system aligned well with the MnO_x in the high concentration regime and with the NiO_x in the low concentration regime. This result implies that the blend coprecipitation followed the same surface-controlled particle growth mechanism as in the MnO_x in the early reaction period when the solute was adequate, and that it switched to the kinetics of NiO_x precipitation as the reaction proceeded and less solute was residual in the solution. The two points that are getting closer to the pure nickel precipitation mechanism corresponded to the reaction after 12 minutes of mixing after the Mn^{2+} consumption almost plateaued and Ni^{2+} nickel was still significantly participating in the reaction. The decrease of critical particle size under the low supersaturation condition made the particle growth even on the rough particle surface more difficult and some of the precipitating Ni^{2+} may have switched back to the continuous nucleation mechanism [40]. This hypothesis of new particles nucleating in the Mn3Ni1Ox precipitation at later reaction times was supported by the slight increase of the small particle fraction in the PSDs (Fig. 2).

The growth mechanisms during precipitation of TM ions from pure and blend TM solutions provides fundamental knowledge necessary for rational battery material design and control, in the case where precipitate precursors are used for the production of battery active materials. Ideally, multicomponent precipitates would have controllable composition and particle size throughout a precipitation reaction process. Such control is important because of the sensitivity of the final materials processed using the TM precipitates with regards to composition and particle size on final material and electrochemical properties [5, 41]. This study’s main focus was the nucleation and particle growth processes for TM precipitates, and in particular it was found that properties such as crystal size and surface roughness interacted with the precipitation rate. The detailed nucleation and growth processes also influence final material composition in multicomponent systems, including both the total composition and the distribution of TMs within the particles. A systematic study on the external factors that influence the nucleation and particle growth process, such as feed concentration and solution temperature will be needed to provide a more complete understanding of the nucleation and growth processes of the particles [18].

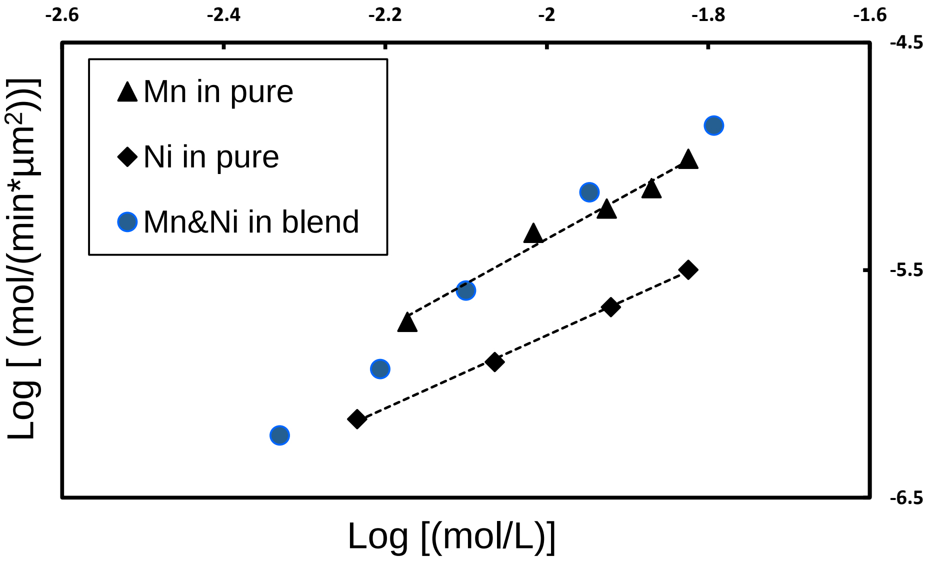

Figure 6. Logarithms of the reaction rates as a function of the logarithms of the residual TM concentrations. Concentrations were for total TM, which was equivalent to oxalate concentrations in all experiments. Dashed lines represent from linear fits.

4.5. Conclusion

In this work, in-situ FBRM measurements converted to PSDs were combined with ICP-OES measurements of solution compositional changes in-situ to track the reaction process as a function of time. Such information is necessary to understand the detailed nucleation and growth processes occurring in the solution, as well as to normalize the reaction rates for the coprecipitation. The FBRM provided insights into the timescales of particle nucleation and growth for variations in transition metal composition during oxalate coprecipitation. By comparison of the observations for pure nickel and manganese coprecipitation in comparison with coprecipitation of a blend of these transition metals, insights were gained into the mechanism by which nickel was consumed in a higher rate in a precipitation with a blend of Mn as opposed to precipitation in the absence of manganese ions. The experimental results demonstrated that the pure manganese and pure nickel precipitations followed different nucleation and particle growth paths. In the pure manganese oxalate precipitation, the nucleation ceases when the particle growth starts, which resulted in the solute being consumed at a faster rate. However, in the pure nickel oxalate precipitation, particle nucleation continues concurrent with the slower particle growth process, which resulted in a relatively slower observed reaction rate. In the blend system of manganese and nickel, the rough surface helped to facilitate fast deposition of both transition metal ions on the surface; furthermore, manganese and nickel ions both followed an efficient surface-controlled direct adsorbing mechanism of precipitation. These observations explained why in the blend system both transition metal ions were consumed quickly and in a similar ratio, which resulted in a homogeneous blend precipitate, which would be desirable from a battery precursor synthesis standpoint. This study demonstrates the importance of understanding the nucleation and growth processes of precipitate particles when being used as precursors for multicomponent transition metal functional materials such as metal oxides. The different nucleation and growth mechanisms influence the composition of the final precipitates, the size and size distribution of the collected particles, and the timescale of the precipitation process. All of these outcomes are very important to resulting material properties and for rational predictive design of particulate reactors for making these materials.

4.6. Reference

[1] J.B. Goodenough, K.-S.S. Park, The Li-Ion Rechargeable Battery: A Perspective, J. Am. Chem. Soc. 135 (2013) 1167–1176. doi:10.1021/ja3091438.

[2] N. Nitta, F. Wu, J.T. Lee, G. Yushin, Li-ion battery materials: Present and future, Mater. Today. 18 (2015) 252–264. doi:10.1016/j.mattod.2014.10.040.

[3] J.M. Tarascon, M. Armand, Issues and challenges facing rechargeable lithium batteries, Nature. 414 (2001) 359–367. doi:10.1038/35104644.

[4] E. Vinodkumar, R. Marom, R. Elazari, G. Salitra, D. Aurbach, Challenges in the development of advanced Li-ion batteries: a review, Energy Environ. Sci. 4 (2011) 3243–3262. doi:10.1039/c1ee01598b.

[5] H. Dong, G.M. Koenig Jr, Compositional control of precipitate precursors for lithium-ion battery active materials: role of solution equilibrium and precipitation rate, J. Mater. Chem. A. 5 (2017) 13785–13798. doi:10.1039/C7TA03653A.

[6] M.M. Thackeray, S.-H. Kang, C.S. Johnson, J.T. Vaughey, R. Benedek, S.A. Hackney, Li2MnO3-stabilized LiMO2 (M = Mn, Ni, Co) electrodes for lithium-ion batteries, J. Mater. Chem. 17 (2007) 3112–3125. doi:10.1039/B702425H.

[7] C.S. Johnson, N. Li, C. Lefief, J.T. Vaughey, M.M. Thackeray, Synthesis, Characterization and Electrochemistry of Lithium Battery Electrodes: xLi2MnO3·(1 − x)LiMn0.333Ni0.333Co0.333O2 (0 ≤ x ≤ 0.7), Chem. Mater. 20 (2008) 6095–6106. doi:10.1021/cm801245r.

[8] L. Wan, Y. Deng, C. Yang, H. Xu, X. Qin, G. Chen, Ni/Mn ratio and morphology-dependent crystallographic facet structure and electrochemical properties of the high-voltage spinel LiNi0.5Mn1.5O4 cathode material, RSC Adv. 5 (2015) 25988–25997. doi:10.1039/C5RA03602J.

[9] H. Duncan, B. Hai, M. Leskes, C.P. Grey, G. Chen, Relationships between Mn 3+ Content, Structural Ordering, Phase Transformation, and Kinetic Properties in LiNi x Mn 2– x O 4 Cathode Materials, Chem. Mater. 26 (2014) 5374–5382. doi:10.1021/cm502607v.

[10] K.R. Chemelewski, D.W. Shin, W. Li, A. Manthiram, Octahedral and truncated high-voltage spinel cathodes: the role of morphology and surface planes in electrochemical properties, J. Mater. Chem. A. 1 (2013) 3347. doi:10.1039/c3ta00682d.

[11] H. Dong, A. Wang, G.M. Koenig, Role of coprecipitation and calcination of precursors on phase homogeneity and electrochemical properties of battery active materials, Powder Technol. 335 (2018). doi:10.1016/j.powtec.2018.05.020.

[12] D. Wang, I. Belharouak, L.H. Ortega, X. Zhang, R. Xu, D. Zhou, G. Zhou, K. Amine, Synthesis of high capacity cathodes for lithium-ion batteries by morphology-tailored hydroxide co-precipitation, J. Power Sources. 274 (2015) 451–457. doi:10.1016/j.jpowsour.2014.10.016.

[13] L. Li, X. Zhang, R. Chen, T. Zhao, J. Lu, F. Wu, K. Amine, Synthesis and electrochemical performance of cathode material Li1.2Co0.13Ni0.13Mn0.54O2 from spent lithium-ion batteries, J. Power Sources. 249 (2014) 28–34. doi:10.1016/j.jpowsour.2013.10.092.

[14] L. Yang, G. Xi, Preparation and Electrochemical Performance of LiNi1/3Co1/3Mn1/3O2 Cathode Materials for Lithium-ion Batteries from Spent Mixed Alkaline Batteries, J. Electron. Mater. 45 (2015) 301–306. doi:10.1007/s11664-015-4067-z.

[15] H. Liu, L. Tan, High rate performance of novel cathode material Li1.33Ni1/3Co1/3Mn1/3O2 for lithium ion batteries, Mater. Chem. Phys. 129 (2011) 729–732. doi:10.1016/j.matchemphys.2011.04.031.

[16] X. Zhang, F. Cheng, K. Zhang, Y. Liang, S. Yang, J. Liang, J. Chen, Facile polymer-assisted synthesis of LiNi0.5Mn1.5O4 with a hierarchical micro–nano structure and high rate capability, RSC Adv. 2 (2012) 5669. doi:10.1039/c2ra20669b.

[17] S. Wu, C.W. Yang, Preparation of LiNi0.8Co0.2O2-based cathode materials for lithium batteries by a co-precipitation method, J. Power Sources. 146 (2005) 270–274. doi:10.1016/j.jpowsour.2005.03.027.

[18] P. Axmann, G. Gabrielli, M. Wohlfahrt-Mehrens, Tailoring high-voltage and high-performance LiNi0.5Mn1.5O4 cathode material for high energy lithium-ion batteries, J. Power Sources. 301 (2016) 151–159. doi:10.1016/j.jpowsour.2015.10.010.

[19] J.P. Robinson, G.M. Koenig, Tuning solution chemistry for morphology control of lithium-ion battery precursor particles, Powder Technol. 284 (2015) 225–230. doi:10.1016/j.powtec.2015.06.070.

[20] D. Sarkar, X.-T. Doan, Z. Ying, R. Srinivasan, In situ particle size estimation for crystallization processes by multivariate image analysis, Chem. Eng. Sci. 64 (2009) 9–19. doi:10.1016/J.CES.2008.09.007.

[21] J. Eggers, M. Kempkes, M. Mazzotti, Measurement of size and shape distributions of particles through image analysis, Chem. Eng. Sci. 63 (2008) 5513–5521. doi:10.1016/J.CES.2008.08.007.

[22] B. Presles, J. Debayle, G. Fevotte, J.-C. Pinoli, Novel image analysis method for <italic>in situ</italic> monitoring the particle size distribution of batch crystallization processes, J. Electron. Imaging. 19 (2010) 031207. doi:10.1117/1.3462800.

[23] J. Calderon De Anda, X.Z. Wang, X. Lai, K.J. Roberts, Classifying organic crystals via in-process image analysis and the use of monitoring charts to follow polymorphic and morphological changes, J. Process Control. 15 (2005) 785–797. doi:10.1016/J.JPROCONT.2005.02.002.

[24] S.-Y. Yoon, Y. Deng, Flocculation and reflocculation of clay suspension by different polymer systems under turbulent conditions, J. Colloid Interface Sci. 278 (2004) 139–145. doi:10.1016/J.JCIS.2004.05.011.

[25] J.C. Alfano, P.W. Carter, A.J. Dunham, M.J. Nowak, K.R. Tubergen, Polyelectrolyte-Induced Aggregation of Microcrystalline Cellulose: Reversibility and Shear Effects, J. Colloid Interface Sci. 223 (2000) 244–254. doi:10.1006/JCIS.1999.6651.

[26] P. Raj, W. Batchelor, A. Blanco, E. de la Fuente, C. Negro, G. Garnier, Effect of polyelectrolyte morphology and adsorption on the mechanism of nanocellulose flocculation, J. Colloid Interface Sci. 481 (2016) 158–167. doi:10.1016/j.jcis.2016.07.048.

[27] N. Doki, H. Seki, K. Takano, H. Asatani, M. Yokota, N. Kubota, Process control of seeded batch cooling crystallization of the metastable α-form glycine using an in-situ ATR-FTIR spectrometer and an in-situ FBRM particle counter, Cryst. Growth Des. 4 (2004) 949–953. doi:10.1021/cg030070s.

[28] Z.Q. Yu, P.S. Chow, R.B.H. Tan, Interpretation of focused beam reflectance measurement (FBRM) data via simulated crystallization, Org. Process Res. Dev. 12 (2008) 646–654. doi:10.1021/op800063n.

[29] B. De Clercq, P.A. Lant, P.A. Vanrolleghem, Focused beam reflectance technique for in situ particle sizing in wastewater treatment settling tanks, J. Chem. Technol. Biotechnol. 79 (2004) 610–618. doi:10.1002/jctb.1028.

[30] A. V. Pandit, V.R. Vivek, Chord Length Distribution to Particle Size Distribution, AIChE J. 62 (2016) 4215–4228. doi:10.1002/aic.

[31] E. Zhao, M. Chen, D. Chen, X. Xiao, Z. Hu, A Versatile Coating Strategy to Highly Improve the Electrochemical Properties of Layered Oxide LiMO2(M = Ni0.5Mn0.5and Ni1/3Mn1/3Co1/3), ACS Appl. Mater. Interfaces. 7 (2015) 27096–27105. doi:10.1021/acsami.5b08777.

[32] F. Wu, H. Lu, Y. Su, N. Li, L. Bao, S. Chen, Preparation and electrochemical performance of Li-rich layered cathode material, Li[Ni0.2Li0.2Mn0.6]O2, for lithium-ion batteries, J. Appl. Electrochem. 40 (2010) 783–789. doi:10.1007/s10800-009-0057-2.

[33] A. Manthiram, K. Chemelewski, E.-S. Lee, A perspective on the high-voltage LiMn1.5Ni0.5O4 spinel cathode for lithium-ion batteries, Energy Environ. Sci. 7 (2014) 1339. doi:10.1039/c3ee42981d.

[34] R. Marom, S.F. Amalraj, N. Leifer, D. Jacob, D. Aurbach, A review of advanced and practical lithium battery materials, J. Mater. Chem. 21 (2011) 9938–9954. doi:10.1039/C0JM04225K.

[35] D. Wang, I. Belharouak, G.M. Koenig, G. Zhou, K. Amine, Growth mechanism of Ni0.3Mn0.7CO3 precursor for high capacity Li-ion battery cathodes, J. Mater. Chem. 21 (2011) 9290. doi:10.1039/c1jm11077b.

[36] Y.Y. Yang, S. Xu, M. Xie, Y. He, G. Huang, Y.Y. Yang, Growth mechanisms for spherical mixed hydroxide agglomerates prepared by co-precipitation method: A case of Ni1/3Co1/3Mn1/3(OH)2, J. Alloys Compd. 619 (2015) 846–853. doi:10.1016/j.jallcom.2014.08.152.

[37] M. Aoun, E. Plasari, R. David, J. Villermaux, A simultaneous determination of nucleation and growth rates from batch spontaneous precipitation, Chem. Eng. Sci. 54 (1999) 1161–1180. doi:10.1016/S0009-2509(98)00488-6.

[38] J.A. Dirksen, T. a. Ring, Fundamentals of crystallization: Kinetic effects on particle size distributions and morphology, Chem. Eng. Sci. 46 (1991) 2389–2427. doi:10.1016/0009-2509(91)80035-W.

[39] D.D. Eberl, V.A. Drits, J. Środoń, Deducing growth mechanisms for minerals from the shapes of crystal size distributions, Am. J. Sci. 298 (1998) 499–533. doi:10.2475/ajs.298.6.499.

[40] R. Doremus, Precipitation kinetics of ionic salts from solution, J. Phys. Chem. 2158 (1968). doi:10.1021/j150567a011.

[41] Y. Xue, Z. Wang, L. Zheng, F. Yu, B. Liu, Y. Zhang, K. Ke, Investigation on preparation and performance of spinel LiNi0.5Mn1.5O4 with different microstructures for lithium-ion batteries, Sci. Rep. 5 (2015) 13299. doi:10.1038/srep13299

5: Apparent Activation Energy of Multicomponent Transition Metal Oxalates to Probe Synthesis of Battery Precursor Materials

5.1. Overview

In this study the apparent activation energy of pure and multicomponent transition metal oxalate coprecipitation reactions were experimentally measured via time dependent extinction of light passing through the reaction solution. These measurements provide a quantitative descriptor of the influence of the relative transition metal composition on the nucleation and growth processes of these precipitates. The resulting crystal structures of the synthesized precursors were also determined and put into the context of the measured coprecipitation apparent activation energies, revealing that the apparent activation energy may indicate impurity or secondary phase formation before it is detectable with x-ray diffraction. This paper is the first report of using apparent activation energies to investigate battery precursor coprecipitation reactions, and these methods should be extendable to chemistry for coprecipitation of many multicomponent transition metal particles which have application in multiple fields including energy storage materials.

The element of this chapter has been submitted to Journal of Powder Technology.

5.2. Introduction

Lithium-ion (Li-ion) batteries are a major technology for consumer electronics and one of the few options for energy storage in transportation applications due to the high energy and power densities that can be achieved [1,2]. While many components and physical properties have an important role in the electrochemical charge and discharge processes, the intrinsic properties of the cathode active materials are among the most important that define the limits of the performance metrics of the battery which include electrochemical capacity, rate capability, cycling stability, and cost [3–5]. Extensive research has reported the optimization of cathode active materials through various strategies including metal ion substitution, surface coating, and particle morphology control to improve the electrochemical properties of the resulting batteries [6–12]. While there are many routes to improve cathode material performance and there are many cathode materials to choose from, high levels of control over the composition and phase of the final cathode material are needed to produce high performance and reproducible battery active materials regardless of the cathode chemistry.

Coprecipitation is a popular method reported in the literature to produce transition metal (TM) precursors which are subsequently lithiated and calcined to produce Li-ion battery active materials [13–20]. The method is straightforward to scale up to larger volume material production and is amenable to both batch and continuous systems [14,21,22]. Even though precipitation synthesis procedures are often straightforward, careful control over the solution chemistry can result in complex compositions and morphologies such as compositional core-shell particles [23–26], particles with gradients from core to surface in their concentration [27–29], and a diversity of shapes including spheres, rods, plates, and dumbbells [11,14,30–32]. While precipitation is a robust and scalable route to synthesize battery active material precursors and complex compositions and morphologies are possible, methods are needed to characterize the precipitation process to improve rational and predictive control of these materials. For example, previous work has demonstrated that in some cases the TM precursors (and subsequently the TM oxide final active materials) had compositions that significantly deviated from feed stoichiometry to the synthesis process, resulting in deleterious effects on the electrochemical performance of the final active material [14,33]. In-situ tracking of the concentrations of the TMs in the solid and liquid phase in the reactor was demonstrated as one method to characterize the precipitation process and understand the origins of compositional deviations [14]. Subsequent follow up reports demonstrated that combining the in-situ concentration information during synthesis with in-situ tracking of the evolution of the particle size distribution yields further insights into the rate of precipitation of the precursors and the different nucleation and growth regimes the particles can experience as a function of TM composition in the feed [34]. These previous reports were focused on compositional deviations of the TM precursors, but producing pure and/or controllable crystal phases of the precursor is also important to synthesizing high performance electrode materials. In particular, phase pure particles are often needed to rationally guide particle morphology [11], and if the particles are not phase-pure the appropriate amount of lithium salt to add before calcination can be challenging to determine [29].

In this chapter, a method will be demonstrated to probe the apparent activation energy during the coprecipitation of TM battery precursors. It is noted here that the activation energies calculated from the experimental method in this study result from a combination of physical and chemical processes including mass transfer, chemical reaction, nucleation formation and initial growth and thus the energies are referred to as apparent activation energies. To our knowledge, this method has never been applied to investigate battery precursor particles, nor to the TM oxalates that will be the focus of this study. The method was based on similar analysis applied to the formation of vanadium oxide precipitates – although in contrast to the present report the vanadium precipitates contained a single TM and were presumably all of the same composition and crystal structure [35]. The precipitation of metal oxalate was chosen as the exemplar system because TM oxalates have previously been reported as precursors for the synthesis of high-performance battery materials [14,36,37]. In addition, oxalate forms phase pure dihydrate precursors across a variety of TMs used for Li-ion battery cathodes, including Co, Mn, and Ni. In this study, Mn oxalate, Ni oxalate, and blends of Mn and Ni oxalate of varying Mn:Ni ratios were investigated. Such precursors can be lithiated and calcined to different final active materials depending on their Mn:Ni ratio, for example $LiMn_{0.5}Ni_{0.5}O_2$ for Mn:Ni 1:1 $LiMn_{1.5}Ni_{0.5}O_4$ for Mn:Ni 3:1 [38,39]. This report will first present the apparent activation energies of Mn and Ni oxalate coprecipitations at different Mn:Ni feed compositions. Then, the sensitivity of the crystal structure of the produced precipitates, determined from refinement of powder X-ray diffraction patterns, to the Mn:Ni composition will be reported in the context of the apparent activation energy results. The results presented suggest that the apparent activation energy reflects the composition-dependent structure of the precipitate particles that form in the reaction solution. It is expected that this analysis would be valuable for any battery precursor system where multiple structural phases are present, which is the case for not only TM oxalate precipitation but also for other TM precursor systems such as TM carbonate and hydroxide [29].

5.3. Experimental

5.3.1. Measurement of Coprecipitation Induction Time

Coprecipitation of TM oxalate particles was conducted by mixing solutions of dissolved TM sulfate with dissolved sodium oxalate. Laboratory grade $MnSO_4·H_2O$, $NiSO_4·6H_2O$, and $Na_2C_2O_4$ (all from Fisher) were used for the coprecipitation reaction. 50 mL of 15 mM TM solution with varying Mn:Ni ratios and 50 mL of 15 mM oxalate solution were prepared separately by dissolving TM salts and oxalate salt. The solutions were heated to the desired target temperature (50, 55, 60, and 65 °C for each Mn:Ni concentration investigated) and then mixed together all at once by pouring the TM solution into the oxalate solution. The mixed solution was homogeneous mixed with a stir bar rotating at 300 rpm for 10 seconds and then a small portion of the solution was poured into a 3 mL sample cuvette. The cuvette was then quickly put into an ultraviolet-visible (UV-Vis) spectrometer (PerkinElmer Lambda 35) and the transmitted intensity of light at a wavelength of 480 nm that reached the detector after passing through cuvette was collected every 10 seconds. The experiment was concluded when the measured extinction of transmitted light decreased after reaching a plateau, which occurred after 500 to 1000 seconds depending on the solution temperature and feed composition. The wavelength of 480 nm was chosen for analysis because at this wavelength solutions of dissolved Ni and Mn salts both had negligible extinction. It was thus assumed that any increases in extinction resulted from light being scattered by the resulting solid particles that nucleate and grow during the coprecipitation process. Throughout the UV-Vis measurements, the cuvette was in a temperature-controlled cuvette holder (PerkinElmer PTP-1 Peltier System) which maintained the solution temperature at the target temperature for the duration of each coprecipitation experiment.

An example of the measured extinction as a function of reaction time is shown in Fig. 1a. It can be seen that the extinction was low at the beginning of the reaction because the particles that scatter the light have not yet had significant nucleation. As the time elapsed, the extinction slowly increased and then transitioned to a region where it increased linearly with time. After this linear increase the extinction would reach a maximum and then slowly start to decrease. The general profile of the extinction as a function of time was the same for all TM ratios synthesized, and thus the process was considered in the context of three different regions separated by dashed lines in Fig. 1a. Region I was the inert period when the reactant species have mixed but particle nucleation has not reached a significant extent and thus the curve was almost horizontal. Region II was the transition period when the nuclei have stabilized and started to grow. Region III was the period of continuous and fast particle growth. Both region I and region III of the curve were linear and were fit using least squares methods, and dashed lines of best fit have been added in Fig. 1a. The coprecipitation particle growth starting point, or induction time (τ) was determined by the intersection between the lines of best fit for the inert region (I) and the growth region (III). This method for measuring τ was both a reliable and reproducible way to measure the induction period as opposed to visual observation of the reaction solution [35]. Experiments measuring □ were conducted at multiple temperatures and multiple Mn:Ni ratios, and each specific temperature and solution composition was repeated at a minimum in triplicate to determine average induction times. As will be described below, these induction times were used to calculate apparent activation energies.

5.3.2. Calculation of Apparent Activation Energy

To determine the apparent activation energy, the induction time was assumed to follow Arrhenius behavior. For each TM solution ratio, the average induction time was measured at four different temperatures. Fig. 1b shows an example of how the induction time information was then used, where plots were generated with ln(τ) on the y-axis and the inverse of the reaction temperature (in °K) on the x-axis. Assuming Arrhenius behavior for the induction process, the relationship between induction time and temperature would be of the form [208]:

$$\ln(\tau) = -\ln(A) + \frac{E}{k_B T} \tag{1}$$

where A is the pre-exponential constant, E is the apparent activation energy and k_B is Boltzmann's constant. The slope of a linear fit of ln(τ) vs. 1/T thus yields E/kB and a value for E, the apparent activation energy for those solution conditions. Thus, the slope of the line of best fit in Fig. 1b is equal to E/kB and the apparent activation energy can be determined from this analysis.

5.3.3. Materials Characterization

For material characterization, larger scale synthesis was conducted for each Mn:Ni ratio and the precursor particles were filtered, rinsed with distilled water, and put into an oven (Carbolite) at 80 °C in an air atmosphere overnight to dry the powder. More detailed description of the synthesis process can be found in previous publications [14,41]. The process and reaction conditions were all the same as used for the induction time measurements except that the total solution volume was increased to 800 mL and the synthesis was conducted within a 1 L beaker. The crystal structures of the resulting coprecipitated particles were analyzed by powder X-ray diffraction (XRD) with a PANalytical X'pert ProMPD using a Cu-Kα radiation source. Fullprof was used to find the lattice parameters of each sample [42]. Thermal gravimetrical analysis (TGA, TA Q50) was conducted to measure the temperatures of structural water loss and oxalate decomposition, which were each determined by peaks in the plot of the differential mass change as a function of temperature. All TGA measurements were performed in air with a heating rate of 10 °C min−1.

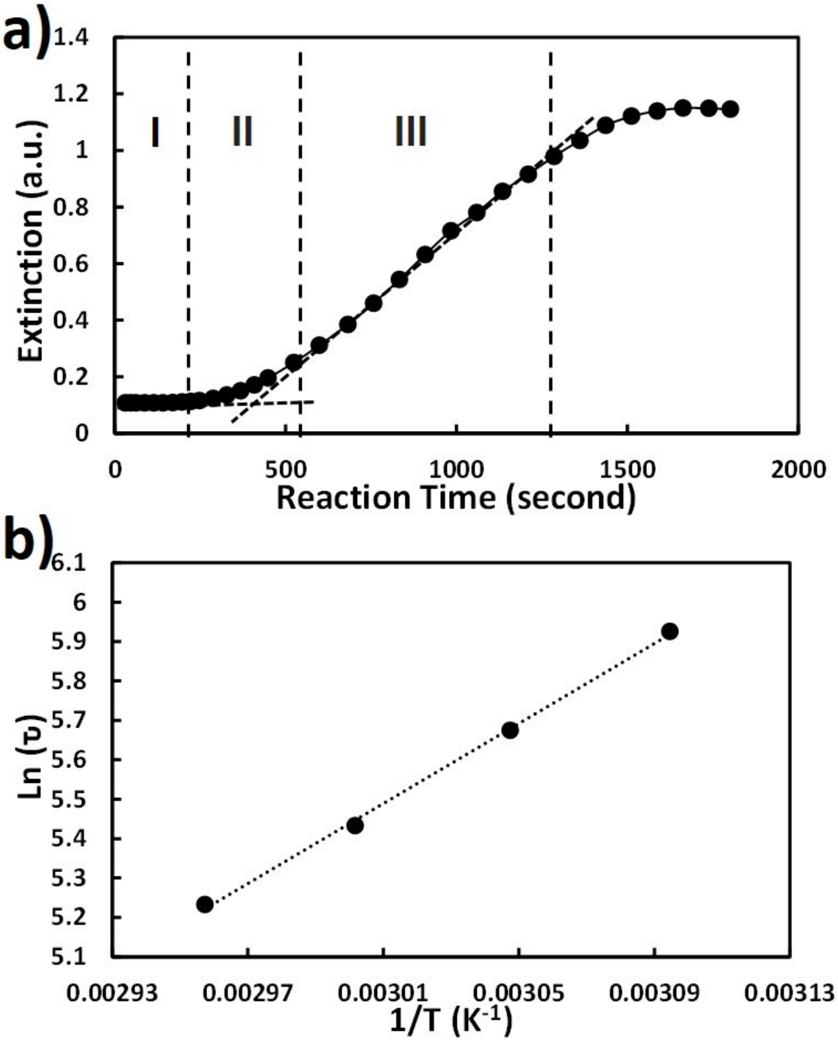

Figure 1. a) Extinction at 480 nm measured using UV-Vis on the coprecipitation reaction solution as a function of time. Regions I, II, and III are discussed in the text and the general profile was representative for all solution compositions investigated. b) Example of plot used to extract the

apparent activation energy from the induction time measured as a function of temperature assuming Arrhenius behavior. For both a) and b) all precipitations were conducted with 15 mM total TM in the initial solution and a 3:1 Mn:Ni ratio. The temperature for a) was 50 °C.

5.4. Results and Discussion

It was postulated that apparent activation energy of the nucleation and growth of the coprecipitated particles would provide a quantitative route to understand the impact of solution composition on the phase of the resulting particles which form. This idea was based on previous observations that at the solution conditions used in this study 1) pure Mn and Ni oxalate form different phases, and 2) pure Mn and Ni oxalate precipitate at very different rates [14]. Thus, it was expected that apparent activation energy would provide a quantitative descriptor that differentiates Ni from Mn precipitation. Given that the pure Mn and Ni oxalates form different phases, it was expected that they would have limits to the extent to which they could form a solid solution, and thus the apparent activation energy might also provide insights into the solution conditions where a second phase started to precipitate. It was expected that Arrhenius behavior for the coprecipitation reaction would be appropriate, as it had been previously applied to other crystallization processes [35,43]. Initial experiments such as those in Fig. 1b also revealed good linear relationships when using the linearized form of the Arrhenius relationship with respect to (Equation 1), and as will be described in further detail across all reaction conditions the fit was very good.

The apparent activation energies determined for each solution composition are shown in Fig.2. Error bars represent the standard deviation between the experimental data and the least squares fit to determine the activation energy, and some were quite wide. Large error bars may have been due to a number of factors, including local temperature fluctuations during coprecipitation, surface imperfections of the vial containers, or inhomogeneity in the local mixing provided by the stirring [44–46]. Table 1 also provides the detailed numerical values associated with these energies. The R2 values were almost all larger than 0.9, indicating a good linear fit of Equation 1 across the range of Mn feed compositions explored. The smallest R2 value is 0.85 at Mn feed content of 70% while values of other feed compositions were all above 0.9 (Table 1).

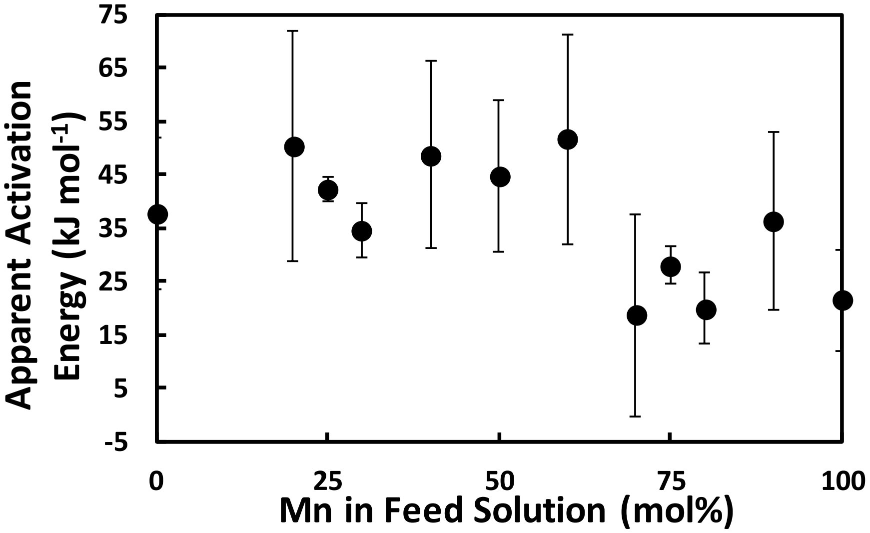

Figure 2 Apparent activation energies of the coprecipitation reactions with differing feed Mn:Ni ratios. Error bars represent the standard deviation between the experimental data and the least squares fit to determine he activation energy.

To facilitate discussion of results, the nomenclature MnXXNiYY will be used, where the "XX" and "YY" represent the feed solution to the reaction being XX mol% Mn and YY mol% Ni. Mn100 and Ni100 represent the pure Mn and pure Ni coprecipitation. The activation energies of pure Mn and pure Ni oxalate coprecipitation were determined to be 37.8 ± 13.2 kJ mol-1 and 21.4 ± 9.46 kJ mol-1, respectively. These quantitative results, with Mn oxalate having a lower apparent activation energy for coprecipitation, were in agreement with observations that Mn oxalate coprecipitates faster than Ni oxalate under otherwise identical reaction conditions.

Table 1. Apparent activation energy determined from Arrhenius fitting of the induction time as a function of temperature for varying Mn concentrations in the feed to the coprecipitation.

Solution Mn content (mol %)	Activation energy (kJ mol^{-1})	Fitting R^2	Activation Energy Error (kJ mol^{-1})
0	37.8	0.94	13.2
20	50.5	0.92	21.6
25	42.2	1.00	2.29
30	34.6	0.99	5.21
40	48.8	0.94	17.6
50	44.8	0.95	14.1
60	51.6	0.93	19.6
70	18.7	0.84	18.9
75	28.0	0.99	3.57
80	19.9	0.95	6.60
90	36.3	0.90	16.8
100	21.4	0.91	9.46

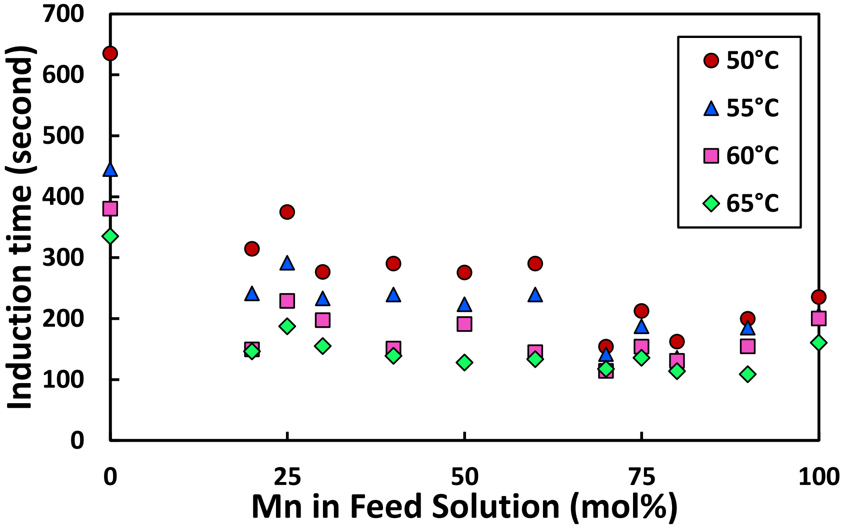

Figure 3 Measured induction times of the coprecipitation reactions with different feed Mn:Ni ratios at 50 °C (red circles), 55 °C (blue triangles), 60 °C (pink squares), and 65 °C (green diamonds).

Comparing the activation energies of coprecipitations with Mn feed molar percentage between 20% and 50% (Fig.2), there was a slight trend of increasing activation energy with increasing Mn in the feed solution, though the size of the error bars makes concrete assignment of this effect challenging. It is noted that within this range as the Mn feed content increased the intercept of the Arrhenius fits decreased (data not shown). The decrease in the intercept reflected a decrease in the pre-exponential term of the Arrhenius equation (Equation 1). The decrease of the pre-exponential constant with increasing relative Mn in the coprecipitation solution reflected a decrease in the absolute crystallization rates. This analysis was consistent with the decrease of the induction times across all temperatures that the coprecipitation was performed (Fig.3). It can be seen in Fig.3 that there was a significant drop of induction times from pure Ni coprecipitation to 20 mol% Mn blend coprecipitation and then a slow decrease of the induction time as the Mn content was further increased until 70 mol% Mn was used. A slight local minimum in the induction time measured at all temperatures at 20 mol% Mn may have been due to transformation of the crystallization mechanism from homogeneous to heterogeneous crystallization [44], due to a seeding effect that the initial and fast forming manganese oxalate nuclei acting as the seeds to facilitate faster nickel precipitation [14]. This seeding effect and subsequent observation of qualitative reduction in induction time was previously suggested and supported by experimental evidence via pure Mn oxalate seed addition at the initiation of pure Ni oxalate coprecipitation in a previous study [14,47]. The slight increase of the apparent activation energy with increasing Mn content in the feeding solutions, while in contrast to the absolute induction time measurements, may indicate the structure distortion of the precipitate particles as they start to grow due to the different phases of the initial nuclei seeds and the later larger crystals that form (crystal structure discussed in further detail below) [41]. The high Mn content seeds may result in a higher barrier for Ni precipitation which would be reflected by the increasing activation energy, while the apparent crystallization rates represented via induction time were decreased due to the compensation by the increase of fast-forming Mn nuclei which provided more seed surface to facilitate a higher overall precipitation rate.

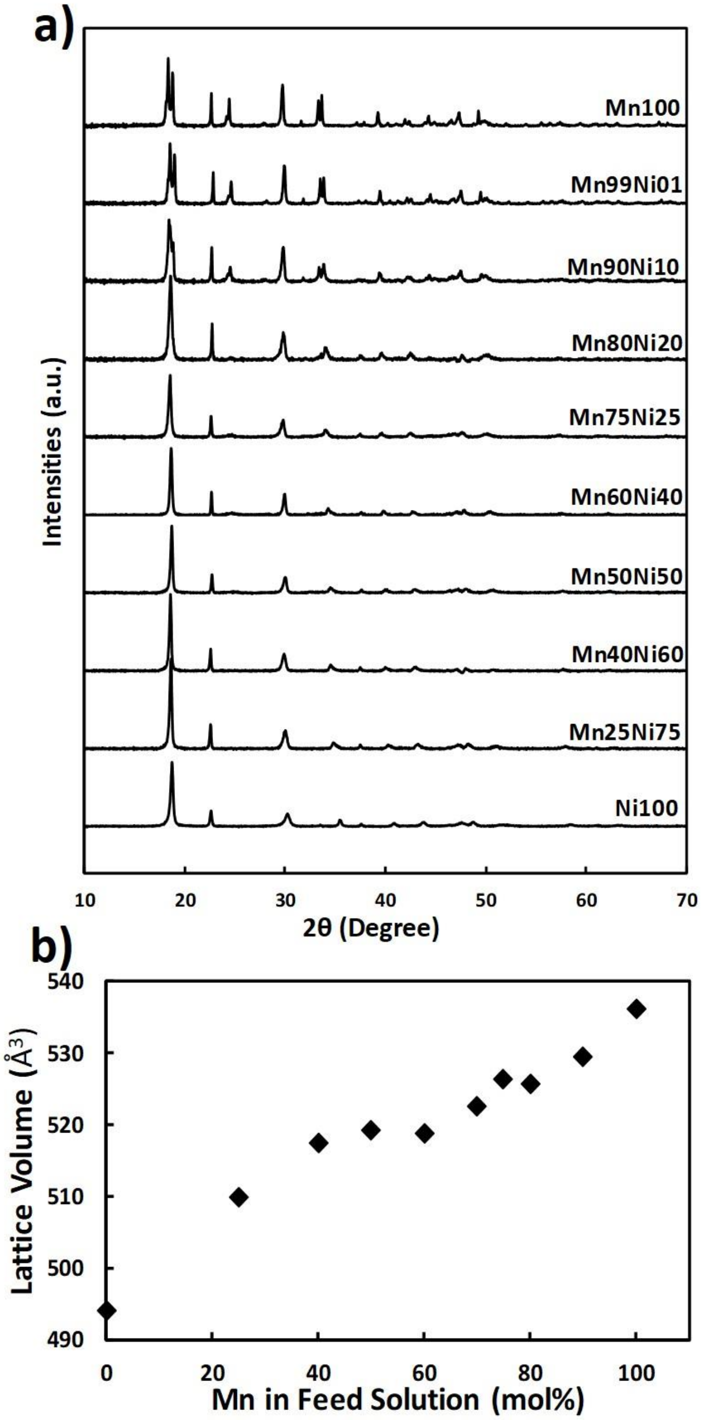

Figure 4. a) XRD patterns of the obtained precipitate particles with varying Mn:Ni ratio feed concentrations. MnXXNiYY indicates the feed was XX mol% Mn and YY mol% Ni. b) Lattice volumes determined from refining the patterns in a).

Inspection of Fig. 2 reveals a significant drop of apparent activation energy when the Mn content increased to 70% of the feed solution. The activation energy at 70 mol% Mn was calculated to be 18.7 ± 18.9 kJ mol-1, significantly smaller compared to the 37.8 ± 13.2 kJ mol-1, 42.2 ± 2.29 kJ mol-1, and 44.8 ± 14.1 kJ mol-1 of Ni100, Mn25Ni75 and Mn50Ni50 coprecipitations. It is speculated that this decrease in the apparent activation energy may have reflected a phase transition in the formed Mn Ni oxalate particles. As shown in the XRD patterns of the obtained Mn Ni oxalate particles (Fig. 4a), the particles collected from feed solutions with 90 mol% or higher Mn content in the feed solution exhibited the peaks of Mn oxalate, while the particles collected from feed solutions with less than 90 mol% Mn had peaks consistent with the structure of Ni oxalate. Previous literature has reported that the orthorhombic β-$MC_2O_4 \cdot 2H_2O$ (where M stands for the d-block TM) with space group P212121 was a thermodynamically preferred and more stable structure compared to the α-MC_2O_4·2H2O with monoclinic space group C2/c [48–50]. In the coprecipitation conditions in this paper, pure Ni oxalate formed the β phase and pure Mn oxalate formed the α phase. The Ni oxalate β phase being the dominant structure across most of the compositional range (until 90 mol% Mn) was consistent with the higher stability of the β phase dictating the crystal structure of the resulting oxalate material powder. Also, the substitution of Mn would be expected to distort the crystal structure, which may have resulted in a slight increase in the apparent activation energy as a function of Mn mol% in the feed as the Mn was increased from 0 to 60 mol% (although it is noted the standard deviation in the apparent activation energy measurements was relatively high). The decrease of the activation energy at Mn70Ni30 composition may have been due to a phase transition of the bulk precipitates formed early in the coprecipitation from orthorhombic β-phase to the monoclinic α-phase, which is the phase of Mn concentrated seeds. The structural similarity between the early formed manganese oxalate seeds and the particles subsequently growing on these seeds would have reduced the apparent activation barrier of the particle nucleation and growth [44]. Previous studies on the calcium carbonate coprecipitation reactions have revealed that higher similarity between the precipitates and the seeds resulted in a significant increase in reaction rates [51,52]. Although the apparent activation energy measurements suggest that the precipitate particles formed may have been α-phase at a feed of 70 mol% Mn, the phase was not observed in powder XRD until the Mn in the feed was 90 mol%. The higher Mn composition required to observe the α-phase in XRD may be due to the fact that the phase transition only happened locally and on the early formed precipitates and that gradually the more stable β phase was the dominant crystal structure that grew during the coprecipitation. If the amount of a phase was relatively small relative to the total sample mass, as well as buried within the cores of the precipitate particles, it would not be surprising that it would not be detected with powder XRD. The calculated lattice parameters and lattice volumes of the oxalate powders were obtained using Rietveld refinement and are summarized in Table 2. The lattice volumes as a function of Mn content in the solution are also plotted in Fig. 4b. It can be seen that the lattice volume increased as the Mn content increased, consistent with Mn^{2+} having a larger ionic radius than Ni^{2+} [14].

As the manganese content was increased to 100% in the solution (pure Mn coprecipitation), the activation energy was 21.42 ± 9.46 kJ/mol, similar to that of the phase transition point. It can be seen from the plot that in each of the two single-phase ranges of the precipitation reaction, there appeared to be a peak of the activation energy in the middle of the composition range while the activation energy was the lowest for the pure feed solution. This may reflect the distorted structure of the precipitate due to the existence of multiple TM ions with different sizes in the structure.

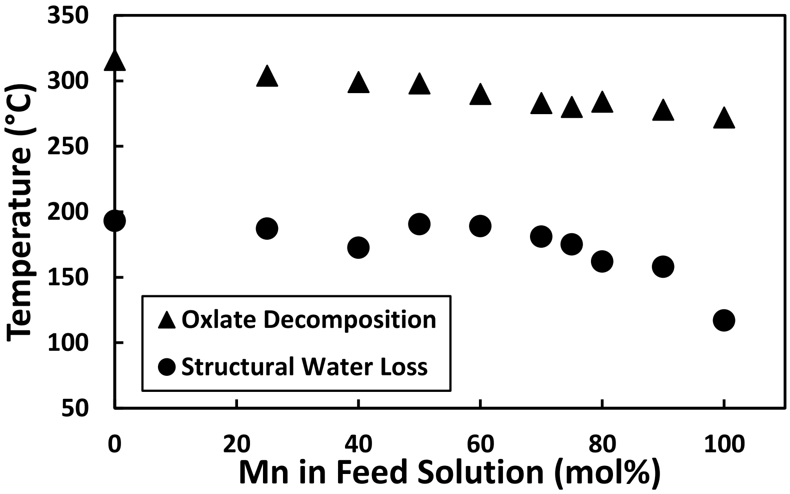

Figure 5. Peaks in differential mass loss from TGA on the powders collected from the different reaction solutions corresponding to oxalate decomposition (black triangles) and structural water loss (black circles).

TGA analysis was also conducted with the collected precipitate particles. All materials had two distinct peaks in differential mass loss. The first reflected the loss of structural water, which typically occurred at below 200°C and has previously been used to indicate the structural stability of a material [41,53]. Higher structural water loss temperature implies a more stable structure which holds the structural water more tightly. The differential mass loss peak associated with structural water loss as a function of Mn mol% in the feed solution is shown in Fig. 5 with numerical values provided in Table 2. It can be seen that the temperature of structural water loss increased with increasing Ni content (or decreasing Mn content) in the solution, and concurrently incorporated into the precipitate phase. This observation was in agreement with the higher stability of the β phase which pure Ni oxalate formed [14]. As Mn content was increased in the feed solution and in the precipitate structure, the formed precipitate underwent constantly increasing structural distortion in the single β phase as Mn content increased, reducing the structural stability of the phase and decreasing the structural water loss temperature. When Mn content reached the threshold of phase transition to the Mn oxalate phase which forms the less stable □ phase, the drop of structural stability would be expected to accelerate the decrease in the structural water loss temperature. This expectation was consistent with the significant decrease in the structural water loss temperature when 70 mol% Mn was in the feed (Fig. 5). The increasing sensitivity to the Mn content on the structural water loss occurs at the composition where apparent activation energy had a dramatic change, indicating that the change in phase of the precipitates may impact the structural stability of the material even as the bulk phase observed in XRD does not have a detectable phase transition. The peak temperature in differential mass loss for oxalate decomposition as a function of Mn content in the feed solution was also plotted in Fig. 5 (numerical values in Table 2). The oxalate decomposition temperature also decreased as more Mn was added to the particles, although the decrease appeared to have a similar gradual slope across the compositional range.

Table 2. Lattice parameters determined from Rietveld refinement of the XRD patterns for oxalate precipitates formed with different Mn:Ni ratios in the feed. The differential mass loss peak temperatures from TGA analysis associated with structural water loss and oxalate decomposition is also listed for each feed condition.

Mn in the Feed Solution (mol %)	Phase	Lattice Parameters				Lattice Volume (Å^3)	Peak in Differential Mass Loss (°C)	
		a	b	c	β		Structural Water Loss	Oxalate Decomposition
0	β	11.81	5.33	15.70		494.1	193	316
25	β	11.91	5.44	15.74		509.9	187	304
40	β	11.97	5.49	15.75		517.5	173	299
50	β	11.97	5.52	15.72		519.3	191	298
60	β	11.98	5.52	15.69		518.8	189	290
70	β	12.01	5.55	15.68		522.6	181	283
75	β	12.00	5.57	15.75		526.4	175	280
80	β	12.00	5.58	15.69		525.7	162	284
90	□	12.00	5.63	10.00	128.4	529.6	158	278
100	□	12.08	5.66	10.03	128.6	536.2	117	272

The results presented above, when combined, suggest that the apparent activation energies for the precipitates with varying compositions of the blend of TMs provide insights into the composition where precipitate particles of different phases start to form. While after full growth of the particles the new phase does not always have the necessary amount and/or crystallinity of material to be detected in powder XRD analysis, the local minimum of the activation energy can be used to determine the solution conditions where multiple phases of nuclei may form in the solution. It should be noted that it is suspected that the local minimum in apparent activation energy was resulted from the new phase facilitating the growth stage of the precipitation by seeding further growth faster due to the similarity between seeds and further growing particles in phase. Thus, other systems may behave quite differently depending on whether there are two polymorphs dependent on the TM or cations used, and the relative stability and apparent activation energy of the pure phase materials. Further study will also be needed to confirm the formation of both phases during the nucleation phase of the precipitation speculated in this report.

5.5. Conclusions

This report probed the interactions within a multicomponent cation coprecipitation process via apparent activation energy measurements for particles often used as precursors to synthesize battery materials. Apparent activation energy was measured by analysis of induction times of the crystallization reaction process as a function of temperature using UV-Vis spectroscopy. It was found that a local minimum of the experimentally measured activation energy occurred near to the composition where a new phase becomes preferred for the resulting precipitate particles. The observed minimum in the apparent activation energy appears to be consistent with where the precipitate particles of different phases form, although one of the phases was not detected in the final particles using bulk XRD on the collected particles, suggesting they were not retained in sufficient amount and/or crystallinity during the more substantive growth phase of the material. The apparent activation energy analysis is expected to provide valuable insights to many coprecipitation processes with multicomponent cations where multiple phases may have been observed depending on solution conditions.

5.6. Reference

[1] J.B. Goodenough, Y. Kim, Challenges for rechargeable Li batteries, Chem. Mater. 22 (2010) 587–603. doi:10.1021/cm901452z.

[2] J.B. Goodenough, K.-S.S. Park, The Li-Ion Rechargeable Battery: A Perspective, J. Am. Chem. Soc. 135 (2013) 1167–1176. doi:10.1021/ja3091438.

[3] B. Scrosati, J. Garche, Lithium batteries: Status, prospects and future, J. Power Sources. 195 (2010) 2419–2430. doi:10.1016/j.jpowsour.2009.11.048.

[4] C.M. Julien, A. Mauger, Review of 5-V electrodes for Li-ion batteries: Status and trends, Ionics (Kiel). 19 (2013) 951–988. doi:10.1007/s11581-013-0913-2.

[5] D.L. Wood, J. Li, C. Daniel, Prospects for reducing the processing cost of lithium ion batteries, J. Power Sources. 275 (2015) 234–242. doi:10.1016/j.jpowsour.2014.11.019.

[6] T.H.H. Cho, S.M.M. Park, M. Yoshio, T. Hirai, Y. Hideshima, Effect of synthesis condition on the structural and electrochemical properties of Li[Ni1/3Mn1/3Co1/3]O2prepared by carbonate co-precipitation method, J. Power Sources. 142 (2005) 306–312. doi:10.1016/j.jpowsour.2004.10.016.

[7] Y.K. Sun, B.R. Lee, H.J. Noh, H. Wu, S.T. Myung, K. Amine, A novel concentration-gradient Li[Ni0.83Co0.07Mn0.10]O2cathode material for high-energy lithium-ion batteries, J. Mater. Chem. 21 (2011) 10108–10112. doi:10.1039/c0jm04242k.

[8] L. Li, S. Song, X. Zhang, R. Chen, J. Lu, F. Wu, K. Amine, Ultrasonic-assisted co-precipitation to synthesize lithium-rich cathode Li1.3Ni0.21Mn0.64O2+d materials for lithium-ion batteries, J. Power Sources. 272 (2014) 922–928. doi:10.1016/j.jpowsour.2014.08.063.

[9] Q. Ma, D. Mu, Y. Liu, S. Yin, C. Dai, Enhancing coulombic efficiency and rate capability of high capacity lithium excess layered oxide cathode material by electrocatalysis of nanogold, RSC Adv. 6 (2016) 20374–20380. doi:10.1039/C5RA26667J.

[10] F. Wu, H. Lu, Y. Su, N. Li, L. Bao, S. Chen, Preparation and electrochemical performance of Li-rich layered cathode material, Li[Ni0.2Li0.2Mn0.6]O2, for lithium-ion batteries, J. Appl. Electrochem. 40 (2010) 783–789. doi:10.1007/s10800-009-0057-2.

[11] J.P. Robinson, G.M. Koenig, Tuning solution chemistry for morphology control of lithium-ion battery precursor particles, Powder Technol. 284 (2015) 225–230. doi:10.1016/j.powtec.2015.06.070.

[12] G.M. Koenig, J. Ma, B. Key, J. Fink, K.-B. Low, R. Shahbazian-Yassar, I. Belharouak, Composite of LiFePO4 with Titanium Phosphate Phases as Lithium-Ion Battery Electrode Material, J. Phys. Chem. C. 117 (2013) 21132–21138. doi:10.1021/jp4074174.

[13] H.S. Shin, S.H. Park, Y.C. Bae, Y.K. Sun, Synthesis of Li[Ni0.475Co0.05Mn0.475] O2cathode materials via a carbonate process, Solid State Ionics. 176 (2005) 2577–2581. doi:10.1016/j.ssi.2005.07.008.

[14] H. Dong, G.M. Koenig Jr, Compositional control of precipitate precursors for lithium-ion battery active materials: role of solution equilibrium and precipitation rate, J. Mater. Chem. A. 5 (2017) 13785–13798. doi:10.1039/C7TA03653A.

[15] A. Van Bommel, J.R. Dahn, Analysis of the Growth Mechanism of Coprecipitated Spherical and Dense Nickel , Manganese , and Cobalt -Containing Hydroxides in the Presence of

Aqueous Ammonia Analysis of the Growth Mechanism of Coprecipitated Spherical and Dense Nickel , Manganese , an, Chem. Mater. 21 (2009) 1500–1503. doi:10.1021/cm803144d.

[16] G.-H. Kim, S.-T. Myung, H.J. Bang, J. Prakash, Y.-K. Sun, Synthesis and Electrochemical Properties of Li[Ni[sub 1/3]Co[sub 1/3]Mn[sub (1/3−x)]Mg[sub x]]O[sub 2−y]F[sub y] via Coprecipitation, Electrochem. Solid-State Lett. 7 (2004) A477. doi:10.1149/1.1809554.

[17] D. Liu, J. Han, J.B. Goodenough, Structure, morphology, and cathode performance of Li1-x[Ni0.5Mn1.5]O4 prepared by coprecipitation with oxalic acid, J. Power Sources. 195 (2010) 2918–2923. doi:10.1016/j.jpowsour.2009.11.024.

[18] X. Lu, C. Liu, W. Zhu, Z. Lu, W. Li, Y. Yang, G. Yang, Synthesis of micron-sized LiNi0.5Mn1.5O4 single crystals through in situ microemulsion/coprecipitation and characterization of their electrochemical capabilities, Powder Technol. 343 (2019) 445–453. doi:10.1016/J.POWTEC.2018.11.038.

[19] J.H. Kim, W.C. Choi, H.Y. Kim, Y. Kang, Y.-K. Park, Preparation of mono-dispersed mixed metal oxide micro hollow spheres by homogeneous precipitation in a micro precipitator, Powder Technol. 153 (2005) 166–175. doi:10.1016/J.POWTEC.2005.03.004.

[20] L. Li, X. Li, Z. Wang, H. Guo, P. Yue, W. Chen, L. Wu, A simple and effective method to synthesize layered LiNi0.8Co0.1Mn0.1O2 cathode materials for lithium ion battery, Powder Technol. 206 (2011) 353–357. doi:10.1016/J.POWTEC.2010.09.010.

[21] D. Wang, I. Belharouak, G.M. Koenig, G. Zhou, K. Amine, Growth mechanism of Ni0.3Mn0.7CO3 precursor for high capacity Li-ion battery cathodes, J. Mater. Chem. 21 (2011) 9290. doi:10.1039/c1jm11077b.

[22] Y. Kim, D. Kim, Synthesis of high-density nickel cobalt aluminum hydroxide by continuous coprecipitation method, ACS Appl. Mater. Interfaces. 4 (2012) 586–589. doi:10.1021/am201585z.

[23] Y.K. Sun, S.T. Myung, M.H. Kim, J. Prakash, K. Amine, Synthesis and characterization of Li[(Ni0.8Co 0.1Mn0.1)0.8(Ni0.5Mn 0.5)0.2]O2 with the microscale core-shell structure as the positive electrode material for lithium batteries, J. Am. Chem. Soc. 127 (2005) 13411–13418. doi:10.1021/ja053675g.

[24] Y.K. Sun, S.T. Myung, B.C. Park, K. Amine, Synthesis of spherical nano- To microscale core-shell particles Li[(Ni 0.8Co 0.1Mn 0.1) 1-x(Ni 0.5Mn 0.5) x]O 2 and their applications to lithium batteries, Chem. Mater. 18 (2006) 5159–5163. doi:10.1021/cm061746k.

[25] K.-S. Lee, S.-T. Myung, Y.-K. Sun, Synthesis and electrochemical performances of core-shell structured Li[(Ni1/3Co1/3Mn1/3)0.8(Ni1/2Mn1/2)0.2]O2 cathode material for lithium ion batteries, J. Power Sources. 195 (2010) 6043–6048. doi:10.1016/J.JPOWSOUR.2010.02.002.

[26] Y. Sun, S. Myung, H. Shin, Y.C. Bae, Novel Core−Shell-Structured Li[(Ni0.8Co0.2)0.8(Ni0.5Mn0.5)0.2]O2 via Coprecipitation as Positive Electrode Material for Lithium Secondary Batteries, J. Phys. Chem. B. 110 (2006) 6810–6815. doi:10.1021/jp0571473.

[27] Y.-K. Sun, Z. Chen, H.-J. Noh, D.-J. Lee, H.-G. Jung, Y. Ren, S. Wang, C.S. Yoon, S.-T. Myung, K. Amine, Nanostructured high-energy cathode materials for advanced lithium batteries, Nat. Mater. 11 (2012) 942–947. doi:10.1038/nmat3435.

[28] Y.K. Sun, D.H. Kim, C.S. Yoon, S.T. Myung, J. Prakash, K. Amine, A novel cathode material with a concentrationgradient for high-energy and safe Lithium-Ion batteries, Adv. Funct. Mater. 20 (2010) 485–491. doi:10.1002/adfm.200901730.

[29] G.M. Koenig, I. Belharouak, H. Deng, Y.-K. Sun, K. Amine, Composition-Tailored Synthesis of Gradient Transition Metal Precursor Particles for Lithium-Ion Battery Cathode Materials, Chem. Mater. 23 (2011) 1954–1963. doi:10.1021/cm200058c.

[30] D.K. Kim, P. Muralidharan, H.-W. Lee, R. Ruffo, Y. Yang, C.K. Chan, H. Peng, R.A. Huggins, Y. Cui, Spinel LiMn2O4 Nanorods as Lithium Ion Battery Cathodes, Nano Lett. 8 (2008) 3948–3952. doi:10.1021/nl8024328.

[31] R. Mei, X. Song, Y. Yang, Z. An, J. Zhang, Plate-like LiFePO4crystallite with preferential growth of (010) lattice plane for high performance Li-ion batteries, RSC Adv. 4 (2014) 5746–5752. doi:10.1039/c3ra45755a.

[32] G. Li, L. Qi, P. Xiao, Y. Yu, X. Chen, W. Yang, Effect of precursor structures on the electrochemical performance of Ni-rich LiNi0.88Co0.12O2 cathode materials, Electrochim. Acta. 270 (2018) 319–329. doi:10.1016/J.ELECTACTA.2018.03.106.

[33] M.M. Thackeray, Lithiated Oxides for Lithium Ion Batteries, J. Electrochem. Soc. 142 (1995) 2558–2563. doi:10.1149/1.2050053.

[34] H. Dong, A. Wang, G. Smart, D. Johnson, G.M. Koenig, In-situ analysis of nucleation and growth of transition metal oxalate battery precursor particles via time evolution of solution composition and particle size distribution, Colloids Surfaces A Physicochem. Eng. Asp. 558 (2018) 8–15. doi:10.1016/J.COLSURFA.2018.08.047.

[35] D. Oboroceanu, N. Quill, C. Lenihan, D.N. Eidhin, S.P. Albu, R.P. Lynch, D.N. Buckley, Effects of Temperature and Composition on Catholyte Stability in Vanadium Flow Batteries: Measurement and Modeling, J. Electrochem. Soc. 164 (2017) A2101–A2109. doi:10.1149/2.1401709jes.

[36] D. Wang, I. Belharouak, G. Zhou, K. Amine, Synthesis of Lithium and Manganese-Rich Cathode Materials via an Oxalate Co-Precipitation Method, J. Electrochem. Soc. 160 (2013) A3108–A3112. doi:10.1149/2.016305jes.

[37] Z. Qi, G.M. Koenig, High-Performance LiCoO2 Sub-Micrometer Materials from Scalable Microparticle Template Processing, ChemistrySelect. 1 (2016) 3992–3999. doi:10.1002/slct.201600872.

[38] B.L. Cushing, J.B. Goodenough, Influence of carbon coating on the performance of a LiMn0.5Ni0.5O2 cathode, Solid State Sci. 4 (2002) 1487–1493. doi:10.1016/S1293-2558(02)00044-4.

[39] K. Amine, H. Tukamoto, H. Yasuda, Y. Fujita, Preparation and electrochemical investigation of LiMn2 − xMexO4 (Me: Ni, Fe, and x = 0.5, 1) cathode materials for secondary lithium batteries, J. Power Sources. 68 (1997) 604–608. doi:10.1016/S0378-7753(96)02590-6.

[40] S. Arrhenius, Über die Dissociationswärme und den Einfluss der Temperatur auf den Dissociationsgrad der Elektrolyte, Zeitschrift Für Phys. Chemie. 4U (2017) 96–116.

[41] H. Dong, A. Wang, G.M. Koenig, Role of coprecipitation and calcination of precursors on phase homogeneity and electrochemical properties of battery active materials, Powder Technol. 335 (2018) 137–146. doi:10.1016/j.powtec.2018.05.020.

[42] J. Rodríguez-Carvajal, Recent advances in magnetic structure determination by neutron powder diffraction, Phys. B Condens. Matter. 192 (1993) 55–69. doi:10.1016/0921-4526(93)90108-I.

[43] D. Oboroceanu, N. Quill, C. Lenihan, D.N. Eidhin, S.P. Albu, R.P. Lynch, D.N. Buckley, Communication—Observation of Arrhenius Behavior of Catholyte Stability in Vanadium Flow Batteries, J. Electrochem. Soc. 163 (2016) A2919–A2921. doi:10.1149/2.0361614jes.

[44] S.K. Myasnikov, A.P. Chipryakova, N.N. Kulov, Kinetics, energy characteristics, and intensification of crystallization processes in chemical precipitation of hardness ions, Theor. Found. Chem. Eng. 47 (2013) 505–523. doi:10.1134/S0040579513050229.

[45] N. Doki, H. Seki, K. Takano, H. Asatani, M. Yokota, N. Kubota, Process control of seeded batch cooling crystallization of the metastable α-form glycine using an in-situ ATR-FTIR spectrometer and an in-situ FBRM particle counter, Cryst. Growth Des. 4 (2004) 949–953. doi:10.1021/cg030070s.

[46] R. Doremus, Precipitation kinetics of ionic salts from solution, J. Phys. Chem. 2158 (1968). doi:10.1021/j150567a011.

[47] M.Z. Mubarok, J. Lieberto, Precipitation of Nickel Hydroxide from Simulated and Atmospheric-leach Solution of Nickel Laterite Ore, Procedia Earth Planet. Sci. 6 (2013) 457–464. doi:10.1002/eej.4390960608.

[48] K. Du, L.-H. Zhang, Y.-B. Cao, H. Guo, Z.-D. Peng, G.-R. Hu, Synthesis of LiFe0.4Mn0.6−x Ni x PO4/C by co-precipitation method and its electrochemical performances, J. Appl. Electrochem. 41 (2011) 1349. doi:10.1007/s10800-011-0356-2.

[49] L. Liang, K. Du, Z. Peng, Y. Cao, J. Duan, J. Jiang, G. Hu, Co–precipitation synthesis of Ni0.6Co0.2Mn0.2(OH)2 precursor and characterization of LiNi0.6Co0.2Mn0.2O2 cathode material for secondary lithium batteries, Electrochim. Acta. 130 (2014) 82–89. doi:10.1016/j.electacta.2014.02.100.

[50] M. Noh, J. Cho, Optimized Synthetic Conditions of LiNi0.5Co0.2Mn0.3O2 Cathode Materials for High Rate Lithium Batteries via Co-Precipitation Method, J. Electrochem. Soc. . 160 (2013) A105–A111. doi:10.1149/2.004302jes.

[51] M.C. López, J.L. Tirado, C. Pérez Vicente, Structural and comparative electrochemical study of M(II) oxalates, M = Mn, Fe, Co, Ni, Cu, Zn, J. Power Sources. 227 (2013) 65–71. doi:10.1016/j.jpowsour.2012.08.100.

[52] S. Guillemet-Fritsch, M. Aoun-Habbache, J. Sarrias, A. Rousset, N. Jongen, M. Donnet, P. Bowen, J. Lemaître, High-quality nickel manganese oxalate powders synthesized in a new segmented flow tubular reactor, Solid State Ionics. 171 (2004) 135–140. doi:10.1016/S0167-2738(03)00282-0.

[53] N. Mancilla, V. Caliva, M.C. D'Antonio, A.C. González-Baró, E.J. Baran, Vibrational spectroscopic investigation of the hydrates of manganese(II) oxalate, J. Raman Spectrosc. 40 (2009) 915–920. doi:10.1002/jrs.2200.

[54] M.G. Lioliou, C.A. Paraskeva, P.G. Koutsoukos, A.C. Payatakes, Heterogeneous nucleation and growth of calcium carbonate on calcite and quartz, J. Colloid Interface Sci. 308 (2007) 421–428. doi:10.1016/J.JCIS.2006.12.045.

[55] Y.-P. Lin, P.C. Singer, Effects of seed material and solution composition on calcite precipitation, Geochim. Cosmochim. Acta. 69 (2005) 4495–4504. doi:10.1016/J.GCA.2005.06.002.

[56] M. Augustin, D. Fenske, I. Bardenhagen, A. Westphal, M. Knipper, T. Plaggenborg, J. Kolny-Olesiak, J. Parisi, Manganese oxide phases and morphologies: A study on calcination temperature and atmospheric dependence, Beilstein J. Nanotechnol. 6 (2015) 47–59. doi:10.3762/bjnano.6.6.

6: Preliminary Work on Electrode Alignment , Dissertation Summary and Future Work

6.1. Overview

In this study we first used citric acid as the inhibitor in the coprecipitation reaction to synthesize plate shape precursors and final active materials LiMn1.5Ni0.5O4 (LMNO). The particles were successfully oriented normal to the current collector within the electrode slurry, being responsive to the applied magnetic field after coating with Fe3O4 superparamagnetic nanoparticles. The out-of-plane orientation of the particles is expected to form fast diffusion channels along the direction of electrode thickness, while the nano-scale porous network within the active particles forme during calcination allowed homogeneous and fast ion diffusion along the particle diameter. The superiority in ion diffusion and rate capability of the obtained electrodes would imply the possibility of this method in producing more high-energy electrode with other materials chemistries and compositions.

Some preliminary positive results have been collected and are reported in this chapter. This will guide us in the next step to get better electrochemical performances out of the obtained active materials. Future works in a wider aspect will be discussed as well, tying to the overall goal of synthesizing predictable precursors and final active materials for energy storage and other applications.

The element of this chapter will be added into a future publication:

Dong, H., Cai, C., Denecke, M. E., Remaly, G., Koenig, Jr., G. M. Low-tortuosity $LiMn_{1.5}Ni_{0.5}O_4$ electrode by particle alignment under low magnetic field. In Preparation.

6.2. Introduction

6.2.1. Electrode tortuosity

The transition of traditional vehicles with internal combustion engines burning fossil fuels into electrical vehicles (EV) using renewable energy sources demands the mass production of secondary batteries with high energy and power density, long cycle life and great safety. Lithium ion batteries have dominated the EV battery market due to the ubiquitous high energy density which allows for long mileage, and the structural stability under high-power or high-current pulse condition when propelling the car. Higher energy and power capacities, accessible under aggressive conditions such as fast charging and discharging, high or low temperatures, for the current Li-ion battery configuration through precise engineering design are still needed and are predicted to more than double the current capacities. A normal way for battery manufacturers to increase the energy density of batteries is calendaring the electrodes with high pressure, in order to densify the electrode. This step, while produce higher volumetric energy density, has been found to result in sacrificed cycle life and rate capability, due to the fact that calendaring generate a tortuous microstructure within the electrode that hinders the lithium ion diffusion under high current rates and also produces high polarizations [1]. Particle fracture under high strain, lithium metal plating, and gas generation from electrolyte oxidation are all possible results of local high polarization of electrodes.

Tortuosity of an electrode, τ, has been defined as the extent of which the electrode microstructure influences or decreases the effective lithium ion diffusion along the electrode layer thickness, as reflected in following equation:

$$D\_eff=\epsilon/\tau\ D\_0 \qquad [1]$$

where D_eff is the effective ionic diffusivity, ϵ is the electrode porosity, and D_0 is the bulk ionic diffusivity of the electrolyte. While in the ideal case the tortuosity should be equal to one, meaning that the microstructure created by certain packing pattern of particles doesn't affect normal ion diffusion as in the electrolyte, the practical tortuosity values measured for commercial electrode are in the range of 3-5, reflecting the fact that the complex and tortuous poring network hinders the lithium diffusion. Both simulation and experimental results have confirmed the importance of tortuosity of the electrodes on the accessible capacity from the batteries [2,3], showing that with the tortuosity as high as 3-5 capacity starts to fall dramatically when the C-rate increases above around 0.75C (charge or discharge within 1.3 hour), ion diffusion being the limiting step. Yet-Ming Chiang and his group published a few works on aligning the active particles normal to the current collector direction and have seen significant improvement in rate capabilities of the aligned electrode compared to the isotropic control electrodes [3–6]. The approaches they took to align the particles include co-extrusion [4], freeze-casting [3], and magnetic field alignment [5,6]. Compared to co-extrusion and freeze-casting methods, which requires the post-sintering process to control the channel size and density, magnetic field alignment method is more amenable to the current electrode manufacturer process, and it also allows the use of binder and carbon black to facilitate electrode integrity and electron transfer as in conventional electrodes. The alignment of particle under magnetic field requires a large aspect ratio of particles, such as rods and plates; it was also proved by simulation results that the out-of-plan orientation of high aspect ratio particles renders the electrode tortuosity much less than even the randomly oriented spherical particles [2]. Chiang group also came up with the method of aligning the pores into channel structure instead of aligning the particles, which seems applicable to any shapes of particles [5,6]. This method, however, uses oil-based emulsion as the pore forming agent which requires complete post-cleaning step, making the procedure complicated and sensitive to many potential synthesis conditions and parameters thus hard to scale up.

6.2.2. Particle Morphology Tuning by Chemical Inhibitors

Coprecipitation is a common method to synthesize precursors for single and multicomponent TM oxides materials both in labs and in manufacturing. Coprecipitation method has the advantages that it is relatively easy to perform in the lab, scalable, allows tunable and monodisperse particle morphologies [7–12], and provides homogeneous mixing of the multiple TM components throughout the secondary particles [13–15]. The particle morphologies can be adjusted by tuning the reaction conditions and the particle morphologies can be well retained after the calcination process, which makes particle morphology control viable [16,17]. Particles of different morphologies have been synthesized via coprecipitation method, including spheres, rods, plates, cubes, and hollow spheres [11,17–20]. Most particle morphology tuning requires the use of chemical agent. Ammonia is the most commonly used chelating agent in order to produce dense spherical particles [21,28–31] due to the formation of ammonia complexes with transition metal ions that slows down the precipitation rate [28], or the dissolution-recrystallization of the particles by ammonia in the solution [32]. Several other chemical species have been used as ‘chelating agent’ to synthesis battery active materials precursors, such as citric acid, ascorbic acid, glucose, etc. but most of these chemicals inhibit the growth of precipitate without a specific surface bonding and thus only reduce the particle size without a control of particle shape [17,25–27].

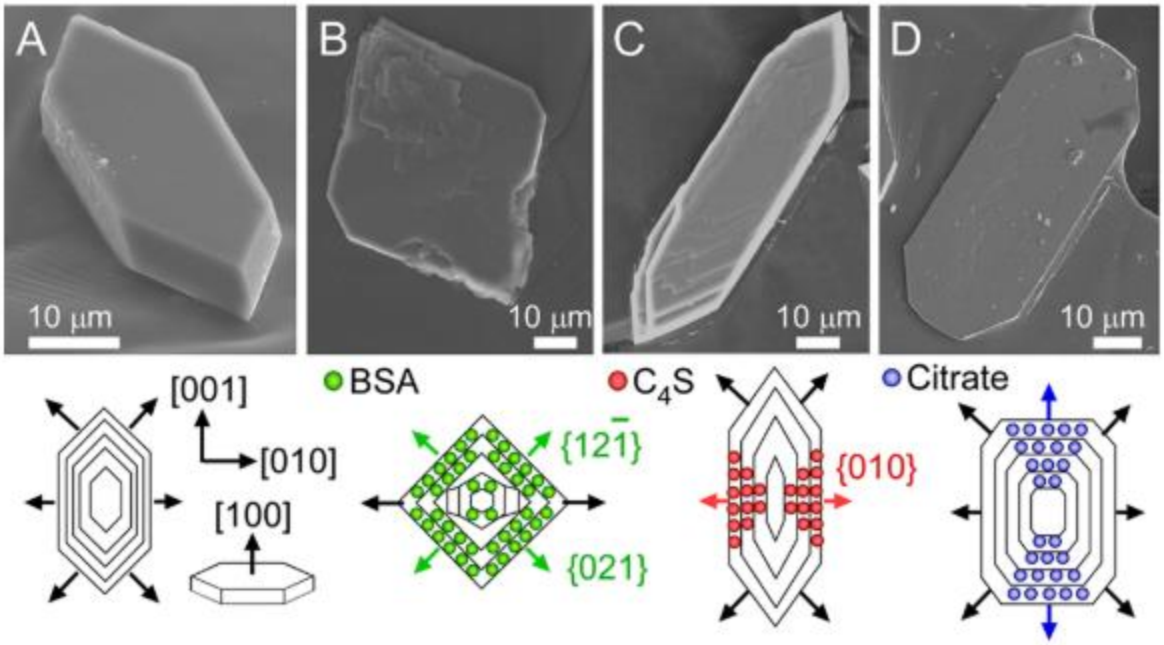

Figure 1. Different particle morphologies obtained after adding different chemical inhibitors in calcium oxalate crystallization and the proposed mechanism of specific binding of chemical inhibitor onto certain crystal facets. [7]

According to a report from Rimer group [7], the specific bonding of some organic or inorganic chemicals with calcium oxalate crystal facets resulted in the particle morphology change compared to the control experiment. Using citrate acid, one of the inhibitors in their study, as the inhibitor in the growth of calcium oxalate particles, they obtained quasi-rectangular flat particles as compared to the elongated hexagonal platelets of larger thickness obtained from the control synthesis experiment with no inhibitor added. Since the calcium oxalate monohydrate particles produced in their study has been characterized to have the monoclinic structure, and the precursor particles synthesized in our study exhibit a mixture of orthorhombic and monoclinic structure [8] we expected that the chemical inhibitors used in the calcium oxalate precipitation have similar behaviors and effects in tuning the particle morphologies in our system.

6.2.3. Composition Control for Coprecipitation with Inhibitor

The issue of composition deviation of the precipitated particles from the feed ratio can become more complicated considering that the added inhibitor has preferential binding with one TM than the other while making the precipitation reaction rates slower for both TM ions. Figure 2 shows our results of in-situ tracking of TM concentration in blend and pure reaction solutions, with or without citric acid added. It can be seen from the plot that the addition of citrate ion in the solution makes the difference in precipitation rate thus reaction extent more significant within a certain reaction timeframe, and thus feed ratio needs to be adjusted in order to get the stoichiometrically correct precipitate particles.

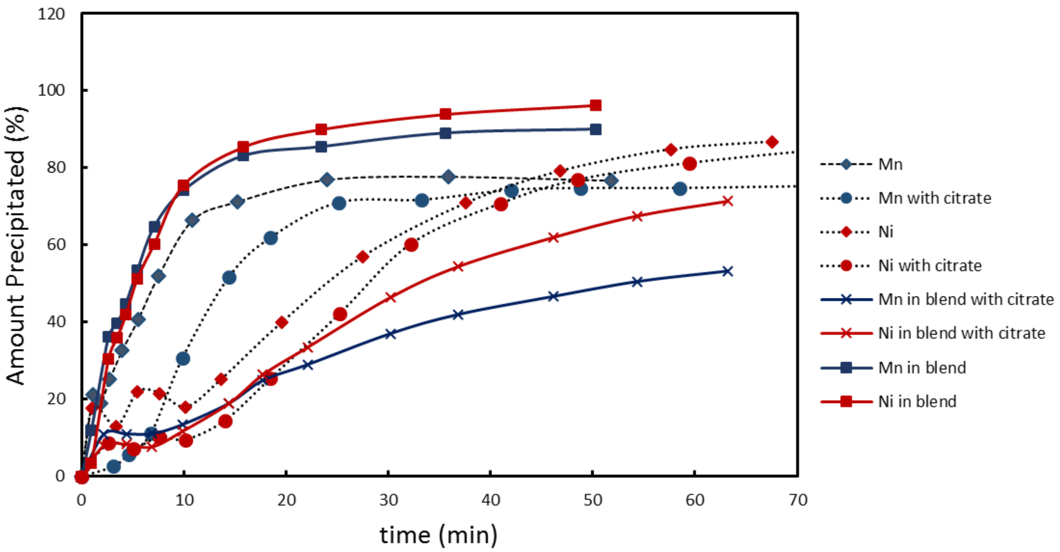

Figure 2. Amount of TM precipitated as a function of reaction time in the pure or blend solutions with or without citrate added.

6.3. Experimental

6.3.1. Oxalate Particles of Special Morphology

Laboratory grade $MnSO_4 \cdot H_2O$, $NiSO_4 \cdot 6H_2O$, $Na_2C_2O_4$, and $C_6H_8O_7$ (all from Fisher) were used for the coprecipitation synthesis. TM sulfate and oxalate reagents were dissolved separately in deionized (DI) water to prepare TM solution and oxalate solution, and both solutions were heated to 60 °C. The TM solution was then poured all at once into the oxalate solution to start the coprecipitation reaction. The total volumes of the mixed solutions were 0.8 L (within a 1 L beaker) for all syntheses, and the reagent masses were adjusted to desired solution concentration and TM feed ratio in order to get 3:1 Mn:Ni composition in the precipitate and final oxide materials with a certain concentration of inhibitor to tune particles morphology into platelet shape. To be specific equivalent TM salt masses of 50mM TM in the final solution with Mn:Ni ratio of 4.475:1 was prepared, and citric acid mass of equivalent 5.1mM citric in the final solution was added into the TM solution during preparation. The temperature was maintained during the reaction at 60 °C. The coprecipitation solution was stirred at 300 rpm with a magnetic stirrer. The particles were collected by vacuum filtration after 30 minutes, and then rinsed with ~2 L DI water before drying in the oven (Carbolite) at 80 °C overnight. The precursor particles were mixed with 5% excess LiOH with 1:2 Li:TM ratio using a mortar and pestle by hand for 5 minutes. This mixture was then fired in the furnace (Carbolite CWF 1300 box furnace) in an air atmosphere at 850°C for 6 hours to obtain the final active material (with the target composition generally being $LiMn_{1.5}Ni_{0.5}O_4$). The furnace temperature ramp rate was set at 1°C / minute, and during the firing process the temperature was programmed for holds at 200 °C and 350 °C each for 2 hours to complete the individual steps of the structural water loss and oxalate decomposition, respectively.

6.3.2. Electrode Alignment Setup

The process of electrode fabrication and battery cell assembly is almost the same as in the previous description for the control set of experiment. There are two differences: 1) the active materials were coated with Fe3O4 superparamagnetic nanoparticles by electrostatic force in aqueous suspension; 2) 20% extra NMP solution was added into the slurry in order to increase the electrode paste fluidity; 3) The gap of doctor blade for pasting the electrode slurry was chosen at 300 µm to also increase the fluidity of the paste to facilitate the particle alignment. For the aligned electrode, the same active materials and electrode ingredient were used except that the electrode paste was put onto the electrode alignment equipment as described below and get aligned under magnetic field during the drying process. The as-aligned electrode was put into an oven to dry at 80 °C overnight in air, followed by another 3 hours vacuum drying at 80 °C prior to punching into

14 mm diameter electrode disks and fabricated into half cell batteries with a Li metal chip as the anode.

The demonstration of particle alignment during electrode casting on a current collector is shown in Fig. 2, with the randomly coated electrode at the top and the magnetic aligned at the bottom [66]. The rotating magnetic field can be created by putting a magnet underneath the electrode paste while the magnet is rotating motivated by a motor. The detailed alignment method has also been reported, giving guide about the type and amount of magnetic Nano-particles needed to coat the active materials, making the particles responsive to external magnetic field [9].

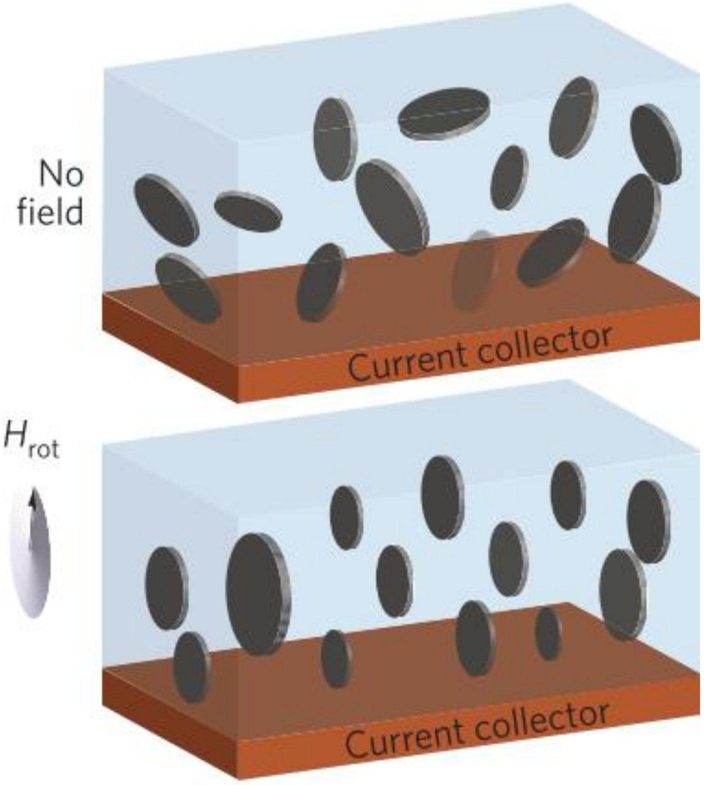

Figure 3. Demonstration of flakes alignment during electrode casting. Casting of the electrode paste without any applied magnetic field (top) and when a rotating magnetic field (Hrot) is applied during the drying step (bottom). [10]

Inspired by the electrode alignment experimental set up by the use of magnetic field from Billaud *et al.* [10] as shown in Figure 4a), we built up a similar setup as shown in Figure 4b) developed to provide support for the drying electrodes while providing a revolving magnetic field. Structurally, there were three main components, a base plate and two side plates. All three of these components were machined from 0.75 in 6061-T6 aluminum plate from Mcmaster-Carr. Machining was done with a Maximum waterjet and a YCM vertical machining center. The base plate provided mounting for the side plates and motor, while the side plates supported a piece of glass that the electrodes would dry on. One of the side plates also had mounting for the bearing, a 0.5 in pillow-block style bearing, Mcmaster-Carr product 5967K31. For fasteners, standard metric M8 bolts were used. The magnet was a 1.0 in cube neodymium magnet, with 14,400 internal gauss from amazon. This was held to a 0.5 in diameter stainless steel shaft with an aluminum coupler. The coupler was made by water jetting two pieces of 0.5 in of aluminum and welding them together with a Miller TIG welder. Two holes were then drilled and tapped for set screws. The motor was a Hangar 9 PowerPro HD nitro engine starter, which was powered by a generic 300W power supply. All components were modelled in Autodesk Fusion 360, and toolpaths for machined parts were generated in Fusion 360 as well.

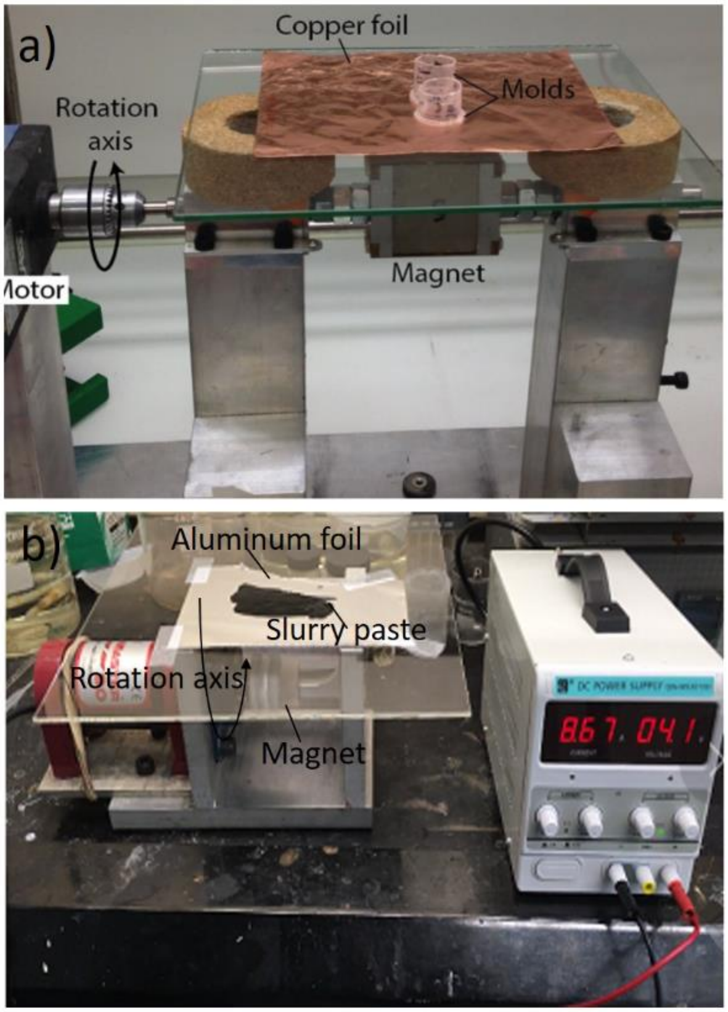

Figure 4. Electrode alignment experimental setup enabled by magnetic field spinning as applied in literature a) [10] and in our work b).

6.4. Preliminary Results and Discussion

ICP-OES results of the obtained particles showed a Mn:Ni ratio in the precipitate precursors and also the final TM oxide materials to be 2.98:1, very close to 3:1 and were considered to be stoichiometric spinel $LiMn_{1.5}Ni_{0.5}O_4$. The particle morphologies were characterized by SEM and shown in Figure 5. And it can be clearly seen that the particles are hexagonal platelets comprised of nano-scale primary particles. The coated Fe_3O_4 particles on the surface can also be seen after electrostatic coating (Figure 5 b).

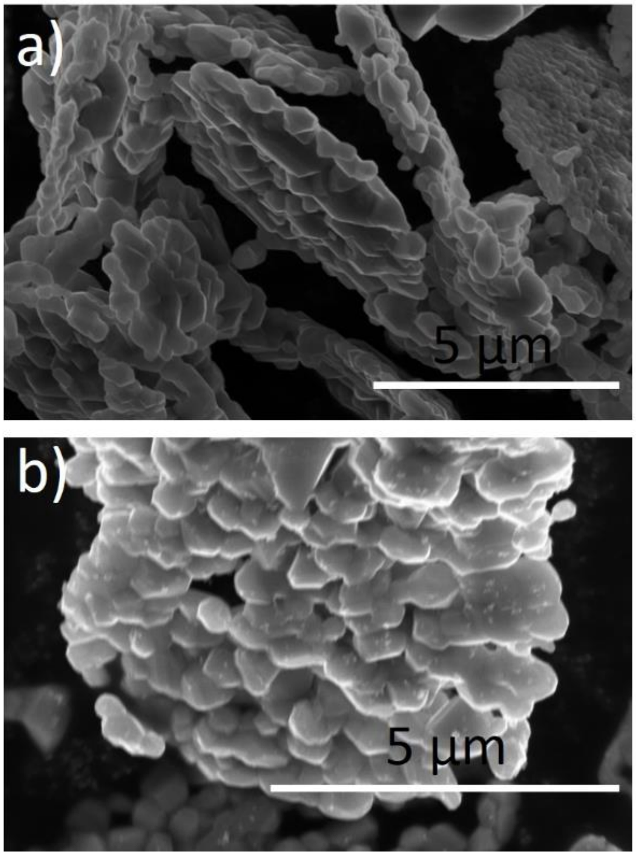

Figure 5. SEM images of platelet LMNO particles of stoichiometric composition synthesized from inhibitor added coprecipitation before a) and after b) superparamagnetic nanoparticles coating.

The difference in rate capability in the aligned electrode due to the reduced tortuosity was not clearly seen from the comparison between the aligned and control electrodes (Figure 6). The aligned electrode actually exhibited worse rate capability indicated by smaller specific capacities at higher current rates (>= C/5, which means the current for discharging the cell within 5 hours according to the theoretical LMNO capacity). It should also be noted that even the theoretical at low discharge rate such as C/20 the obtained specific capacities were both much lower than the theoretical value for LMNO (148 mAh/g).

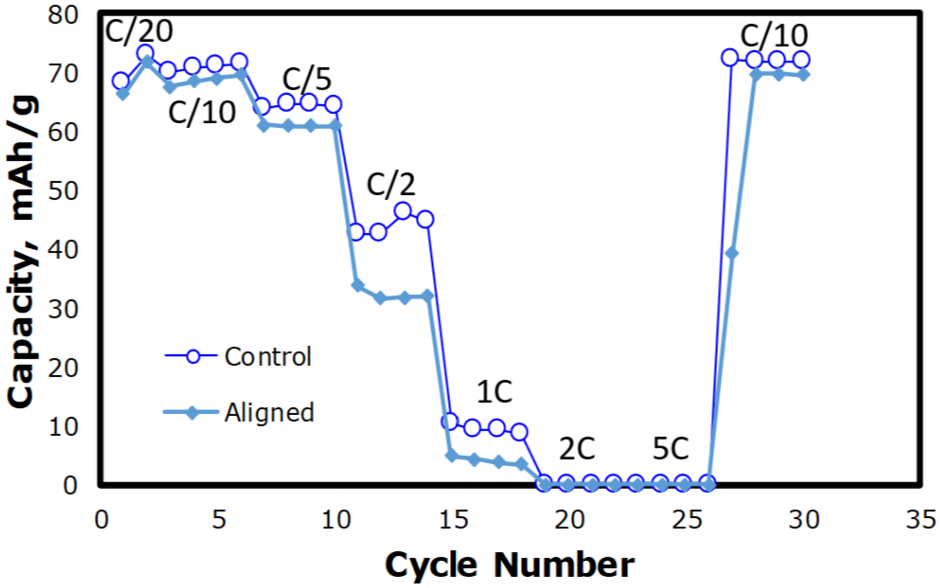

Figure 6. Specific capacities of half cell batteries from the aligned and control cathode electrodes. The cell were charged and discharged at C/20 for two cycles, and at C/10, C/5, C/2, 1C, 2C, 5C each for four cycles, and then at C/10 for four cycles at the end.

SEM images of the aligned electrode showed particle aligned at all different directions and no clear alignment pattern along the out-of-plan direction was observed (Figure 7), which was similar to the not-aligned control electrode. A big fracture in the electrode load was also observed from the figure. The poor rate capability of the aligned electrode may be attributed to the fractures formed during the drying process of the slurry left by the evaporation of the higher volume of NMP solution. The incomplete alignment of the platelet particles may also cause the higher void fraction within the electrode pack, making the Li transportation path more tortuous.

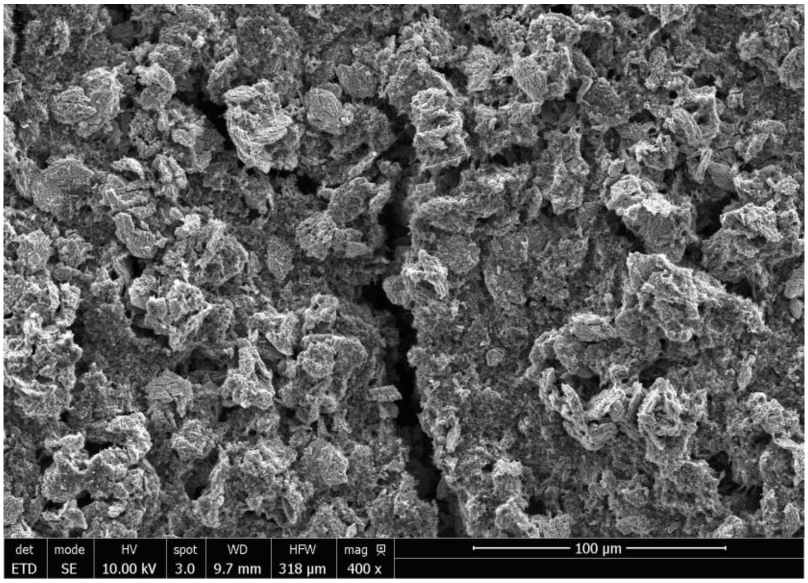

Figure 7. SEM images of the aligned electrode.

6.5. Conclusions

Even though we successfully synthesized the platelet particles by using citric acid as the chemical inhibitor and also make the final stoichiometry correct in the active materials by tuning the TM feed ratio during the coprecipitation reaction, we were not able to collect the expected results in terms of the progress in rate capability of the battery cells after electrode alignment treatment. SEM images showed fractures within the electrode in the out-of-plane orientation which might be one of the reasons why the electrodes showed lower capacities than the theoretical value in all current rates applied. The incomplete alignment may be the reason why the aligned electrode showed worse Li ion conductivity due to the higher void fraction compared to the not-aligned control electrode in which particles naturally aligned in-plane under gravimetric force.

These results indicated that the platelet particles may not be the ideal particle morphologies if the particle alignment is not efficient. This can also be supported by the observation that the octahedron shaped LMNO particles synthesized from coprecipitations without chemical inhibitor added showed significant superiority in rate capabilities. This reflected the necessities to explore the alignment effect as a function of particle morphology including particle size and shape. A few other experimental parameters that influence the alignment efficiency should also be systematically studied and optimized, including the solvent fraction of electrode slurry, the spinning rate of the magnet, the temperature during the alignment and drying.

We also need to develop a reliable technique to measure the tortuosity of electrodes, which will not only quantitatively measure the alignment extent of the particles but confirm that the advance in the rate capability is due to the decrease in electrode tortuosity.

6.6. Dissertation Summary and Future Work

This dissertation work looked into the solution chemistry of multicomponent coprecipitation reactions, with the blend coprecipitation of Mn and Ni as an example, to gain insights about the crystallization and particle process of the reaction and the interaction between precipitation of different ions and its influence on the particle composition, morphology, and phase purity. Reliable techniques were applied and developed to be able to in-situ track the solution concentration, and particle size distribution along the reaction; the method of detecting new phase formation in the precipitate particles was also found by experimentally measuring apparent activation energies of the reaction and observing local minimum. Particle tunability was achieved by chemical inhibitor addition, while more systematic study is needed to take advantage the particles of certain morphology and get better electrochemical performances from the battery cells.

Coprecipitation is a complicated process with many physical and chemical processes occurring simultaneously, and many factors potentially influencing the mechanisms of crystallization and particle growth. As more knowledge and insights are gained about the relationship between reaction conditions and product particle properties, there is chance that a computational model can be developed to guide the choice of reaction conditions in order to synthesize product particles of desired properties. Such model will need to take a wide range of reaction parameters for account, and to provide an accurate prediction of all the physical and chemical processes along the coprecipitation reaction. A recently published paper by Argonne National Lab reported their progress in predicting the precursor particles' properties from hydroxide coprecipitation. The computational outcomes were comparable to the experimental results but with significant mismatch due to the over-simplicity of their model [11]. Further advance in the development of such models, followed after the gain of deeper understanding of the coprecipitation reaction is expected to predict the results of higher resolution and to guide the control of reaction conditions and chemical selection.

Meanwhile the design space is expected to expand as the kinetics of the reaction become better understood. So far only limited particle morphologies have been synthesized via coprecipitation, especially compared to the particle products from hydrothermal synthesis.

Hydrothermal synthesis approach, however, always requires the use of high temperature for a long reaction time to obtain target particles. With the advantage of mild reaction condition, coprecipitation is expected to achieve wider variety of controllable particle properties as the fundamental knowledge of the reaction advances.

Advanced characterization methods are needed for the pursuit of fundamental knowledge of coprecipitation reaction. More advanced tools to in-situ measure the solution concentrations and particle morphologies, as well as characterization methods to investigate the cation and phase distribution within the precipitated particles, are critical for gaining reliable information of the reaction process and particles obtained, so that correlation between reaction process and particle product can be achieved. So far, less interest has been put into the study of precursor particles compared to the study of final active materials. However, more emphasis should be put into the study of coprecipitation reaction and the precursors, as a controllable synthesis process of the precursor particle determines not only the properties of the intermediate precursor particles but most importantly the properties and performances of the final materials in real applications.

6.7. Reference

[1] S.J. Harris, P. Lu, Effects of Inhomogeneities—Nanoscale to Mesoscale—on the Durability of Li-Ion Batteries, J. Phys. Chem. C. 117 (2013) 6481–6492. doi:10.1021/jp311431z.

[2] M. Ebner, D.W. Chung, R.E. García, V. Wood, Tortuosity anisotropy in lithium-ion battery electrodes, Adv. Energy Mater. 4 (2014) 1–6. doi:10.1002/aenm.201301278.

[3] B. Delattre, R. Amin, J. Sander, J. De Coninck, A.P. Tomsia, Y.-M. Chiang, Impact of Pore Tortuosity on Electrode Kinetics in Lithium Battery Electrodes: Study in Directionally

Freeze-Cast LiNi 0.8 Co 0.15 Al 0.05 O 2 (NCA), J. Electrochem. Soc. 165 (2018) A388–A395. doi:10.1149/2.1321802jes.

[4] C.J. Bae, C.K. Erdonmez, J.W. Halloran, Y.M. Chiang, Design of battery electrodes with dual-scale porosity to minimize tortuosity and maximize performance, Adv. Mater. 25 (2013) 1254–1258. doi:10.1002/adma.201204055.

[5] L. Li, R.M. Erb, J. Wang, J. Wang, Y.-M. Chiang, Fabrication of Low-Tortuosity Ultrahigh-Area-Capacity Battery Electrodes through Magnetic Alignment of Emulsion-Based Slurries, Adv. Energy Mater. 1802472 (2018) 1802472. doi:10.1002/aenm.201802472.

[6] J.S. Sander, R.M. Erb, L. Li, A. Gurijala, Y.M. Chiang, High-performance battery electrodes via magnetic templating, Nat. Energy. 1 (2016). doi:10.1038/nenergy.2016.99.

[7] S. Farmanesh, S. Ramamoorthy, J. Chung, J.R. Asplin, P. Karande, J.D. Rimer, Specificity of Growth Inhibitors and their Cooperative Effects in Calcium Oxalate Monohydrate Crystallization, J. Am. Chem. Soc. 136 (2014) 367–376. doi:10.1021/ja410623q.

[8] H. Dong, G.M. Koenig Jr, Compositional control of precipitate precursors for lithium-ion battery active materials: role of solution equilibrium and precipitation rate, J. Mater. Chem. A. 5 (2017) 13785–13798. doi:10.1039/C7TA03653A.

[9] R.M. Erb, R. Libanori, N. Rothfuchs, A.R. Studart, Composites Reinforced in Three Dimensions by Using Low Magnetic Fields, 202508 (2012) 199–205.

[10] J. Billaud, F. Bouville, T. Magrini, C. Villevieille, A.R. Studart, Magnetically aligned graphite electrodes for high-rate performance Li-ion batteries, Nat. Energy. 1 (2016) 1–13. doi:10.1038/nenergy.2016.97.

[11] P. Barai, Z. Feng, H. Kondo, V. Srinivasan, Multiscale Computational Model for Particle Size Evolution during Coprecipitation of Li-Ion Battery Cathode Precursors, J. Phys. Chem. B. (2019) acs.jpcb.8b12004. doi:10.1021/acs.jpcb.8b12004.

Appendix

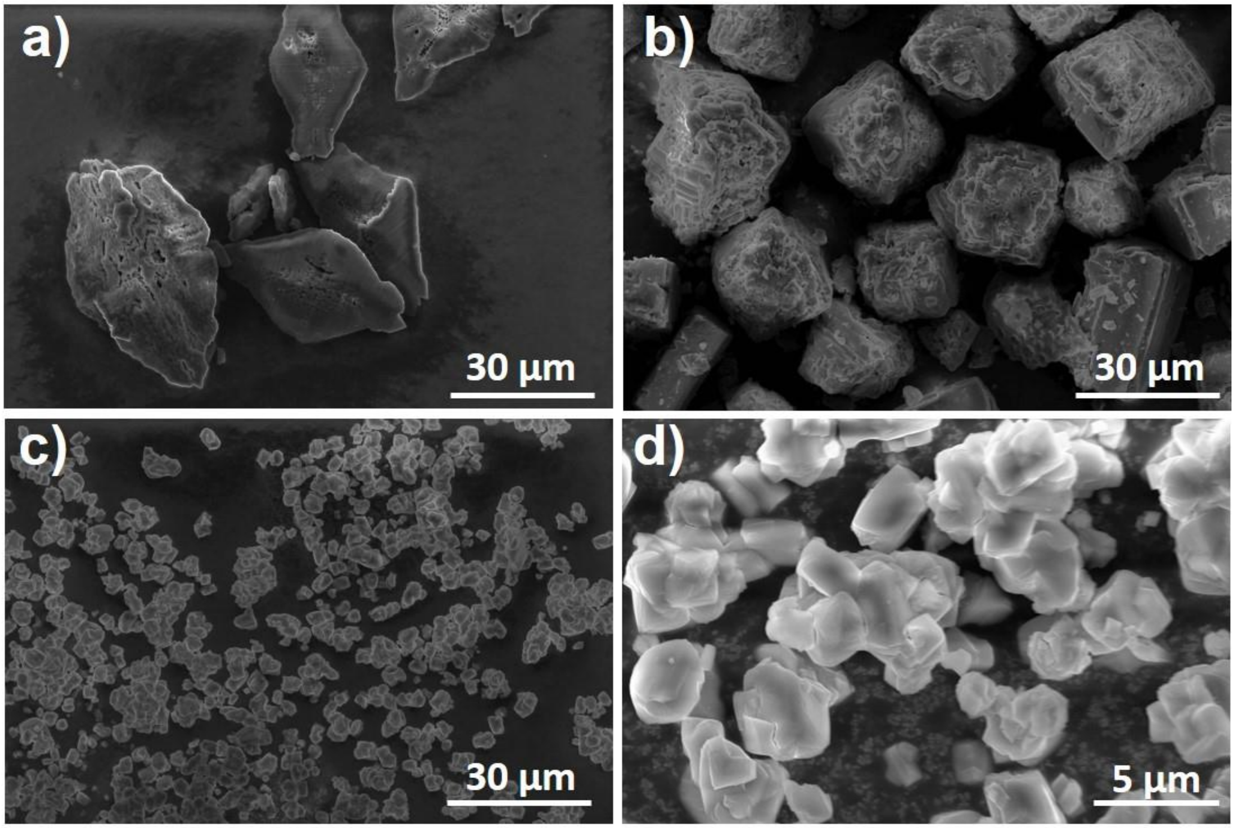

Figure S1. a) SEM image of $MnC_2O_4 \cdot 2H_2O$ collected after 30 minutes of precipitation of 20 mM Mn^{2+} feed. b) SEM image of $MnC_2O_4 \cdot 2H_2O$ used as seeds for the seeded precipitation experiments. The seeds were synthesized by collecting the precipitate after 5 minutes of precipitation of 100 mM Mn^{2+} feed. c) SEM image of $NiC_2O_4 \cdot 2H_2O$ particles collected after 30 minutes of precipitation of 20 mM Ni^{2+} feed. The SEM in d) is a higher magnification image of the same sample shown in c). In all precipitations for the particles shown in this figure, the $C_2O_4^{2-}$ feed concentration was the same as the transition metal feed concentration.

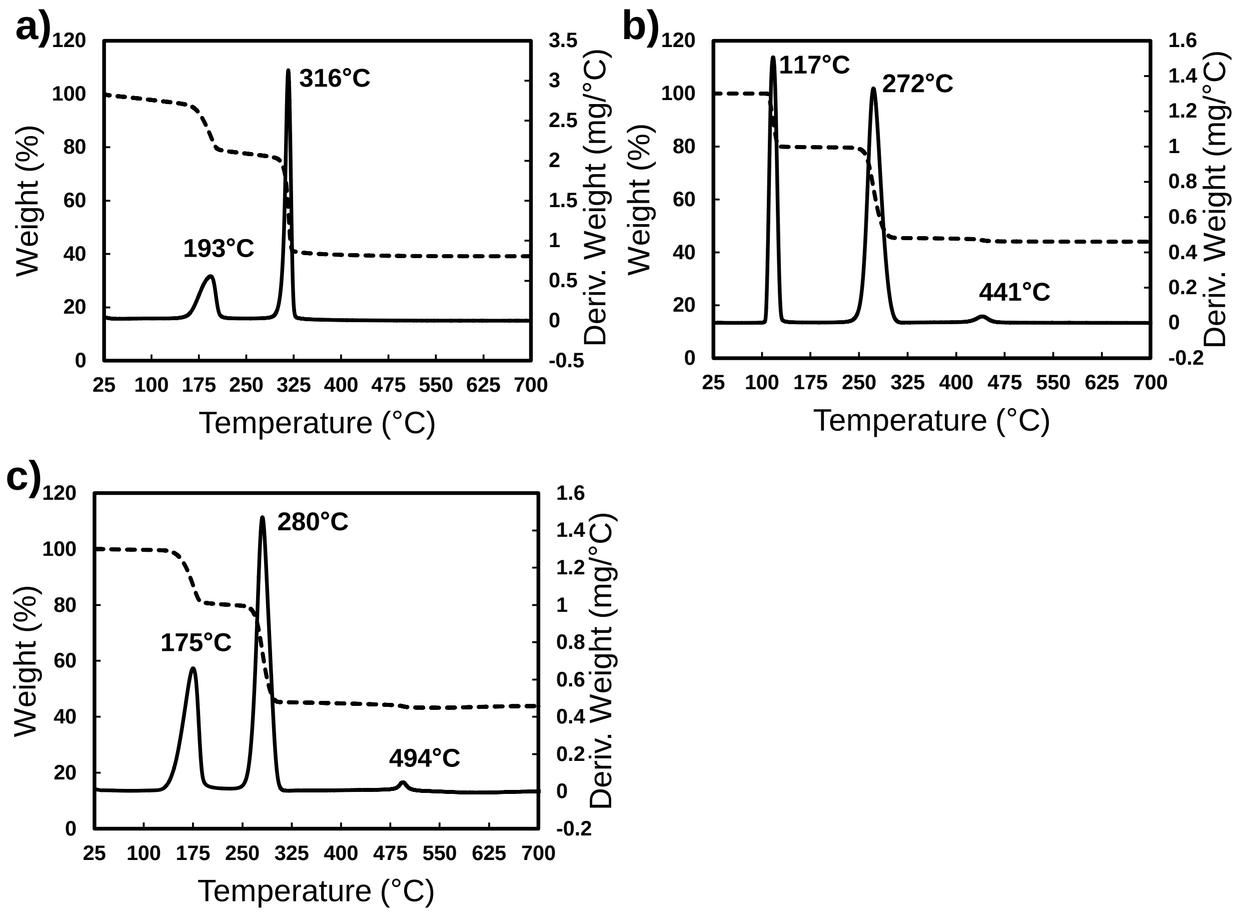

Figure S2. TGA profiles for a) $NiC_2O_4 \cdot 2H_2O$, b) $MnC_2O_4 \cdot 2H_2O$, and c) $Mn_{0.72}Ni_{0.28}C_2O_4 \cdot 2H_2O$. Dashed lines are fractional weight change as a function of temperature and solid lines are the derivative of the weight loss.

Discussion of TGA Profiles for Oxalate Precipitates

In the case of $NiC_2O_4{\cdot}2H_2O$, the dehydration was relatively gradual and peaked at 193 °C and the oxalate decomposition had a sharp peak at 316 °C (Figure S2a). The mass loss of 59.00 % was consistent with a theoretical expectation of 59.13 % for conversion to NiO. In the case of $MnC_2O_4{\cdot}2H_2O$, the dehydration peak was at 117 °C and the oxalate decomposition peak was at 272 °C (Figure S2b). The temperature for the dehydration and decomposition, as well as the further mass loss of 1% with a peak at 441 °C, were in good accordance with previous reports.[174] The final product of thermal treatment of manganese oxalate under high temperature in air is reported to be Mn_2O_3 [2-5], which was consistent with XRD patterns of our $MnC_2O_4{\cdot}2H_2O$ material heated above the minor mass loss temperature at 441 °C (data not shown). The minor mass loss has previously been attributed to the phase transition from Mn_5O_8 to Mn_2O_3, accompanied by oxygen loss and the desorption of water and carbon dioxide from the particle surface [1,2]. The total mass loss of 55.98 % was also in agreement with the theoretical value for a final product of Mn_2O_3 (55.90 %). The blend oxalate (composition $Mn_{0.72}Ni_{0.28}C_2O_4{\cdot}2H_2O$ from ICP and TGA analysis) had a dehydration peak at 175 °C and an oxalate decomposition peak at 280 °C (Figure S2c). Both peaks were between the values observed for the pure Mn and Ni oxalates. The blend oxalate had a gradual peak for dehydration, similar to that observed for the pure $NiC_2O_4{\cdot}2H_2O$. The high Mn content of the blend oxalate likely also contributes to the formation of similar Mn species that result in the small peak at higher temperatures also observed in $MnC_2O_4{\cdot}2H_2O$ samples (Figures 2b,c).

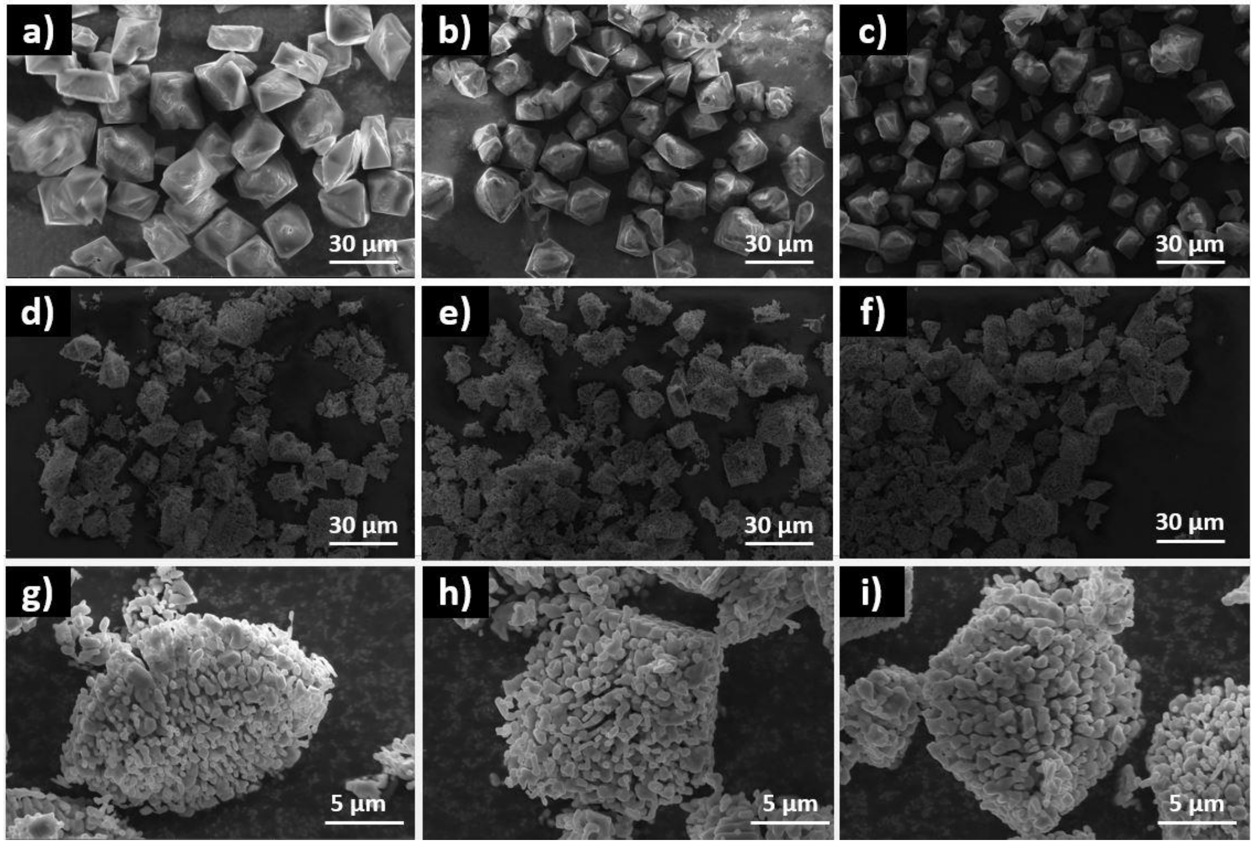

Figure S3. SEM images of a) Mn-rich, b) stoichiometric, and c) Ni-rich oxalate precursors; and the resulting d) Mn-rich, e) stoichiometric, and f) Ni-rich LMNO materials. g), h), and i) are the same powders as d), e), and f) at higher magnification.

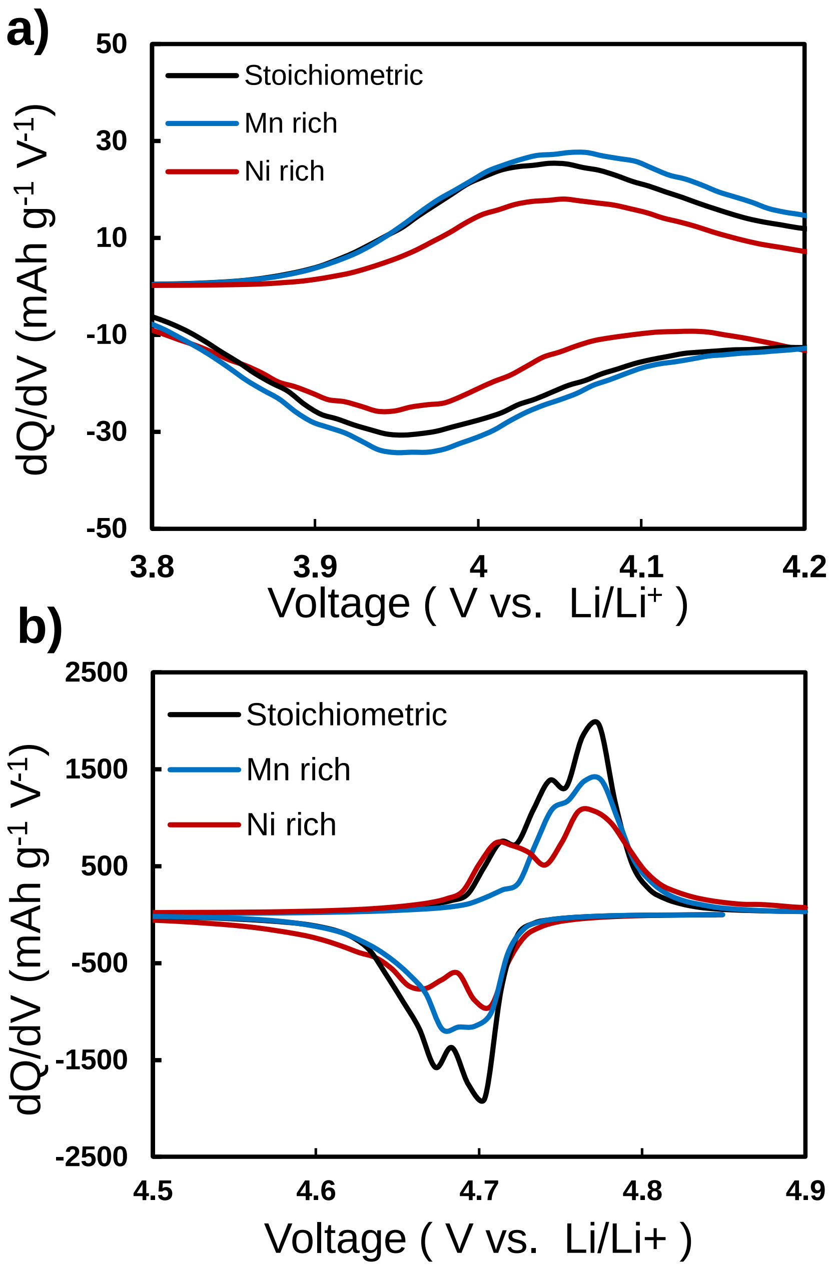

Figure S4. dQ/dV curves for the stoichiometric, Mn-rich, and Ni-rich materials cycled in Li/LMNO cells. The cells were cycled between 3.6 and 4.9 V (vs. Li/Li$^+$) and the regions shown are a) 3.8 to 4.2 V and b) 4.5 to 4.9 V. The cells were cycled at a rate of C/20 (6.3 mA/g LMNO).

Discussion of dQ/dV curves for LMNO cells

Figure S4 shows the dQ/dV for the second charge/discharge cycle at rate of C/20 for the stoichiometric, Mn-rich, and Ni-rich materials. The voltage range for Figure S4a was chosen to focus on the range associated with the Mn^{3+}/Mn^{4+} redox couple and the voltage range for Figure S4b was chosen to focus on the range associated with the $Ni^{2+}/Ni^{3+}/Ni^{4+}$ redox couple(s). In the low voltage range (Figure S4a), all samples had a broad Mn oxidation peak between 4.0-4.1 V that corresponded to the low voltage capacity region during charge/discharge. The dQ/dV peak areas of the Mn-rich and stoichiometric LMNO cells were close, and both were greater than that of the Ni-rich LMNO, indicating that the Mn^{3+} content in the Mn-rich and stoichiometric LMNO was greater and consistent with other results reported in this manuscript. For the Ni redox couple peaks observed above 4.6 V (Figure S4b), three different peak positions were exhibited during Ni oxidation on charging. Kim et al. previously reported that Fd-3m disordered LMNO had two separate peaks at 4.7 V and 4.76 V in dQ/dV charging curves, while the $P4_332$ ordered LMNO structure also had two peaks but they were closer in potential at 4.74 V and 4.76 V [6]. The lower voltage peak shifted from 4.7 V to 4.74 V at the transition from the disordered to ordered LMNO while the higher voltage peak maintained the same voltage. Duncan et al. reported similar results, where the separation between the Ni oxidation peaks for dQ/dV was 20 – 30 mV for the ordered LMNO and 60 – 65 mV for the disordered LMNO [7]. Thus from the Ni oxidation peak positions of the three samples in Figure S4b, the results were consistent with the Ni-rich LMNO sample dominated by the Fd-3m disordered phase and the Mn-rich and stoichiometric LMNO samples exhibiting a blend of both the ordered and disordered spinel phases in the samples (thus both lower voltage Ni oxidation peaks were observed for three peaks in total). The results in Figure S4 were also consistent with a previous report from Zhong et al. that studied a series of different Mn:Ni compositions; they observed a larger separation of around 60 mV for the Mn:Ni 3:1 sample that contained $Li_xNi_{1-x}O$ rock salt impurity phase, and smaller separation for the Mn-rich LMNO [8]. We also observed XRD features consistent with the rock salt impurity phase for our Ni-rich material, and thus having two observable Ni oxidation peaks for this sample with greater separation was consistent with the rock salt impurity phase inducing electrochemical features consistent with only the disordered phase in the spinel structure. We also note that high Mn^{3+} content in the structure has also been reported to result in transition from ordered to disordered spinel phase according to Duncan et al.'s report.

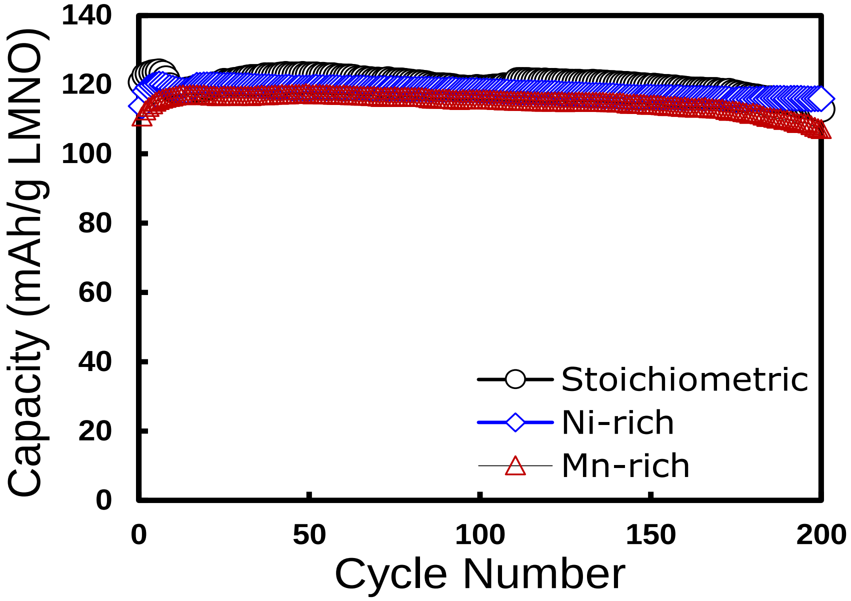

Figure S5. Cycle life test of stoichiometric (black circles), Mn-rich (red triangles), and Ni-rich (blue diamonds) LMNO. Cells were charged and discharged at C/10 rate (14.67 mA/g LMNO).

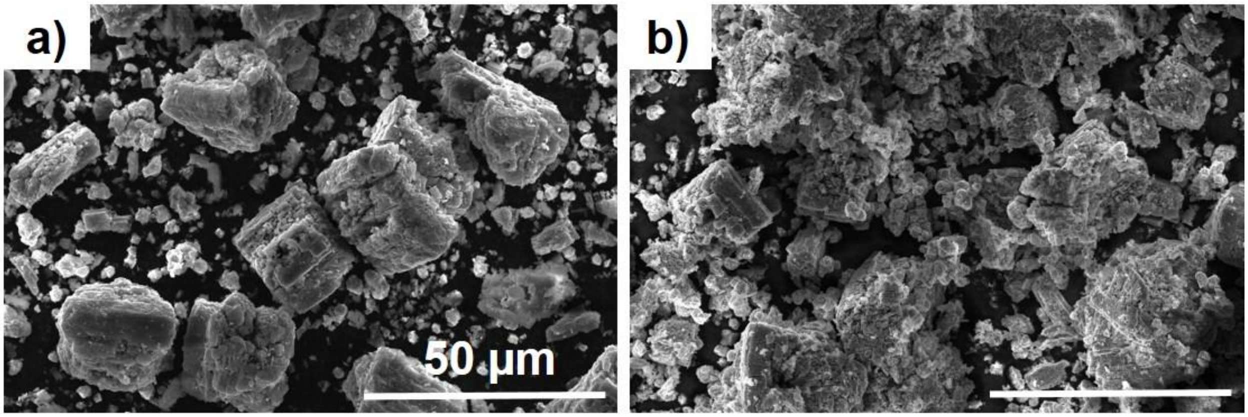

Figure S6. a) Scanning electron micrographs of physically mixed samples (mix of $MnC_2O_4\cdot 2H_2O$ and $NiC_2O_4\cdot 2H_2O$ powders) fired at a) 500°C and b) 700°C for 6 hours. Both scale bars 50 μm.

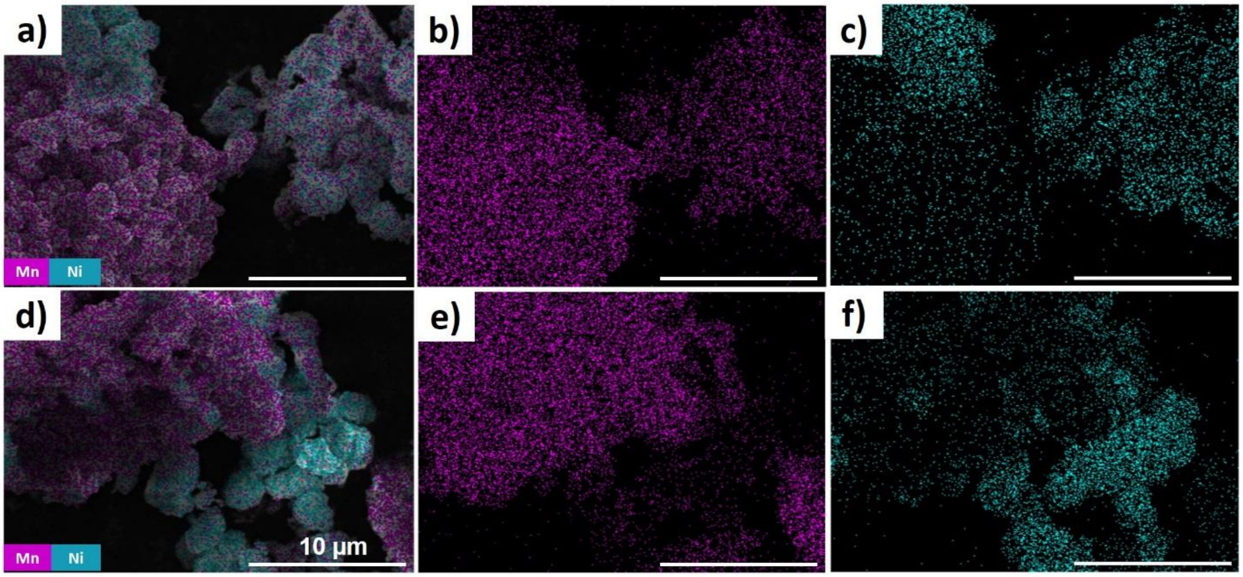

Figure S7. a) Energy dispersive spectroscopy (EDS) elemental compositional maps for Mn and Ni of physically mixed sample fired at 850°C for 6 hours (P-850-6 particles). b) Mn and c) Ni individual EDS maps of the same region as a). d) EDS elemental compositional map of physically mixed sample fired at 700°C for 48 hours (P-500-6 particles) with Mn and Ni. e) Mn and f) Ni individual EDS maps of the same region as d). For all images, magenta corresponds to Mn and blue corresponds to Ni. All scale bars correspond to 10 μm.

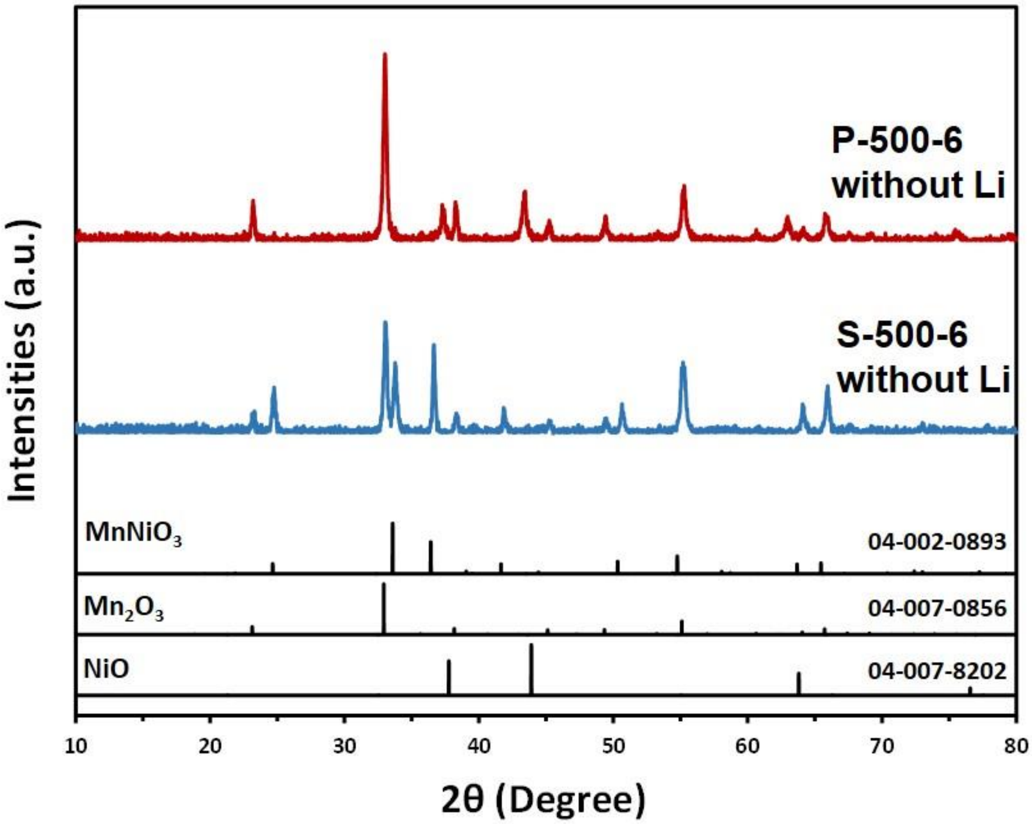

Figure S8. Sample powder XRD patterns and the relevant reference patterns from the literature. Sample patterns correspond to physically mixed sample fired at 500 °C for 6 hours with no lithium salt added (P-500-6 without Li, red) and solution mixed sample fired at 500°C for 6 hours with no lithium salt added (S-500-6 without Li, blue). The peak positions of the reference pattern of the potential transition metal oxide species of $MnNiO_3$, Mn_2O_3, and NiO are shown with their corresponding PDF card numbers.

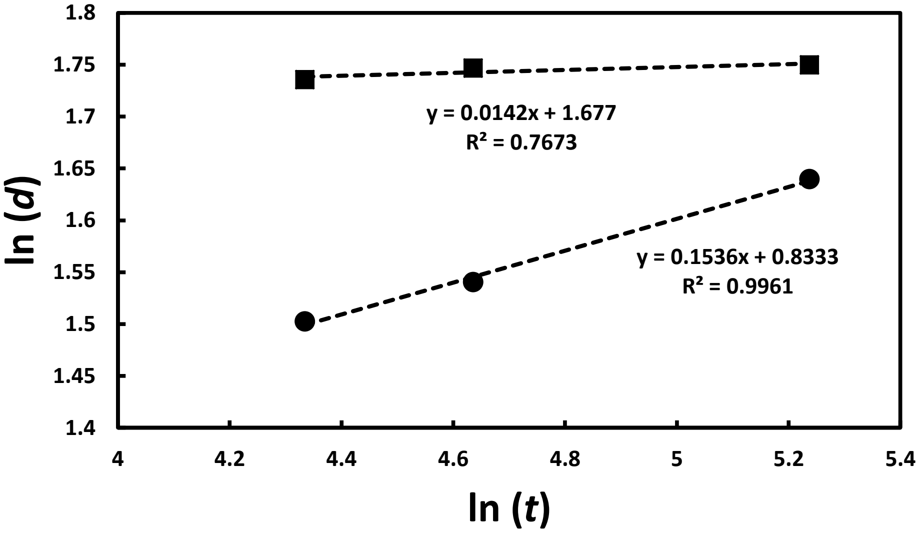

Figure S9. ln *d* vs. ln *t* for physically mixed samples (cubes) and solution mixed samples (circles) held at 700°C. *d* is the average grain size calculated by the Scherrer equation in units of nanometers, and *t* is the calculation time in units of seconds. Linear least squares best fits for the two data sets are shown as dashed lines, with their corresponding equations and R^2 values.

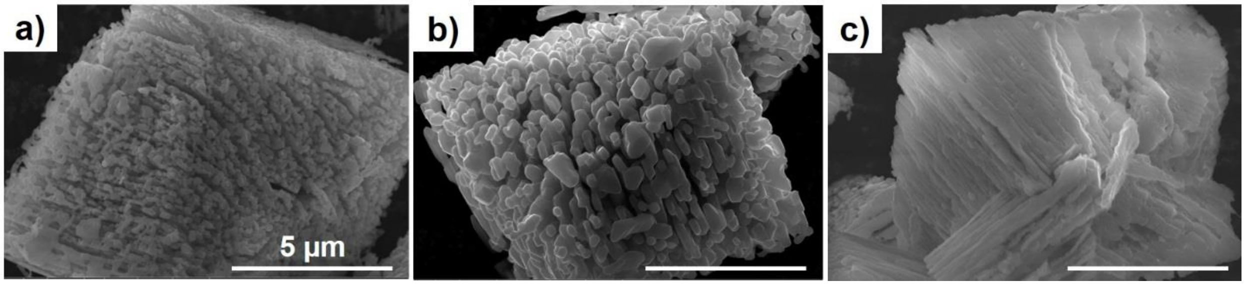

Figure S10. Scanning electron micrographs of solution mixed samples fired at a) 700°C for 6 hours (S-700-6), b) 850°C for 6 hours (S-850-6), and c) 700°C for 48 hours (S-700-48). All scale bars correspond to 5 µm.

Calculation of the rate constant in the diffusion-controlled solid reaction equation

As discussed in the manuscript, the relationship between reaction fraction and time can be described by the Equation 1:

$$\left(1-(1-\alpha)^{1/3}\right)^{2}=k'{t}, \qquad (1)$$

where $k' = {k_1}/{r_0}^2 = \frac{2DV_mC_0}{{r_0}^2}$ [9, 10]. D is the diffusion coefficient of the penetrating or diffusing species B, V_m is the volume of product formed from per mole of B, and C_0 is the concentration of B species outside the spherical particle. Assuming that the unreacted inner sphere has no penetrating species, C_0 is therefore the driving force for the diffusion process due to concentration difference.

Taking the diffusion of lithium ions from LiOH into the Mn and Ni oxide particles to form the final product $LiMn_{1.5}Ni_{0.5}O_4$ (LMNO) as an example, the initial concentration of the diffusing species (Li^+) outside the particle is calculated as below:

$$C_0 = d_{LiOH}\times\frac{n}{M_{LiOH}}=\left[1.46\ \frac{g}{cm^3}\right]\times\frac{[1\ mol]}{\left[23.95\frac{g}{mol}\right]}=0.0610\,\frac{mol}{cm^3}=6.10*10^4\,\frac{mol}{m^3}.$$

d_{LiOH} is the density of molten LiOH, *n* is the number of moles of lithium ions per mole of LiOH, and *M* is the molecular weight of LiOH.

And the volume of the product LMNO is calculated using the following equation:

$$V_m=\frac{\frac{1}{n}\times M_{LMNO}}{d_{LMNO}}=\frac{\frac{1}{1}\times 182.69\frac{g}{mol}}{4.44\frac{g}{cm^3}}=41.15\,\frac{cm^3}{mol}=4.11*10^{-5}\,\frac{m^3}{mol},$$

where n is the number of moles of lithium ions in one mole of LMNO, d and M are the density and molecular weight of LMNO respectively.

Substituting these two values as well as the diffusion coefficient D under the designated temperature calculated using Arrhenius equation and the initial particle size r_0, the rate constant k' can be obtained.

Calculation of the LMNO amount in physically mixed samples from the reaction fraction

As stated in the manuscript, for the physically mixed samples the conditions were simplified such that the manganese oxide was treated as a fixed component which was fully lithiated before the diffusion process initiated, and that nickel ions were treated as the penetrating species from NiO into $LiMn_2O_4$ (LMO) to form the final product LMNO.

Sample P-700-6 is shown here as an example to show the calculation process. The calculated reaction fraction after applying Equation S1 was 0.013 for sample P-700-6, which means that 0.013 moles of each one mole of initial LMO had reacted with NiO to form LMNO. For one mole of LMO, $\frac{2}{3}$ mole of NiO is needed to form LMNO, therefore if 0.013 of one mole of LMO is being converted in the reaction the mass of each unreacted reagent and the formed product at end of the reaction per mole of LMO will be as below:

$$m_{LMO} = M_{LMO} \times (1-\alpha) = 180.82\frac{g}{mol} \times (1-0.013) = 178.47\ {}^{g}/_{mol}$$

$$m_{NiO} = \frac{2}{3} \times M_{NiO} \times (1-\alpha) = \frac{2}{3} \times 74.69\frac{g}{mol} \times (1-0.013) = 49.15\,{}^{g}/_{mol}$$

$$m_{LMNO} = m_{LMNO} \times \alpha = 182.69\frac{g}{mol} * 0.013 = 2.37\,{}^{g}/_{mol}$$

Thus the LMNO mass fraction at end of the calcination process for this example sample is:

$$\frac{m_{LMNO}}{m_{LMO}+m_{NiO}+m_{LMNO}} = \frac{2.37{}^{g}/_{mol}}{(178.47+49.15+2.37){}^{g}/_{mol}} = 0.0103\,{}^{g}/_{g}.$$

Table S1. The resulting Mn:Ni ratios precipitates formed from 3:1 Mn:Ni feed stoichiometry as a function of total initial concentration of transition metal in the feed. Values are tabulated for equilibrium calculations, ICP measurements, and the deviation between calculations and measurements.

Feed Concentration (mol/L)	**Equilibrium Calculation**	**Measured using ICP**	**Deviation from Equilibrium (%)**
0.10	2.88	2.97	3.13
0.05	2.76	2.86	3.62
0.02	2.38	2.71	13.9
0.01	1.72	2.33	35.5

Note: The stoichiometries measured of the precursors collected after 30 minutes were slightly different from those based on *in-situ* TM concentration measurements. This likely resulted from the processing time and washing and filtering stages completed on the final full volume of precursor solution.

Table S2. The Mn:Ni ratio in the initial feed, calculated for the resulting precipitate at equilibrium, and measured in the resulting precipitate using ICP for the Ni-rich, stoichiometric, and Mn-rich materials.

Feed Ratio	**Mn:Ni Ratio in Precipitate**		**Deviation from Equilibrium (%)**	**Chemical Formula of LNMOs Measured by ICP**
	Equilibrium Calculation	**Measured using ICP**		
3.00	2.38	2.71	13.9	$Li_{0.94}Mn_{1.46}Ni_{0.54}O_4$
3.52	2.85	3.02	5.85	$Li_{0.97}Mn_{1.50}Ni_{0.50}O_4$
3.82	3.11	3.33	7.18	$Li_{0.96}Mn_{1.54}Ni_{0.46}O_4$

Note: The resulting stoichiometry of the active material after calcination is in the final column. Li, Mn, and Ni for the final material were determined via ICP ratios, while the O was assumed to be 4.

Appendix References

[1] J. Topfer, J. Jung, Thermal decomposition of mixed crystals NixMn3-x(C2O4)3.6H2O, Thermochim. Acta. 202 (1992) 281–289.

[2] S. Thota, B. Prasad, J. Kumar, Formation and magnetic behaviour of manganese oxide nanoparticles, Mater. Sci. Eng. B. 167 (2010) 153–160. doi:10.1016/j.mseb.2010.01.049.

[3] B. Donkova, D. Mehandjiev, Mechanism of decomposition of manganese(II) oxalate dihydrate and manganese(II) oxalate trihydrate, Thermochim. Acta. 421 (2004) 141–149. doi:10.1016/j.tca.2004.04.001.

[4] M.E. Brown, A.K. Galwey, Thermal Decomposition of Manganese(II) Oxalate in Vacuum and in Oxygen, J. Chem. Soc. Faraday Trans. 1 Phys. Chem. Condens. Phases. 70 (1974) 1316–1324.

[5] X. Gao, D. Dollimore, The thermal decomposition of oxalates, Thermochim. Acta. 215 (1993) 47–63. doi:10.1016/0040-6031(93)80081-K.

[6] J.-H. Kim, S.-T. Myung, C.S. Yoon, S.G. Kang, Y.-K. Sun, Comparative Study of LiNi0.5Mn1.5O4-δ and LiNi0.5Mn1.5O4 Cathodes Having Two Crystallographic Structures: Fd $\bar{3}$m and P 4332, Chem. Mater. 16 (2004) 906–914. doi:10.1021/cm035050s.

[7] H. Duncan, B. Hai, M. Leskes, C.P. Grey, G. Chen, Relationships between Mn 3+ Content, Structural Ordering, Phase Transformation, and Kinetic Properties in LiNi x Mn 2– x O 4 Cathode Materials, Chem. Mater. 26 (2014) 5374–5382. doi:10.1021/cm502607v.

[8] Q. Zhong, A. Bonakclarpour, M. Zhang, Y. Gao, J.R. Dahn, Synthesis and Electrochemistry of LiNixMn2-xO4, J Electrochem Soc. 144 (1997) 205–213. doi:10.1149/1.1837386.

[9] R.E. Carter, Kinetic Model for Solid-State Reactions, J. Chem. Phys. 34 (1961) 2010–2015. doi:10.1063/1.1731812.

[10] C.F. Dickinson, G.R. Heal, Solid–liquid diffusion controlled rate equations, Thermochim. Acta. 340–341 (1999) 89–103. doi:10.1016/S0040-6031(99)00256

Acknowledgement

I can write this part for the length of the whole thesis. But I will try to keep it short.

First, I want to thank my advisor Gary Koenig. Gary to me is more than advisor. As an international student coming from the other side of Pacific Ocean, I came here like a little baby, knowing little about the way people speak, interact, and live. And I learnt a lot of it from Gary (which makes me doubt if the way I speak English is more like a boy). To me he is a combination of teacher and parent, even though he seems too young to be seen as my parent, as he is too young to get a tenure already and many other achievements. But he is and he does! I have been feeling lucky to have such a great advisor and model. And one thing I feel particularly grateful about is that he always generously offers his praises to my work, even though it not always deserves them. In fact, those very positive feedbacks and encouragements from Gary might be one of the major reasons why I can make it to graduation.

And another of those reasons is Gilbert, my Fiancé and who soon will be my husband. I am so addictive to every dish he cooks for me, that I have long ago decided to marry him and let him be my labor for the whole life. Without him feeding me this well, I'd not have a healthy body and a happy mood every day to be as productive as I am now. Not only that, he'd pretty much do anything to get everything I want, even though I can be very demanding at times. I am so touched by his love and care for me, that I have determined to become a better and better woman, not only for myself but also for him to feel proud about.

And my parents. I cannot imagine how parents can do better than them to raise a child. They give me always the best they can along the way I grow up till now, and only hoping that I am safe, healthy, and happy. I feel bad that I have to depart so far away from them for these many years, and I also want to thank them for always respecting and supporting my decisions without

even thinking about their own needs. I wish we can get together as soon as possible, and get chance to spend some wonderful time with each other, maybe only sharing those trivial things in life, eating out, or taking a road trip.

But I never regret spending these five years for the pursuit of this degree. I value the things I learn from Gary, and the training I get through every piece of research, and all the support from family and friends. All of these make me feel confident and ready to start my new journey.